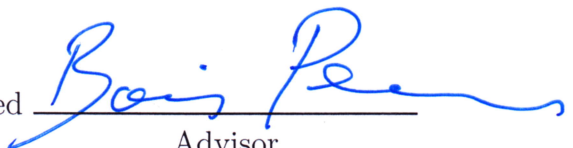


UNMANNED AIRCRAFT SYSTEM SENSE AND AVOID
INTEGRITY AND CONTINUITY

BY
MICHAEL B. JAMOOM

Submitted in partial fulfillment of the
requirements for the degree of
Doctor of Philosophy in Mechanical and Aerospace Engineering
in the Graduate College of the
Illinois Institute of Technology

Approved 
Advisor

Chicago, Illinois
May 2016

© Copyright by
MICHAEL B. JAMOOM
May 2016

ACKNOWLEDGMENT

I am eternally grateful to my academic advisor and dissertation committee chair, Professor Boris Pervan, for his clear guidance, flexibility with my military schedule (including four deployments), and consistent support. I appreciate his vision for my research, matching my aviation experience with the growing field of UAS. I must also thank my advisor and committee member, Professor Mathieu Joerger, for his technical expertise, endless availability for assistance, and infectious enthusiasm for research. I also thank the rest of my committee: Professors Kevin Cassel, John Kallend, and Matthew Spenko.

I have much appreciation for the FAA Hughes Tech Center's Phil Maloney and the rest of his UAS Certification Obstacle Team for supporting this research. It has been an honor serving as a member of the Certification Obstacle Team.

I also thank Colonel Dana Nelson, Colonel Eric Jenkins, Lt Col Scott Clark and my other commanders at Andrews AFB for having my back during this pursuit. I also appreciate the members of the 756th Air Refueling Squadron for their support and encouragement.

I acknowledge all of the Navigation Lab members (Dr Samer Khanafseh, Cagatay Tanil, Stefan Stevanovic, Yawei Zhai, Adriano Canolla, Ryan Cassel, Roohollah Parvizi and Soowon Kim) for their support. I am especially grateful to Stefan Stevanovic for generously sharing all of his LaTeX templates.

I can never thank enough my mother, Randee Jamoom, who raised my brothers and I on her own after my father's untimely death. Any success my brothers and I share are a testament to her. I also thank my brothers Joe Jamoom and Dr Eric Jamoom, for always being there for me. I am grateful to my ex-wife, Sarah Sunday, for her encouragement through the difficult first two years of this endeavor.

I thank Dr Kate McCauley for her friendship and for suggesting a PhD pursuit at a time when I was searching for direction. I also thank Hugh Miranzadeh, James Marsh, and Carrie Lannon, whose friendship truly made Chicago my home. I must also express gratitude to Jeff Few, Maggi McConnell, Dr Jake Bice, Vicki Raftree, Josh Kurland, Gil Riboni, Alex Riboni, Dr Tara Harris, and Jaime Espinoza for their enduring friendship over the years.

TABLE OF CONTENTS

	Page
ACKNOWLEDGEMENT	iii
LIST OF TABLES	viii
LIST OF FIGURES	x
ABSTRACT	xi
CHAPTER	
1. INTRODUCTION	1
1.1. The Need for Sense and Avoid	1
1.2. Self-Separation and Collision Avoidance	2
1.3. Evolution of the Well Clear Threshold	4
1.4. Problem Statement	5
1.5. Prior Work	6
1.6. Integrity Risk	8
1.7. Continuity Risk	9
1.8. Multiple Intruders and Data Association	10
1.9. Dissertation Contributions	11
1.10. Dissertation Outline	13
2. HAZARD STATE ESTIMATION	14
2.1. Intruder Trajectory Estimation	14
2.2. DAA Well Clear and Alerting Threshold	16
2.3. Modified Horizontal Time to CPA	19
2.4. Horizontal Closest Point of Approach	20
2.5. Predicted Vertical Separation	21
2.6. Hazard State Estimate and Estimate Error Variance	21
2.7. Hazard State Estimate Summary	22
3. INTEGRITY RISK	24
3.1. Integrity Risk Based Solely on Tau	24
3.2. Integrity Risk for All Hazard States	26
3.3. Integrity Risk Evaluation Summary	32
4. CONTINUITY RISK	34
4.1. Continuity Based Solely on Modified Tau	34
4.2. Continuity Risk for All Hazard States	35

4.3. Continuity Risk Evaluation Summary	39
5. OPERATIONAL LIMITS AND SENSOR REQUIREMENTS	41
5.1. Operational Limits	41
5.2. Relating Operational Limits to Sensor Requirements	44
5.3. Applying Self-Separation Tests	45
5.4. Summary of Operational Limits and Sensor Requirements	47
6. ANALYSIS OF 2D AND 3D ENCOUNTERS	48
6.1. Nominal Composite Sensor	48
6.2. Two Dimensional Analysis	49
6.3. Three Dimensional Analysis	60
6.4. Summary of 2D and 3D Sensitivity Analyses	66
7. INTRUDER LINEAR ACCELERATIONS	68
7.1. Constant Acceleration Kalman Filter	68
7.2. Hazard States for Linear Accelerations	70
7.3. Intruder Linear Acceleration Sensitivity Analysis	71
7.4. Summary of Intruder Linear Accelerations	75
8. MULTIPLE INTRUDERS	77
8.1. Multiple Intruder Integrity Risk	77
8.2. Continuity Risk	89
8.3. Analysis	89
8.4. Summary of Multiple Intruders	96
9. CONCLUSION	97
9.1. SAA Integrity and Continuity	97
9.2. Summary of Achievements	97
9.3. Future Work	99
9.4. Closing	100
APPENDIX	103
A. INTRUDER TRAJECTORY STATE ESTIMATION	103
A.1. Intruder Spherical Measurements	104
A.2. Measurement Model	104
A.3. Constant Velocity Batch Model	106
A.4. Kalman Filter Estimation Model	108
B. ALTERNATE HAZARD STATES	112
B.1. Simplified Tau	113
B.2. Time to Well Clear Threshold Entry	113

B.3. Vertical Position at Well Clear Threshold Entry and Exit	114
C. THE DISTANCE MODIFICATION	118
D. DERIVATION OF GEOMETRIC HORIZONTAL CPA	120
E. 2D ANALYSIS SENSOR ADJUSTMENTS	122
E.1. Sensor Sample Rate Uncertainty Adjustment	123
E.2. Sensor Detection Range Adjustment	124
F. CARTESIAN TO SPHERICAL PARTIAL DERIVATIVES	125
G. HAZARD STATE PARTIAL DERIVATIVES	128
G.1. Modified Tau	129
G.2. True Tau	130
G.3. Horizontal CPA	131
G.4. Predicted Vertical Separation	134
BIBLIOGRAPHY	135

LIST OF TABLES

Table		Page
2.1	DAA MOPS Alert Summary [72]	18
6.1	SAA Sensor Characteristics [12]	49
6.2	Nominal Sensor for Analyses	50
6.3	Results of a ρ -Adjusted Sensor	54
6.4	Results of a θ -Adjusted Sensor	56
6.5	Results of a $\dot{\rho}$ -Adjusted Sensor	57
6.6	Summary of Sensor Adjustments	58
6.7	Results of a ϕ -Adjusted Sensor	66
E.1	Results of a Δt -Adjusted Sensor	123
E.2	Results of a ρ_0 -Adjusted Sensor	124

LIST OF FIGURES

Figure	Page
1.1 Well Clear Threshold and NMAC (Not to Scale)	3
2.1 Horizontal and Vertical Position of the Intruder Aircraft	15
2.2 Overhead View of Closest Point of Approach	17
3.1 Integrity Risk and Adjusted Threshold	25
3.2 Worst Case HMI Scenario for r_{CPA}	28
3.3 2D Integrity Risk Correlation	30
4.1 Continuity Risk and the Continuity Buffer	35
4.2 Worst Case FA Scenario for r_{CPA}	36
4.3 2D Continuity Risk Correlation	38
5.1 Horizontal Operational Limits	43
5.2 τ_{mod} Operational Limits and Sensor Requirements	45
5.3 Applying All Operational Limits to Sensor Requirements	46
6.1 Two Dimensional Trajectories	51
6.2 Results of a Nominal Sensor	52
6.3 Nominal Normalized $\Delta\sigma$ Between Trajectories	53
6.4 Results of a ρ -Adjusted Sensor: $\sigma_\rho = 100$ feet	54
6.5 Results of a θ -Adjusted Sensor: $\sigma_\theta = 0.1^\circ$	55
6.6 Results of a $\dot{\rho}$ -Adjusted Sensor: $\sigma_{\dot{\rho}} = 100$ ft/s	56
6.7 Results of All Sensor Parameter Adjustments	58
6.8 Three Dimensional Trajectories	61
6.9 3D Results of a Nominal Sensor	62
6.10 Nominal Normalized $\Delta\sigma$ Between 3D Trajectories	64
6.11 3D Results of a ϕ -Adjusted Sensor: $\sigma_\phi = 0.01^\circ$	65
7.1 Results of a Nominal Sensor	73

7.2	Nominal Sensor Tau Comparison	74
7.3	Results of an Adjusted Sensor, $\sigma_\phi = 0.01^\circ$	75
8.1	Correctly Associated Measurements of Two Intruders	78
8.2	Measurement Incorrectly Associated for Two Intruders	79
8.3	First Intruder Encounter	90
8.4	Second Intruder Encounter	91
8.5	Fault Term During the First Encounter	92
8.6	First Encounter Probability of Incorrect Association	93
8.7	Second Encounter Bound on Probability of Incorrect Association	94
8.8	Fault Term During the Second Encounter	94
8.9	Adjusted Sensor $P(IA)$ Bound for Second Encounter	95
8.10	Second Encounter Fault Term Sensor Performance Comparison	95
9.1	DJI Spreading Wings S1000	101
9.2	Velodyne VLP-16 LIDAR PUCK™	101
B.1	Vertical Position at Horizontal Entry and Exit	114
B.2	Head-on Trajectories with 3D Closest Points of Approach	115
B.3	Possible Intruder Trajectories in $(\hat{z}_+; \hat{z}_-)$ Plane	116
E.1	Results of a Δt -Adjusted Sensor: $\Delta t = 0.35$ Hz	123
E.2	Results of a ρ_0 -Adjusted Sensor: $\rho_0 = 6.5$ NM	124

ABSTRACT

This thesis describes new methods to guarantee safety of sense and avoid (SAA) functions for Unmanned Aircraft Systems (UAS) by evaluating integrity and continuity risks. Previous SAA efforts focused on relative safety metrics, such as risk ratios, comparing the risk of using an SAA system versus not using it. The methods in this thesis evaluate integrity and continuity risks as absolute measures of safety, as is the established practice in commercial aircraft terminal area navigation applications. The main contribution of this thesis is a derivation of a new method, based on a standard intruder relative constant velocity assumption, that uses hazard state estimates and estimate error covariances to establish (1) the integrity risk of the SAA system not detecting imminent loss of “well clear,” which is the time and distance required to maintain safe separation from intruder aircraft, and (2) the probability of false alert, the continuity risk. Another contribution is applying these integrity and continuity risk evaluation methods to set quantifiable and certifiable safety requirements on sensors. A sensitivity analysis uses this methodology to evaluate the impact of sensor errors on integrity and continuity risks. The penultimate contribution is an integrity and continuity risk evaluation where the estimation model is refined to address realistic intruder relative linear accelerations, which goes beyond the current constant velocity standard. The final contribution is an integrity and continuity risk evaluation addressing multiple intruders. This evaluation is a new innovation-based method to determine the risk of mis-associating intruder measurements. A mis-association occurs when the SAA system incorrectly associates a measurement to the wrong intruder, causing large errors in the estimated intruder trajectories. The new methods described in this thesis can help ensure safe encounters between aircraft and enable SAA sensor certification for UAS integration into the National Airspace System.

CHAPTER 1

INTRODUCTION

1.1 The Need for Sense and Avoid

Since the early 1990's, unmanned aircraft systems (UAS) operations in the National Airspace System (NAS) have been limited to mostly public functions like military operations and border security [30]. Now UAS operations are rapidly expanding to include a much wider range of civil and public applications, including aerial photography, agriculture and communications [30].

The United States Department of Defense (DoD) is the largest operator of UAS in the world [17]. The DoD had gone from operating UAS on the order of hundreds of flight hours in 1996 to over six hundred thousand flight hours in 2011 [17, 18]. The DoD has a requirement to operate UAS in the NAS to meet operational military taskings, such as those from US Northern Command, but also missions that relate to homeland defense, border and port surveillance, and disaster support [17, 18].

There has also been great UAS growth in the commercial sector. Until the FAA establishes an airworthiness certification process for UAS to operate safely in the NAS, the FAA provides Section 333 exemptions to UAS on a case-by-case basis [33]. As of March 16, 2016, over 4,000 FAA Section 333 exemptions have been granted for commercial UAS operators [33]. In addition, the FAA is estimating the fleet of small UAS (those weighing less than 55 pounds) to increase from 32,800 in 2016 to over 540,000 in 2020 [33].

With this increased interest in UAS, the United States Congress mandated the Federal Aviation Administration (FAA), in Subtitle B of the *FAA Modernization and Reform Act of 2012*, to develop requirements necessary for broader UAS access into the NAS [81]. One of the challenges the FAA faces in meeting this mandate is

ensuring an acceptable level of safety. To do this, a UAS requires a “sense and avoid” (SAA) capability to provide self-separation (SS) and collision avoidance between the UAS and other aircraft analogous to the “see and avoid” responsibility for pilots of manned aircraft [30]. The *FAA Modernization and Reform Act of 2012* defines SAA capability as the capability of an unmanned aircraft to remain a safe distance from and to avoid collisions with other airborne aircraft [81].

Depending on the class of controlled airspace, if an intruder aircraft is cooperative, that is, employing an operating transponder or Automatic Dependent Surveillance - Broadcast (ADS-B) device [34], air traffic control (ATC) may provide separation. Alternatively, a manned aircraft pilot could employ a Traffic Collision Avoidance System (TCAS) as a situational awareness aid to help the pilot detect the intruder then initiate an avoidance maneuver. Otherwise, if the intruder aircraft is non-cooperative, without an operating transponder or ADS-B, the manned aircraft pilot will not have the help of ATC or TCAS. In this manned aircraft case, it is solely the pilot’s responsibility to visually see the intruder and maneuver to maintain separation. Anderson, et al., comprehensively detail how the US Code of Federal Regulations (CFR) 14 CFR 91 relates to a pilot’s “see and avoid” responsibility [4].

Since UAS will not have a pilot on board, it will have to replicate the functionality of pilot vision through an appropriate sensor. Non-cooperative SAA sensors include radar, Laser/Light Detection and Ranging (LIDAR), electro-optical (EO), acoustic, and infrared (IR) [84, 85]. The sensor must adequately inform the UAS SAA system whether or not a separation maneuver is required.

1.2 Self-Separation and Collision Avoidance

Although self-separation (SS) is a widely recognized term by the FAA and International Civil Aviation Organization (ICAO), it has never been fully codified

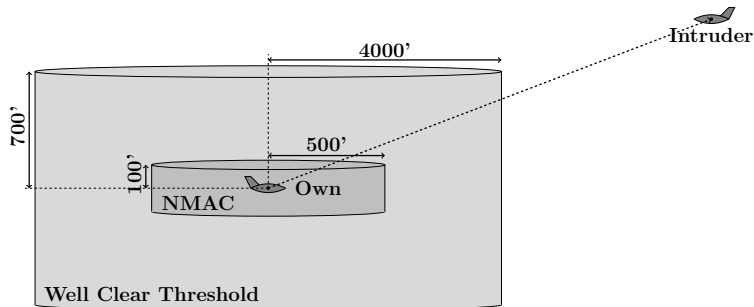


Figure 1.1. Well Clear Threshold and NMAC (Not to Scale)

[31]. “Well clear” is a subjective term in the right-of-way rules, 14 CFR 91.113 [1,4]. In 2011, Weibel, et al., proposed well clear as an objective separation standard [83]. In 2013, the Second FAA SAA Workshop concluded that the concept of well clear is an airborne separation standard [31]. The most recent guidance for a well clear threshold (WCT) is the Radio Technical Commission for Aeronautics (RTCA) Special Committee-228 (SC-228), who in their latest draft of the Detect and Avoid (DAA) Minimum Operational Performance Standards (MOPS), defined the well clear threshold as a modified “tau” (τ_{mod}), or time to closest point of approach (CPA), of 35 seconds, a horizontal miss distance (MD) of 4000 feet, and a vertical miss distance of ± 450 feet [72].

When an intruder cannot remain well clear, a collision avoidance maneuver is required to avoid a near mid-air collision (NMAC). NMAC boundaries are typically 500 feet laterally and 100 feet vertically from the own aircraft [31]. If the intruder aircraft is non-cooperative, it is up to the sense and avoid system to provide the appropriate collision avoidance maneuver. Figure 1.1 depicts the conceptual difference between the well clear threshold and near mid-air collision distance thresholds (not to scale and not accounting for τ_{mod}). For simplicity, this paper will concentrate on self-separation and the well clear threshold. The methodology is the same for collision avoidance and NMAC.

1.3 Evolution of the Well Clear Threshold

As previously mentioned, “well clear” is a subjective term in the right-of-way rules, 14 CFR 91.113 [1, 4]. In 2011, Weibel, et al., of the Massachusetts Institute of Technology (MIT) Lincoln Laboratory (LL) was among the first to propose well clear as an objective separation standard [83]. In 2013, the Second FAA SAA Workshop concluded that the concept of well clear is an airborne separation standard [31]. Also in 2013, Lee, et al., of the National Aeronautics and Space Administration (NASA) Ames Research Center demonstrated a capability, using the NASA Airspace Concept Evaluation System (ACES) model, to determine the rate of well clear violations for various definitions [53]. In 2014, Munoz, et al., of NASA’s Langley Research Center evaluated four different versions of tau, the time to horizontal closest point of approach, and developed detection algorithms for a family of well clear boundary models [57]. In June of 2013, the RTCA SC-228 UAS SAA Science and Research Panel (SARP) was tasked with recommending a quantitative definition for UAS Well Clear [14].

1.3.1 RTCA Special Committee-228. RTCA is a federal advisory committee that responds to FAA requests for technical standard recommendations. RTCA Special Committees incorporate academic, government, and industry members of the aviation community to generate these recommendations. In May of 2013, SC-228 was founded and was tasked to develop Minimum Operational Performance Standards (MOPS) for UAS DAA equipment and command and control (C2) data links [69]. Note DAA and SAA are synonymous terms.

1.3.2 SC-228 SARP Recommendation. The SC-228 SARP evaluated three proposed well clear thresholds: one from the MIT LL, one from NASA, and one from the Air Force Research Laboratory (AFRL). The NASA well clear threshold used a modified tau (τ_{mod}), which is the time to closest point of approach modified

with a distance modifier to account for slow closure rates, of 30 seconds, a horizontal miss distance of 6000 feet, a vertical separation of ± 475 feet, and a vertical time to co-altitude of 20 seconds [14]. The AFRL proposal projected variable wedge-shaped sector volumes that varied in altitude between 450 and 600 feet [14]. Ultimately, in August 2014, the SARP recommended the MIT LL proposal, defining well clear as having a horizontal time to closest point of approach (CPA), τ , of 35 seconds, a horizontal miss distance of 4000 feet and a vertical miss distance of ± 700 feet [14].

1.3.3 Detect and Avoid Minimum Operational Performance Standards.

The Detect and Avoid Minimum Operational Performance Standards is a technical standards document. In September 2015, SC-228 released the first version of the draft Detect and Avoid Minimum Operational Performance Standards, expected to be finalized in July 2016. The current draft of the Minimum Operational Performance Standards redefined the well clear threshold by introducing the term loss of detect and avoid well clear (DWC). The well clear threshold and the threshold defined by a loss of detect and avoid well clear are synonymous. The Minimum Operational Performance Standards further addressed the hazard associated with a loss of well clear by defining what it calls a warning alert, whose threshold is essentially the same as the loss of detect and avoid well clear [72]. The latest draft of the Detect and Avoid Minimum Operational Performance Standards ultimately redefined the well clear threshold as a modified tau of 35 seconds, a horizontal miss distance of 4000 feet, and a vertical miss distance of ± 450 feet [72].

1.4 Problem Statement

Sense and avoid safety needs to be guaranteed. This requires methods to quantify safety performance as a function of sensor uncertainty. In response, this thesis introduces *integrity risk* and *continuity risk* as new UAS SAA safety performance metrics. Integrity and continuity risk are absolute safety metrics [45, 71] as opposed

to the current relative UAS safety performance metrics, such as risk ratios, the failure rate with the SAA system divided by the failure rate without the SAA system [31]. The new methods in this work that evaluate integrity and continuity risk can be used to establish sensor performance requirements to ensure a predefined level of safety. These high-level requirements apply to any candidate sensor or sensor suite. This research also maps and bounds the trade space of requirements necessary to maintain desired integrity and continuity.

1.5 Prior Work

There have been several papers that provide overviews of the SAA problem. Yu and Zhang present the current state of the entire SAA problem, denoting current SAA sensors, decision algorithms, path planning, and path following with a journal literature review [84]. Previous comprehensive reviews of the UAS integration into the NAS problem include [15, 22, 64]. Kuchar and Yang outlined what at the time was an overview of air traffic conflict detection and resolution models [51]. Prior work focusing on development of the WCT are explained in section 1.3.

Much of the previous work has tended to focus on risk ratio safety studies that derive from the development of the ubiquitous TCAS. McLaughlin and Zeitlin described a MITRE safety study that used encounter models to build collision avoidance risk ratios to determine the safety of TCAS version 6.4 [56]. Espindle, et al., described an MIT LL safety study that used encounter models to build collision avoidance risk ratios to determine the safety of TCAS version 7.1 [26]. The Second SAA Workshop determined, using methodology described in the International Civil Aviation Organization (ICAO) Doc 9689, that UAS SAA systems should have two target levels of safety (TLS) based on catastrophic collision risk ratios: 10^{-9} midair collisions (MAC) per flight hour (FH) for cooperative airspace (where transponders are required) and 10^{-7} MAC/FH for all other airspace [31, 38].

A concentration of prior work came from the MIT LL. Kochenderfer, et al., developed an aircraft encounter model used to evaluate safety of collision avoidance systems using NMAC rate and risk ratio, which is defined as the NMAC rate with the collision avoidance system divided by the NMAC rate without the collision avoidance system [48–50]. Kochenderfer, Chryssanthacopoulos, and Billingsley of the MIT LL looked at state uncertainty of a collision avoidance system, quantifying safety as probability of NMAC accounting for avoidance maneuvers, and applying Markov decision processes for collision avoidance [10, 13]. Heisley, et al., of the MIT LL developed an architecture with a future intent to test and certify SAA systems [37]. Owen, et al., of the MIT LL demonstrated and flight tested an approach to developing SAA radar models for requirements derivations that employed a phased-array technology [60]. Edwards and Owen of the MIT LL validated a radar-based SAA concept through modeling and flight test [24].

Also, the Air Force Research Laboratory (AFRL) and the Air Force Institute of Technology (AFIT) have made many contributions to SAA. Shakernia, et al., of Northrop Grumman, in conjunction with AFRL, examined passive ranging techniques (involving benign own aircraft maneuvers) to compensate for EO SAA sensor ranging shortfalls [75]. In late 2006, AFRL flight tested an early SAA system based on EO cameras combined with the self-maneuvering passive ranging techniques [74]. In 2009, AFRL conducted a flight test of their Multi-Sensor Integrated Conflict Avoidance (MuSICA) SAA system which included sensor fusion from ADS-B, TCAS, radar and EO [12, 36]. In addition, AFIT and AFRL researched UAS collision avoidance trajectories that minimized the deviation from intended flight path while using a particle filter to track multiple intruders [77–80].

Some other prior work of note include the following. Kim, et al., of the Korean Pusan National University designed a 3D EO system for small UASs using a Kalman

filter, Sequential Quadratic Programming, and Linear Parameter Varying approaches for tracking and measurement error reduction [47]. Lee, et al., of NASA Langley constructed a distributed traffic model to enable a probabilistic approach to risk assessment by computing collision rates based on Predator training missions in the Grand Forks Air Force Base area [52]. Munoz, et al., of NASA Langley presented DAIDALUS (Detect and Avoid Alerting Logic for Unmanned Systems), a reference SAA concept implementation, which is also outlined in Appendix G of the DAA MOPS [58, 72].

This research describes a different approach than the prior work, focusing directly on the accepted aviation navigation certification standards that quantify integrity and continuity as safety factors [39]. Integrity risk and continuity risk are absolute safety metrics, which can be used to set certifiable requirements on individual system components, such as SAA sensors, to achieve and prove an overall level of safety [45, 71]. For example, for the Local Area Augmentation System (LAAS), an all-weather aircraft landing system, integrity requirements specify that, at near-zero visibility, no more than one undetected hazardous navigation system failure is allowed in a billion approaches [71]. Kelly and Davis broke down their proposed target level of safety for required navigation performance (RNP) into accuracy, integrity, and continuity requirements [46], which are three of the four parameters that quantify navigation system performance (the other being availability) [46, 65]. This research focuses on integrity and continuity because they are the most difficult requirements for avionics systems to achieve.

1.6 Integrity Risk

Kelly and Davis defined integrity as the trust that can be placed in the correctness of information supplied by the system [46]. Enge states that integrity fails when position error exceeds a predefined alert limit but an alert is not sounded to

the pilot or guidance system within a specified time [25]. Integrity risk can be quantified by probability of such a missed detection [25,54,62]. More specifically, integrity risk is quantified as the probability that the system provides Hazardously Misleading Information (HMI) [25,76], which is an unacceptably large error without a timely warning that the system cannot be trusted [65]. For the SAA problem, HMI occurs when the SAA system is not sensing a hazard (and not alerting to maneuver) but in fact, a hazard is present and a self-separation maneuver is required.

The Second SAA Workshop Caucus concluded that the hazard severity classification is always “catastrophic” for collision avoidance and always “major” for failing to maintain well clear [31]. According to FAA Advisory Circular (AC) 25.1309-1A, catastrophic failure conditions must be “extremely improbable” and major failure conditions must be “improbable” [28]. It goes on to define extremely improbable failure conditions as having probability on the order of 10^{-9} or less and improbable failure conditions as having probability between 10^{-5} and 10^{-9} [28]. Based on those definitions, SAA integrity risk requirements can be selected for self-separation and collision avoidance. The self-separation integrity risk should be between 10^{-5} and 10^{-9} and the collision avoidance integrity risk should be 10^{-9} or less.

1.7 Continuity Risk

Kelly and Davis defined continuity as the ability of the total system to perform its function without nonscheduled interruptions [46]. Enge states that continuity fails when an aircraft operation is aborted for any unscheduled reason [25]. The major contributor to continuity risk is typically the probability of false alert (FA) [25,54,62,63,65]. For the SAA system, FA’s occur when alerts to maneuver are issued when no separation hazards are present. When FA’s occur, the potential exists for the UAS to maneuver unexpectedly, resulting in, at best, increased workloads for ATC and pilots of potential intruders or, at worst, an induced self-separation or collision

avoidance hazard with a different intruder. For the purposes of this research, loss of continuity will be classified as a minor hazard, and should occur with a probability no greater than 10^{-5} [28].

1.8 Multiple Intruders and Data Association

The multiple intruder problem is treated as a data association problem, determining if each measurement is correctly associated with the right intruder. Data association is a field extensively covered throughout the last half century [7, 8, 66]. There is uncertainty in data association when there is uncertainty in whether a sensor measurement's origin is a target of interest [7]. There are many algorithms to address data association, including the probabilistic data association filter (with joint and mixture reduction variants) [7], particle filter [77], multiple hypothesis tracker [61], Markov chain Monte Carlo [59], and nearest neighbor method [7]. Many of these methods are computationally expensive. As an example application, Smith, et al., researched UAS collision avoidance trajectories that minimized the deviation from intended flight path while using a particle filter to track multiple intruders [77–80]. However, since the particle filter has an increased computational cost (due to the propagation of large populations of particles) [77], this research will employ a Kalman filter instead of a particle filter.

Also, for computational efficiency, this research will employ one of the simplest available heuristic data association methods, the nearest neighbor, which relies on the Mahalanobis distance metric [7]. The Mahalanobis distance is the square of the norm of the error with respect to the covariance [6, 7, 55]. The nearest neighbor method applies the Mahalanobis distance for measurement-to-track and track-to-track associations [6, 7]. There are many different variations of the nearest neighbor algorithm, to include local nearest neighbor, global nearest neighbor, and k-nearest neighbor approaches, among others [3, 5, 19, 67]. The multiple intruder problem outlined in

this work matches closest to the global nearest neighbor algorithm. However the numerical methods required to determine the probability of incorrect association of a global nearest neighbor are computationally expensive and can be inaccurate for the numbers of degrees of freedom in this research [6]. Instead, this thesis develops a new innovation-based, computationally efficient analytical method to bound the probability of incorrect association to determine integrity risk of multiple intruders.

1.9 Dissertation Contributions

There are five main contributions to knowledge in this thesis. These contributions are outlined in the following subsections.

1.9.1 Integrity Risk Methodology. The first contribution of this work is the development of an integrity risk evaluation methodology to quantify SAA safety. Previous research into SAA safety has focused on relative safety metrics, such as risk ratios, which is a failure rate with the SAA system divided by the failure rate without the SAA system [48]. The approach in this thesis is different, focusing directly on the accepted aviation navigation certification standards, such as those in the LAAS Minimum Aviation System Performance Standards for aircraft approach navigation, that quantify integrity and continuity as safety factors [39,71]. Integrity is an absolute safety metric, which can be used to set certifiable requirements on individual system components, such as SAA sensors, to achieve and prove an overall level of safety [45, 71].

1.9.2 Continuity Risk Methodology. Another contribution of this thesis is development of a continuity risk evaluation methodology to quantify SAA safety. Accepted aviation navigation certification standards quantify continuity, as well as integrity, as safety factors [39]. Like integrity, continuity is an absolute safety metric, which can be used to set certifiable requirements on individual system components,

such as SAA sensors [45, 71].

1.9.3 Relating Integrity and Continuity Risk to Sensor Requirements.

The integrity risk methodology and the continuity risk methodology together result in a protection volume surrounding the own aircraft that inflates the WCT. This inflation results in a tradeoff between SAA safety and airspace capacity requirements. To minimize the impact on airspace capacity, an operational limit is placed on the protection level, resulting in restrictions on sensor performance. A sensitivity analysis explores the sensor requirement trade space for a given operational limit.

1.9.4 Accounting for Linear Accelerations. The trajectory state estimation model used to build the integrity and continuity risk methodology is based on a constant velocity assumption. As outlined in the DAA MOPS, the following statement is repeated for ownship and intruder: “it is assumed that an ownship/intruder track prediction will initiate at the ownship’s/intruder’s current position and be produced using the estimates of ownship/intruder states extrapolated using constant horizontal and vertical velocities” [72]. This assumption is removed and the estimation model accounts for constant accelerations. There is limited prior work on SAA that accounts for uncertainties in intruder dynamics. Barreiro, et al., from NASA Ames, conducted a preliminary investigation into a probabilistic approach for small UAS (less than 55 lbs) SAA intruder path planning, accounting for potential intruder pilot actions based on routes, traffic patterns, topography, airspace, weather information, and observed communications [9].

This thesis evaluates linear intruder accelerations for large UAS, based on sensor measurements. Only linear intruder accelerations are evaluated, leaving turning and leveling intruder trajectories for future work. A linear acceleration-specific analysis explores the sensor trade space.

1.9.5 Accounting for Multiple Intruders. The final contribution of this thesis is accounting for multiple intruders. A general nearest neighbor innovation-based methodology is employed resulting in the development of a new methodology to analytically upper bound the probability of mis-associating any number of intruders. A mis-association means the SAA system incorrectly associates a measurement to the wrong intruder, resulting in estimation errors that impact integrity risk if one of the intruders violates the well clear threshold. A multiple intruder-specific analysis explores the sensor trade space.

1.10 Dissertation Outline

After this introductory chapter, Chapter 2 uses the Detect and Avoid Minimum Operational Performance Standards well clear threshold definition to develop hazard states that define the self-separation hazard. Chapter 3 develops the methodology for determining and applying integrity risk. Chapter 4 describes the methodology for determining and applying continuity risk. Chapter 5 relates the integrity and continuity risk methodology to sensor requirements. Chapter 6 includes a sensitivity analysis depicting an example two dimensional encounter and an example three dimensional encounter to examine trade-offs between integrity and continuity risk, sensor uncertainty, intruder trajectories, and sample rates. Chapter 7 introduces the methodology to account for intruder linear accelerations and compares the modified tau (the modified time to closest point of approach), which does not address accelerations, with an accelerating version of true tau (the actual horizontal time to closest point of approach). Chapter 8 develops the methodology to account for multiple intruders, adjusting integrity based on the probability of mis-association. Finally, Chapter 9 provides conclusions and opportunities for future research.

CHAPTER 2

HAZARD STATE ESTIMATION

This chapter uses the draft Detect and Avoid (DAA) Minimum Operational Performance Standards (MOPS) definition for a SAA self-separation (SS) hazard to derive the hazard states necessary for developing the SAA integrity and continuity risk evaluation methodology introduced in the following two chapters. DAA and SAA are synonymous terms. The DAA MOPS is a technical standards document written by the Radio Technical Commission for Aeronautics (RTCA) Special Committee-228 (SC-228). RTCA is a federal advisory committee that responds to FAA requests for technical standard recommendations. RTCA Special Committees incorporate academic, government, and industry members of the aviation community to generate these recommendations. SC-228 is specifically tasked to develop MOPS for UAS.

There are two ways the DAA MOPS describes the hazard associated with a UAS failing to self-separate. The first description of this hazard is what the DAA MOPS calls a loss of DAA Well Clear (DWC) and the second description of the hazard is what it calls a warning alert [72]. The thresholds that define loss of DWC and the well clear threshold (WCT) are synonymous. The *hazard states* are the variables that define the loss of DWC and the warning alert. Based on the DAA MOPS, this thesis will use three hazard states: modified tau (or modified time to horizontal closest point of approach), horizontal closest point of approach (CPA), and predicted vertical separation. This chapter will define and explain the hazard states.

A detailed explanation of intruder trajectories, the constant velocity measurement model, and intruder trajectory state estimation processes is in Appendix A. A discussion of alternate hazard states is presented in Appendix B.

2.1 Intruder Trajectory Estimation

This section provides some background as to how the sense and avoid problem is defined in this thesis. The intent is to define some terms and provide context for the subsequent sections.

The sense and avoid problem is presented as a three dimensional, two-body problem. The two bodies are the own aircraft and the intruder aircraft. The coordinate frame is an own-aircraft-centered body frame. Figure 2.1 is a graphical depiction of the own aircraft and the intruder aircraft encounter looking down from the top (on the left) and looking from the side (on the right). In the horizontal plane, the x and y axes are oriented such that the x -axis is directly out of the nose of the own aircraft. The azimuth, θ , is the angle counterclockwise from the x -axis to the horizontal range vector, \mathbf{r} (from the origin to the intruder position on the xy -plane). In the vertical plane, ϕ is the elevation angle from the horizontal range vector up to the slant range vector, ρ :

$$\cos \phi = \frac{r}{\rho} \quad (2.1)$$

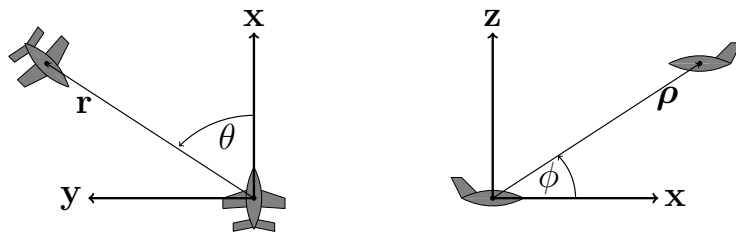


Figure 2.1. Horizontal and Vertical Position of the Intruder Aircraft

For this thesis, the intruder *trajectory states*, \mathbf{x}_n , are the relative Cartesian intruder position and constant velocity:

$$\mathbf{x}_n = \begin{bmatrix} x_n & y_n & z_n & \dot{x} & \dot{y} & \dot{z} \end{bmatrix}^T \quad (2.2)$$

where n is the current epoch. The constant velocity assumption here is based on

the draft DAA MOPS, where it is assumed that intruder track prediction will be extrapolated using constant velocity [72].

SAA sensors can measure the intruder’s relative position (with error) in spherical, Cartesian, or cylindrical coordinates. In the draft Detect and Avoid Minimum Operational Performance Standards, the input intruder measurements from a sense and avoid radar includes relative slant range (ρ), relative range rate ($\dot{\rho}$), relative bearing (θ), and elevation angle (ϕ) [72]. As a result, this thesis will assume intruder measurements (\mathbf{z}_n) of range, range rate, azimuth angle and elevation angle as expressed in equation (2.3):

$$\mathbf{z}_n = \begin{bmatrix} \rho_n & \theta_n & \phi_n & \dot{\rho}_n \end{bmatrix}^T \quad (2.3)$$

The estimation algorithm in this thesis will employ a Kalman filter, which is more computationally efficient than a batch process. A comparison of the two estimation processes can be found in Appendix A.

2.2 DAA Well Clear and Alerting Threshold

The distance and time defining a self-separation hazard was previously described as a well clear threshold (WCT) or well clear boundary [14, 57, 83]. In 2011, Weibel and his colleagues at the MIT Lincoln Laboratory recommended well clear as a separation standard and presented candidate definitions for well clear boundaries [83]. In 2014, Munoz and his colleagues from the NASA Langley Research Center presented a family of well clear boundary models [57]. In 2014, Cook and his team from the SC-228 UAS SAA Science and Research Panel (SARP), recommended a Well Clear Threshold definition after examining three candidates: one from NASA, one from the MIT Lincoln Laboratory, and one from the Air Force Research Laboratory (AFRL) [14].

However, in the draft DAA MOPS, SC-228 expanded on the SARP recommendation and adapted the term detect and avoid well clear (DWC) to describe this self-separation standard [72]. More specifically, the Minimum Operational Performance Standards defines a loss of DWC in the following equation:

$$\text{Loss of DWC} = (0 \leq \tau_{mod} \leq \tau_{SS}) \cap (r_{CPA} \leq r_{MD}) \cap (|z| \leq z_{MD}) \quad (2.4)$$

This means a loss of detect and avoid well clear occurs when modified tau (τ_{mod}) is at or within the tau threshold (τ_{SS}) *and* the horizontal CPA (r_{CPA}) is at or within the horizontal miss distance (HMD) threshold (r_{MD}) *and* the current vertical separation (z) is at or within plus/minus the vertical separation threshold (z_{MD}).

Figure 2.2 is a top-view depiction of the CPA. For a loss of DWC, there has to be a time n , when z_n has to be at or within the vertical miss distance, $\pm z_{MD}$, while the r_{CPA} is at or within the required horizontal miss distance (MD), r_{MD} , and τ_{mod} is at or within the self-separation threshold, τ_{SS} . All must be true simultaneously. If only z_{MD} is violated, the intruder could be co-altitude, but hundreds of miles away. Conversely, if only r_{MD} is violated, the intruder could be directly above or below the own aircraft, but off altitude by several thousand feet.

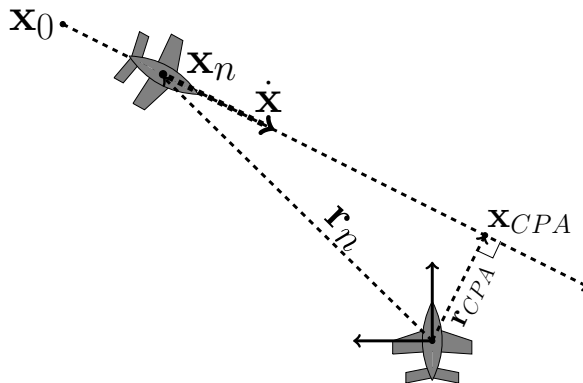


Figure 2.2. Overhead View of Closest Point of Approach

The DAA MOPS also defines alerting thresholds for Preventive, Corrective, and Warning Alerts. In each case, the intruder is considered within an alerting threshold when at any point within the alerting look-ahead time the predicted $\tau_{mod} \leq \tau_{SS}$ and the predicted $r_{CPA} \leq r_{MD}$ and the predicted vertical separation (z_p) is at or within $\pm z_{MD}$. This is described in the following equation:

$$\text{Alert Event} = (0 \leq \tau_{mod} \leq \tau_{SS}) \cap (r_{CPA} \leq r_{MD}) \cap (|z_p| \leq z_{MD}) \quad (2.5)$$

The DAA MOPS terminology is confusing in relation to alerting thresholds. For example, it describes a “predicted r_{CPA} ” as an alerting condition, however, the r_{CPA} itself is a predictive state based on the intruder position and velocity. The different Alerting Thresholds are presented in Table 2.1, which is directly from the DAA MOPS DAA Alert Summary Table 2-20 [72].

Table 2.1. DAA MOPS Alert Summary [72]

Alert Type	Alert Level	Must Alert Threshold			
		Lookahead Time	τ_{SS}	D_{mod}, r_{MD}	z_{MD}
Preventive	Caution	55s	35s	0.66 NM	700 ft
Corrective	Caution	55s	35s	0.66 NM	450 ft
Warning	Warning	25s	35s	0.66 NM	450 ft

Since the warning alert is the most restrictive and matches the DWC thresholds, the hazard states will be defined based on the DAA Warning Alert. Therefore, the hazard states are τ_{mod} , r_{CPA} , and z_p . The corresponding thresholds are $\tau_{SS} = 35$ s, $r_{MD} = 4000$ feet = 0.66 NM, and $z_{MD} = 450$ feet [72]. The lookahead time of 25 seconds will be used to define z_p .

For a hazard to cause a warning alert, the following three events must simultaneously occur:

- The trajectory horizontal CPA, r_{CPA} , must be within the r_{MD}
- The intruder trajectory must vertically cross within $\pm z_{MD}$ within 25 seconds
- τ_{mod} must be less than or equal to τ_{SS} within 25 seconds ($\tau_{mod} - 25s \leq \tau_{SS}$)

2.3 Modified Horizontal Time to CPA

Modified tau, τ_{mod} , is the actual (or true) time to horizontal closest point of approach with an added safety factor [70]. *True tau*, τ_{true} , is the actual time to horizontal closest point of approach assuming unaccelerated flight by both own aircraft and the intruder [70]. The DAA MOPS defines modified tau as follows for closing geometries [72]:

$$\tau_{mod} = \frac{-(r^2 - D_{mod}^2)}{r\dot{r}} = \frac{D_{mod}^2 - r^2}{x\dot{x} + y\dot{y}} \quad (2.6)$$

where r is the relative intruder horizontal range, \dot{r} is the relative intruder horizontal range rate, x and y are the relative intruder Cartesian horizontal position distances and \dot{x} and \dot{y} are the relative intruder Cartesian horizontal velocities.

D_{mod} is the distance modification, which is set equal to the horizontal miss distance threshold, r_{MD} . If $D_{mod} \neq r_{MD}$, the DAA MOPS explains that “alerts may oscillate on and off with un-accelerating ownship and intruder, which is an undesired behavior” [72]. The intent behind D_{mod} has several different explanations depending on the source. These definitions are chronicled in Appendix C.

Since $r = \sqrt{x^2 + y^2}$, modified tau can be defined completely as a function of the trajectory states:

$$\tau_{mod} = \frac{D_{mod}^2 - x^2 - y^2}{x\dot{x} + y\dot{y}} \quad (2.7)$$

2.3.1 True Tau. To get the Actual Time to Horizontal CPA, τ_{true} , in terms of

trajectory states, the following two equations need to be solved:

$$\begin{bmatrix} x_n \\ y_n \end{bmatrix} + \tau_{true} \begin{bmatrix} \dot{x} \\ \dot{y} \end{bmatrix} = \begin{bmatrix} x_{CPA} \\ y_{CPA} \end{bmatrix} \quad (2.8)$$

$$\begin{bmatrix} \dot{x} \\ \dot{y} \end{bmatrix} \cdot \begin{bmatrix} x_{CPA} \\ y_{CPA} \end{bmatrix} = 0 \quad (2.9)$$

The first equation reflects the distance from the current horizontal position to the horizontal CPA as a sum of position and τ times horizontal velocity. The second equation, which is the dot product of horizontal Cartesian velocity vector and the horizontal Cartesian closest point of approach vector, expresses that these two vectors are perpendicular. Combining these equations results in three equations and three unknowns:

$$\begin{bmatrix} 1 & 0 & -\dot{x} \\ 0 & 1 & -\dot{y} \\ \dot{x} & \dot{y} & 0 \end{bmatrix} \begin{bmatrix} x_{CPA} \\ y_{CPA} \\ \tau_{true} \end{bmatrix} = \begin{bmatrix} x_n \\ y_n \\ 0 \end{bmatrix} \quad (2.10)$$

The resulting three unknowns, x_{CPA} , y_{CPA} , and τ_{true} can be computed using the following equations:

$$\begin{bmatrix} x_{CPA} \\ y_{CPA} \end{bmatrix} = \begin{bmatrix} x_n + \tau_{true}\dot{x} \\ y_n + \tau_{true}\dot{y} \end{bmatrix} \quad (2.11)$$

$$\tau_{true} = \frac{-(\dot{x}x_n + \dot{y}y_n)}{\dot{x}^2 + \dot{y}^2} \quad (2.12)$$

2.4 Horizontal Closest Point of Approach

There are two ways to determine the Horizontal CPA, r_{CPA} . One is the-time

based definition in the DAA MOPS and the other is geometrically determined based on a linear intruder trajectory. The time-based horizontal CPA from the DAA MOPS is [72]:

$$r_{CPA} = \sqrt{x_{CPA}^2 + y_{CPA}^2} = \sqrt{(x_n + \tau_{true}\dot{x})^2 + (y_n + \tau_{true}\dot{y})^2} \quad (2.13)$$

The geometric r_{CPA} is derived in Appendix D. Geometric r_{CPA} will prove useful in Chapter 7, where the constant velocity assumption is removed, but the linear trajectory remains. The expression for r_{CPA} is:

$$r_{CPA} = \sqrt{x_{CPA}^2 + y_{CPA}^2} = \frac{\dot{y}x - \dot{x}y}{\sqrt{\dot{x}^2 + \dot{y}^2}} \quad (2.14)$$

when factoring out τ_{true} in equation (2.13), equation (2.13) reduces to equation (2.14).

2.5 Predicted Vertical Separation

To account for the warning alert criteria in the DAA MOPS, there needs to be a predicted vertical separation that can lookahead up to 25 seconds. This can be accounted for in the following equation:

$$z_p = z_n + p\Delta t\dot{z} \quad (2.15)$$

where p are the all the future epochs up to the 25 second lookahead time.

2.6 Hazard State Estimate and Estimate Error Variance

The trajectory state estimator in Appendix A produces a trajectory state estimate, $\hat{\mathbf{x}}_n$, from equation (A.29) and a Kalman filter estimate error covariance matrix, $\hat{\mathbf{P}}_n$, from equation (A.30). The hazard state estimate vector $\hat{\boldsymbol{\psi}}_n$ at epoch n is:

$$\hat{\boldsymbol{\psi}}_n = \begin{bmatrix} \hat{\tau}_{mod,n} & \hat{r}_{CPA,n} & \hat{z}_{p,n} \end{bmatrix}^T \quad (2.16)$$

A first order Taylor series expansion is used to obtain the linearized approximation of the hazard state estimates in relation to the trajectory state estimates ($\hat{\mathbf{x}}_n$):

$$\hat{\boldsymbol{\psi}}_n \approx \mathbf{A}_n \hat{\mathbf{x}}_n \quad (2.17)$$

where \mathbf{A}_n are the Taylor Series partial derivative vectors ($\mathbf{a}_{\tau_n}^T$, $\mathbf{a}_{r_n}^T$, $\mathbf{a}_{z_n}^T$) stacked into one matrix:

$$\mathbf{A}_n = \begin{bmatrix} \mathbf{a}_{\tau_n}^T \\ \mathbf{a}_{r_n}^T \\ \mathbf{a}_{z_n}^T \end{bmatrix} \quad (2.18)$$

As an example of the partial derivative vectors, $\mathbf{a}_{\tau_n}^T$ is the vector of partial derivatives of τ_{mod} with respect to the trajectory states:

$$\mathbf{a}_{\tau_n}^T = \left[\left. \frac{\partial \tau_{mod,n}}{\partial x_n} \right|_{\bar{\mathbf{x}}} \quad \left. \frac{\partial \tau_{mod,n}}{\partial y_n} \right|_{\bar{\mathbf{x}}} \quad \left. \frac{\partial \tau_{mod,n}}{\partial z_n} \right|_{\bar{\mathbf{x}}} \quad \left. \frac{\partial \tau_{mod,n}}{\partial \dot{x}} \right|_{\bar{\mathbf{x}}} \quad \left. \frac{\partial \tau_{mod,n}}{\partial \dot{y}} \right|_{\bar{\mathbf{x}}} \quad \left. \frac{\partial \tau_{mod,n}}{\partial \dot{z}} \right|_{\bar{\mathbf{x}}} \right] \quad (2.19)$$

where $\bar{\mathbf{x}}$ is an a-priori estimate of the trajectory states. The partial derivative vectors $\mathbf{a}_{r_n}^T$ and $\mathbf{a}_{z_n}^T$ are found in the same manner. The hazard state partial derivatives with respect to the trajectory states are derived in Appendix G.

The full covariance matrix, $\mathbf{P}_{\tau r z_n}$, of the hazard state estimate vector, $\hat{\boldsymbol{\psi}}_n$, is determined by the following:

$$\mathbf{P}_{\tau r z_n} = \mathbf{A}_n \hat{\mathbf{P}}_n \mathbf{A}_n^T \quad (2.20)$$

$\mathbf{P}_{\tau r z_n}$ is fully populated so the hazard state estimates ($\hat{\tau}_{mod}$, \hat{r}_{CPA} , and \hat{z}_p) are correlated. The hazard state estimate variances σ_{τ}^2 , σ_r^2 , and σ_z^2 are the diagonal elements of $\mathbf{P}_{\tau r z_n}$.

2.7 Hazard State Estimate Summary

In this chapter, three hazard states were defined based on the DAA MOPS definitions for a loss of DWC and warning alerts. The hazard states are modified tau, horizontal CPA, and predicted vertical separation. These hazard states were defined as functions of the trajectory states, intruder relative position and velocity. Then the hazard state estimates and hazard state estimate error covariance matrix were developed, which are used for the validation the DAA MOPS and the development of SAA integrity and continuity risk evaluation methodologies, which occur in subsequent chapters.

CHAPTER 3

INTEGRITY RISK

The first contribution of this thesis is the introduction of integrity risk as an absolute metric to quantify SAA safety, as opposed to the relative safety metrics of the previous work. Integrity risk is quantified as the probability that the system provides Hazardously Misleading Information (HMI) [25, 76]. In the UAS SAA application, HMI occurs when a hazard is present, but the SAA system does not sense the hazard. This chapter builds the SAA integrity risk evaluation methodology by first examining integrity risk for one hazard state, then expanding the integrity risk evaluation methodology to all three hazard states.

3.1 Integrity Risk Based Solely on Tau

HMI occurs when a hazard exists, but that hazard is not sensed. Accounting for τ_{mod} only, a hazard exists when $\tau_{mod} \leq \tau_{SS}$. The hazard is not sensed if $\hat{\tau}_{mod} > \tau_{SS}$. This HMI leads the own aircraft to not maneuver when a self-separation maneuver is warranted.

It is assumed that measurement errors can be over-bounded in the cumulative distribution function (CDF) sense by Gaussian distributions. Using a linear estimator to determine trajectory states and hazard states, the hazard state estimate error distributions are then also over-bounded by normal distributions [16, 68].

The left curve in Figure 3.1 depicts the probability density function of the estimate, $\hat{\tau}_{mod}$, which has uncertainty due to the imperfect SAA sensors that take the noisy measurements that are used to estimate trajectory states and hazard states. When actual $\tau_{mod} = \tau_{SS}$, which is a hazard condition, there is an unacceptable 50% probability of estimated $\hat{\tau}_{mod}$ being above the threshold, a non-alerting HMI condition where the hazard is not sensed. This $\tau_{mod} = \tau_{SS}$ is the worst case condition since

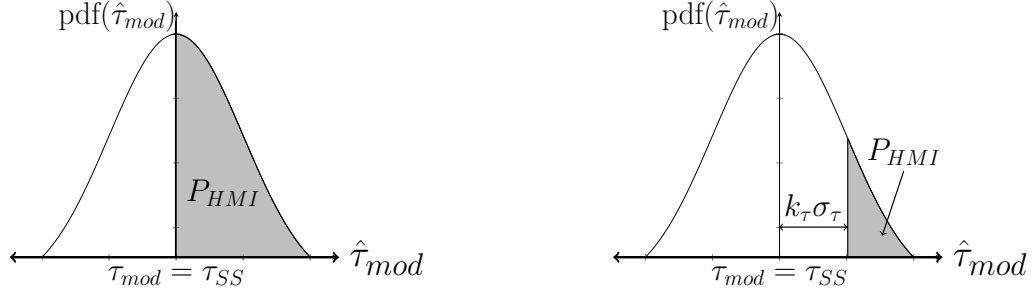


Figure 3.1. Integrity Risk and Adjusted Threshold

when $\tau_{mod} > \tau_{SS}$, there is no hazard, and when $\tau_{mod} < \tau_{SS}$, P_{HMI} is less than 50%.

To reduce the 50% P_{HMI} at this worst case ($\tau_{mod} = \tau_{SS}$), the threshold is adjusted by adding a multiple of the $\hat{\tau}_{mod}$ standard deviation, $k_{\tau}\sigma_{\tau}$, to the original threshold, τ_{SS} . The integrity coefficient, k_{τ} , is determined to ensure a predefined level of integrity, I_{τ} . In the right curve of Figure 3.1, the threshold is modified to $\tau_{SS} + k_{\tau}\sigma_{\tau}$. The hazard is now not sensed if the estimated time to closest approach, $\hat{\tau}_{mod}$, is greater than $\tau_{SS} + k_{\tau}\sigma_{\tau}$. In this case, the self-separation integrity risk is the probability of HMI, P_{HMI} :

$$P_{HMI} = P(\hat{\tau}_{mod} > \tau_{SS} + k_{\tau}\sigma_{\tau} | \tau_{mod} \leq \tau_{SS}) \quad (3.1)$$

P_{HMI} must meet a predefined integrity risk requirement, I_{τ} , that will be specified by the air certification authority's desired level of safety. For the shaded area in the right curve of Figure 3.1 to be I_{τ} , the multiplier k_{τ} is selected such that:

$$Q(k_{\tau}) = I_{\tau} \quad (3.2)$$

where $Q(x)$ is the tail probability of the standard normal distribution with zero mean

and unit variance:

$$Q(x) = 1 - \Phi(x) = \frac{1}{2} \left[1 - \operatorname{erf} \left(\frac{x}{\sqrt{2}} \right) \right] \quad (3.3)$$

and $\Phi(x)$ is the cumulative distribution function (CDF) for the standard normal distribution:

$$\Phi(x) = \frac{1}{2} \left[1 + \operatorname{erf} \left(\frac{x}{\sqrt{2}} \right) \right] \quad (3.4)$$

3.2 Integrity Risk for All Hazard States

In the previous section, only one hazard state was considered. Now, full self-separation integrity risk is based on all three hazard states.

As in the τ_{mod} only case, to ensure P_{HMI} meets the integrity risk requirement at the worst case for r_{CPA} and z_p ($r_{CPA} = r_{MD}$ and $z_p = \pm z_{MD}$), the thresholds are adjusted by adding multiples of the standard deviations (σ_r and σ_z) to the distance thresholds. The adjusted horizontal miss distance threshold is now $r_{MD} + k_r \sigma_r$, the adjusted vertical miss distance threshold is now $z_{MD} + k_z \sigma_z$ at the top vertical warning alert threshold, and the adjusted vertical miss distance threshold is now $-z_{MD} - k_z \sigma_z$ at the bottom vertical warning alert threshold. Now, the self-separation integrity risk is P_{HMI} :

$$\text{Sense No Hazard} = [\hat{\tau}_{mod} > \tau_{SS} + k_r \sigma_r \cup \hat{r}_{CPA} > r_{MD} + k_r \sigma_r \cup |\hat{z}_p| > z_{MD} + k_z \sigma_z] \quad (3.5)$$

$$\text{Hazard Exists} = [\tau_{mod} \leq \tau_{SS} \cap r_{CPA} \leq r_{MD} \cap |z_p| \leq z_{MD}] \quad (3.6)$$

$$P_{HMI} = P[\text{Sense No Hazard} | \text{Hazard Exists}] \quad (3.7)$$

In equation (3.7), the condition reflects an imminent (at or within τ_{SS} seconds) WCT violation (or loss of DWC) at the warning alert limit. **Hazard Exists** describes a condition where three events *occur simultaneously*:

- Actual time to CPA, τ_{mod} , is less than or equal to τ_{SS} .
- *And* actual horizontal CPA, r_{CPA} , is at or within r_{MD} .
- *And* actual predicted vertical separation, z_p , is at or within $\pm z_{MD}$.

In this case, the own aircraft should initiate a self-separation maneuver. **Sense No Hazard** describes a case where *any* of the following four events is occurring:

- Estimated time to CPA, $\hat{\tau}_{mod}$, is greater than the adjusted threshold $\tau_{SS} + k_r \sigma_r$.
- *Or* estimated horizontal CPA, \hat{r}_{CPA} , is beyond the adjusted threshold $r_{MD} + k_r \sigma_r$.
- *Or* estimated predicted vertical separation, \hat{z}_p , is above the adjusted threshold $z_{MD} + k_z \sigma_z$.
- *Or* estimated predicted vertical separation, \hat{z}_p , is below the adjusted threshold $-z_{MD} - k_z \sigma_z$.

Any one of these misleading estimates can cause HMI that leads the own aircraft to not maneuver when a self-separation maneuver is warranted. Figure 3.2 depicts a 2D HMI scenario, where the actual r_{CPA} is just within the r_{MD} threshold but the estimate \hat{r}_{CPA} is just beyond the adjusted threshold $r_{MD} + k_r \sigma_r$. The adjusted threshold ensures that this case occurs with a probability less than or equal to I_r (if I_r is allocated as an integrity requirement specifically for r_{CPA}).

P_{HMI} must meet a predefined integrity risk requirement for the SAA system, I_{SS} , that will be specified by the certification authority's desired level of safety. This integrity risk criterion for full self-separation is expressed as:

$$P_{HMI} \leq I_{SS} \tag{3.8}$$

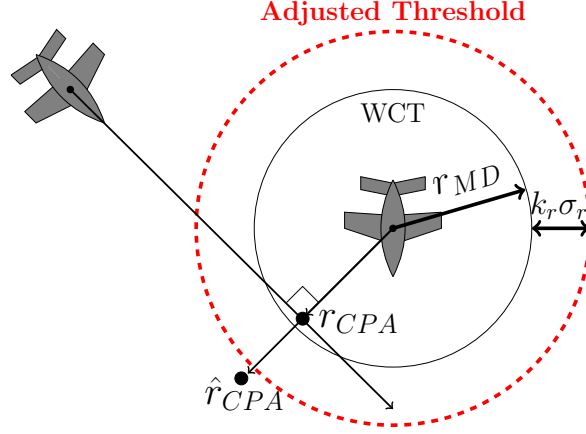


Figure 3.2. Worst Case HMI Scenario for r_{CPA}

The violation of the integrity limit, I_{SS} , reflects a higher than acceptable probability that a self-separation maneuver may be required, but the sensor estimate misleads the SAA system into not maneuvering. There is a single overall requirement, I_{SS} , that needs to be satisfied in equation (3.8). The following paragraphs describe a rigorous approach to establish an upper-bound on P_{HMI} , and to allocate I_{SS} to each hazard state. The approach is also computationally efficient.

The hazard state estimates $\hat{\tau}_{mod}$, \hat{r}_{CPA} , and \hat{z}_p will be correlated in general. P_{HMI} is a joint trivariate normal probability over the three hazard states:

$$P_{HMI} = \frac{1}{\sqrt{(2\pi)^3 |\mathbf{P}_{\tau r z}|}} \left(\int_{k_z \sigma_z}^{\infty} \int_{k_r \sigma_r}^{\infty} \int_{k_\tau \sigma_\tau}^{\infty} e^{-\frac{1}{2}[\psi' - \mu]^T \mathbf{P}_{\tau r z}^{-1} [\psi' - \mu]} d\tau' dr' dz' \right. \\ \left. + \int_{-\infty}^{-2z_{MD} - k_z \sigma_z} \int_{k_r \sigma_r}^{\infty} \int_{k_\tau \sigma_\tau}^{\infty} e^{-\frac{1}{2}[\psi' - \mu]^T \mathbf{P}_{\tau r z}^{-1} [\psi' - \mu]} d\tau' dr' dz' \right) \quad (3.9)$$

where ψ' is the vector of hazard state integration variables (τ' , r' , and z'):

$$\psi' = \begin{bmatrix} \tau' \\ r' \\ z' \end{bmatrix} \quad (3.10)$$

and $\boldsymbol{\mu}$ is the mean vector, which are the hazard state thresholds (τ_{SS} , r_{MD} , and z_{MD}):

$$\boldsymbol{\mu} = \begin{bmatrix} \tau_{SS} \\ r_{MD} \\ z_{MD} \end{bmatrix} \quad (3.11)$$

and $\mathbf{P}_{\tau r z}$ is the hazard state estimate error covariance matrix from equation (2.20). This trivariate normal distribution, centered at a mean vector value of the hazard state thresholds, represents the worst case at the top vertical separation threshold ($+z_{MD}$). The worst case at the bottom vertical separation threshold ($-z_{MD}$) is a mirror image of the worst case at the top and will have the same value as the P_{HMI} in equation (3.9).

To apply the integrity risk evaluation methodology, the coefficient k needs to be determined for each hazard state. The triple integral in equation (3.9) can be evaluated using computationally expensive numerical integration methods [21], which may not be numerically efficient nor computationally stable when evaluating each k coefficient. Also, in future work, when expanding this SAA methodology to online avoidance maneuvers, computational efficiency becomes paramount. Ground vehicles are more likely to carry the payload necessary to do heavy computations quickly. Aircraft, especially UAS, usually do not. For all these reasons, an easy-to-compute bound on P_{HMI} is used, which will be explained in the following paragraphs.

In 3D space, the error covariance matrix can be visualized as a trivariate normal distribution ellipsoid. To illustrate this idea, Figure 3.3 shows constant probability density ellipses in the 2D ($\hat{\tau}_{mod}$, \hat{r}_{CPA}) plane. The P_{HMI} is the joint CDF for this distribution bounded by $[k_r\sigma_r, \infty]$ in the $\hat{\tau}$ direction and $[k_r\sigma_r, \infty]$ in the \hat{r}_{CPA}

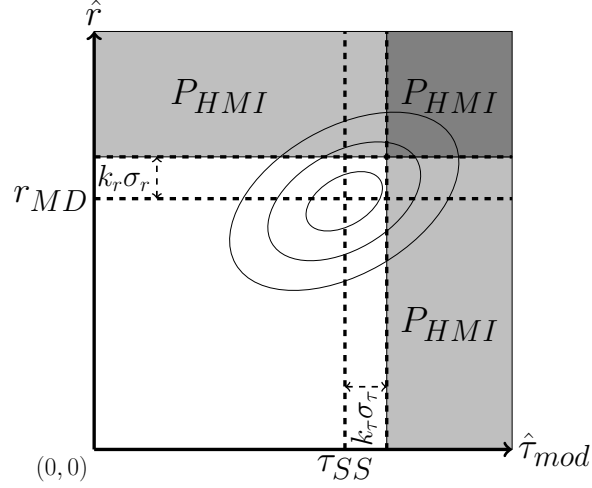


Figure 3.3. 2D Integrity Risk Correlation

direction. In 2D:

$$P_{HMI} = \frac{1}{2\pi\sqrt{|\mathbf{P}_{\tau r}|}} \int_{k_r\sigma_r}^{\infty} \int_{k_{\tau}\sigma_{\tau}}^{\infty} e^{(-\frac{1}{2}[\psi'_{\tau r} - \boldsymbol{\mu}_{\tau r}]^T \mathbf{P}_{\tau r}^{-1} [\psi'_{\tau r} - \boldsymbol{\mu}_{\tau r}])} d\tau' dr' \quad (3.12)$$

where $\boldsymbol{\psi}'_{\tau r}$ is the vector of the two hazard state integration variables (τ' and r'):

$$\boldsymbol{\psi}'_{\tau r} = \begin{bmatrix} \tau' \\ r' \end{bmatrix} \quad (3.13)$$

and $\boldsymbol{\mu}_{\tau r}$ is the mean vector of the two hazard state thresholds (τ_{SS} and r_{MD}):

$$\boldsymbol{\mu}_{\tau r} = \begin{bmatrix} \tau_{SS} \\ r_{MD} \end{bmatrix} \quad (3.14)$$

and $\mathbf{P}_{\tau r}$ is the $(\hat{\tau}_{mod}, \hat{r}_{CPA})$ covariance matrix. This bivariate normal distribution, centered at a mean vector value of the hazard state thresholds, represents the worst case. The double integral in equation (3.12) can also be evaluated using numerical

integration methods [21], requiring a computational load that may not be feasible for the onboard Unmanned Aircraft (UA) Detect and Avoid (DAA) Processor required by the MOPS [72]. According to the DAA MOPS, the UA DAA Processor “is located onboard the UA and evaluates track data from the airborne active surveillance transponder, ADS-B In and Air-to-Air radar” [72]. The current draft of the MOPS does not yet define the computational efficiency requirements for this processor.

In Figure 3.3, the probability of being in the shaded areas is the integrity risk, P_{HMI} . The probability of being in the shaded area to the right of the line $\tau_{mod} = \tau_{SS} + k_\tau \sigma_\tau$ is $Q(k_\tau)$. Likewise, the probability of being in the shaded area above the line $r_{CPA} = r_{MD} + k_r \sigma_r$ is $Q(k_r)$. The probability of being in the overlap region between these two shaded areas cannot be evaluated using Q-functions. Instead, an easy-to-compute bound on P_{HMI} is used, which is expressed as:

$$P_{HMI} \leq Q(k_\tau) + Q(k_r) \quad (3.15)$$

The bound in equation (3.15) accounts for the probability of being in the overlapping upper-right, shaded quadrant twice, which is conservative, hence the inequality.

Extending this bounding to the full 3D case, the integrity risk is upper bounded by the following:

$$P_{HMI} \leq Q(k_\tau) + Q(k_r) + Q(k_z) + Q\left(k_z + \frac{2z_{MD}}{\sigma_z}\right) \quad (3.16)$$

To ensure equation (3.8) is satisfied, this integrity risk upper bound must be less than or equal to the integrity risk requirement:

$$Q(k_\tau) + Q(k_r) + Q(k_z) + Q\left(k_z + \frac{2z_{MD}}{\sigma_z}\right) \leq I_{SS} \quad (3.17)$$

This integrity risk upper bound includes all overlaps between $Q(k_\tau)$, $Q(k_r)$ and $Q(k_z)$, resulting in the inequality. $Q\left(k_z + \frac{2z_{MD}}{\sigma_z}\right)$ represents the very small probability that while the actual z_p is at the upper threshold, z_{MD} , the estimated \hat{z}_p is below the adjusted lower vertical threshold $-z_{MD} - k_z\sigma_z$, which is a sense-no-hazard condition. It is desirable to determine a k_z for the entire encounter. However, k_z is a function of σ_z , which decreases with time. For the purposes of determining k_z , it is assumed that σ_z values more than twice the vertical threshold ($2z_{MD}$) are too large to be useful for SAA alerting. Therefore to determine k_z , it is assumed that $\sigma_z = 2z_{MD}$. With the σ_z assumption, equation (3.16) is now reduced to:

$$P_{HMI} \leq Q(k_\tau) + Q(k_r) + Q(k_z) + Q(k_z + 1) \quad (3.18)$$

and equation (3.17) is now reduced to:

$$Q(k_\tau) + Q(k_r) + Q(k_z) + Q(k_z + 1) \leq I_{SS} \quad (3.19)$$

Equation (3.19) is used to determine coefficients (k_τ, k_r, k_z) that guarantee that P_{HMI} is less than I_{SS} . This could be done, for example, by evenly allocating coefficients $k_\tau = k_r = k_z$. Equations (3.18) and (3.19) give a conservative way to satisfy equation (3.8) while considering the three different hazard states.

This results in a tradeoff between safety and airspace capacity. Larger coefficients (k_τ, k_r, k_z) represent increased safety, but the resulting larger protected airspace around the own aircraft leads to reduced airspace capacity. Chapter 5 will further explore this safety versus airspace capacity tradeoff.

3.3 Integrity Risk Evaluation Summary

This chapter introduced the new idea of using integrity, the probability of

HMI, as an absolute safety metric for SAA systems. An integrity risk evaluation methodology was established, adjusting the DAA MOPS WCT by a multiple of the hazard state estimate error standard deviations. Then a computationally efficient upper bound on the integrity risk was developed to determine the integrity adjustment coefficients. The selection of coefficients results in a tradeoff between safety and airspace capacity further discussed in Chapter 5.

CHAPTER 4

CONTINUITY RISK

Another contribution of this thesis is development of a continuity risk evaluation methodology to quantify sense and avoid safety. Accepted aviation navigation certification standards quantify continuity, as well as integrity, as safety factors [39]. Like integrity, continuity is an absolute safety metric, which can be used to set certifiable requirements on individual system components, such as sense and avoid sensors [45, 71]. Continuity risk is typically quantified as the probability of false alert (FA) [25, 54, 62, 63, 65]. In a sense and avoid system, a false alert occurs when a hazard is sensed when no separation hazards exist. This chapter builds upon the SAA integrity risk evaluation methodology of the previous chapter to develop a methodology to quantify SAA continuity risk.

4.1 Continuity Based Solely on Modified Tau

A false alert occurs when no hazard exists, but a hazard is falsely sensed. Accounting for τ_{mod} only, no hazard exists when $\tau_{mod} > \tau_{SS}$. As discussed in the previous chapter, a hazard is sensed if the estimated hazard state is less than or equal to the adjusted threshold. In this case, a hazard is sensed if $\hat{\tau}_{mod} \leq \tau_{SS} + k_{\tau}\sigma_{\tau}$. As a result, the continuity risk, or probability of false alert, P_{FA} , is defined as:

$$P_{FA} = P(\hat{\tau}_{mod} \leq \tau_{SS} + k_{\tau}\sigma_{\tau} | \tau_{mod} > \tau_{SS}) \quad (4.1)$$

A false alert leads the own aircraft to maneuver when a self-separation maneuver is not warranted.

The left curve in Figure 4.1 depicts the normal distribution of the estimate, $\hat{\tau}_{mod}$, when actual τ_{mod} is just above the adjusted threshold $\tau_{SS} + k_{\tau}\sigma_{\tau}$, where the α in the figure is positive and very small. In this false alert case, actual τ_{mod} exceeds

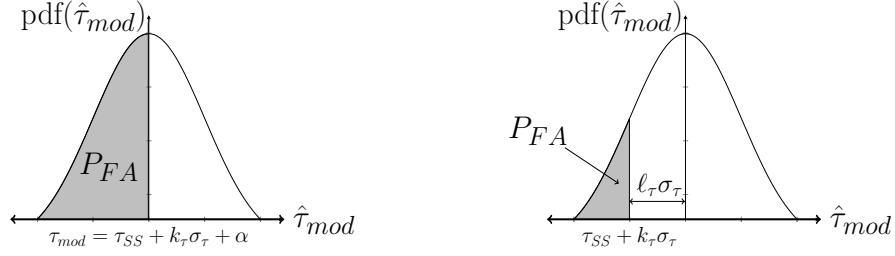


Figure 4.1. Continuity Risk and the Continuity Buffer

the adjusted threshold by very small α . At this point there is a 50% probability of $\hat{\tau}_{mod}$ being either above or below the mean, $\tau_{SS} + k_{\tau}\sigma_{\tau} + \alpha$. To ensure there is an acceptable FA probability, a continuity buffer is introduced by adding a multiple of the τ_{mod} standard deviation, $\ell_{\tau}\sigma_{\tau}$, to the adjusted threshold, $\tau_{SS} + k_{\tau}\sigma_{\tau}$. The continuity coefficient, ℓ_{τ} , is determined to ensure a predefined continuity risk requirement, C_{τ} , that will be specified by the certification authority's desired level of safety. In the right curve of Figure 4.1, the continuity buffer, $\ell_{\tau}\sigma_{\tau}$ is added to the adjusted threshold. In this case, if actual τ_{mod} is at or greater than $\tau_{SS} + (k_{\tau} + \ell_{\tau})\sigma_{\tau}$, then the self-separation continuity risk, or probability of false alert, P_{FA} , is assured to be lower than C_{τ} . Therefore, in order to ensure that P_{FA} is smaller than or equal to C_{τ} , ℓ_{τ} is defined as:

$$\ell_{\tau} = -\Phi^{-1}(C_{\tau}) \quad (4.2)$$

where $\Phi(x)$ is the CDF for the standard normal distribution in equation (3.4).

When τ_{mod} is between $\tau_{SS} + k_{\tau}\sigma_{\tau}$ and $\tau_{SS} + (k_{\tau} + \ell_{\tau})\sigma_{\tau}$, the own aircraft may FA with a probability higher than the continuity risk requirement. As such, the term τ_{mod} *protection level* is introduced and defined as $\tau_{SS} + (k_{\tau} + \ell_{\tau})\sigma_{\tau}$.

4.2 Continuity Risk for All Hazard States

As in the τ_{mod} only case, to ensure there is an acceptable P_{FA} for r_{CPA} and z_p ,

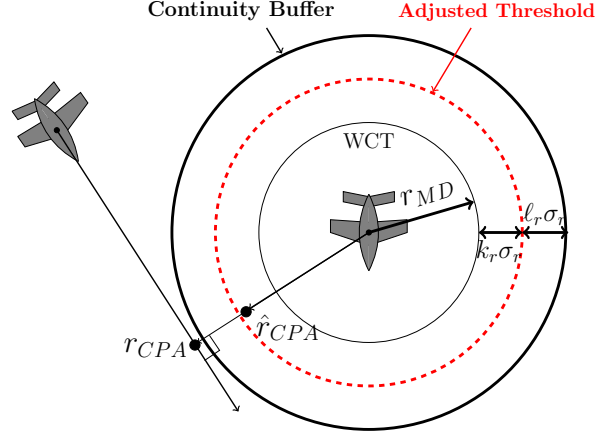


Figure 4.2. Worst Case FA Scenario for r_{CPA}

continuity buffers are added to the integrity-adjusted distance thresholds. The alert to maneuver will still be based on the integrity-adjusted distance thresholds. The area inside each continuity buffer is where false alerts can occur with a probability higher than a given continuity requirement. The self-separation continuity risk is P_{FA} :

$$\text{Sense Hazard} = [\hat{\tau}_{mod} \leq \tau_{SS} + k_{\tau}\sigma_{\tau} \cap \hat{r}_{CPA} \leq r_{MD} + k_r\sigma_r \cap |\hat{z}_p| \leq z_{MD} + k_z\sigma_z] \quad (4.3)$$

$$\text{No Hazard Exists} = [\tau_{mod} > \tau_{SS} \cup r_{CPA} > r_{MD} \cup |z_p| > z_{MD}] \quad (4.4)$$

$$P_{FA} = P(\text{Sense Hazard} | \text{No Hazard Exists}) \quad (4.5)$$

Figure 4.2 depicts a 2D FA scenario, where the actual r_{CPA} is just beyond the protection level ($r_{MD} + k_r\sigma_r + l_r\sigma_r$) while the estimate, \hat{r}_{CPA} , is just within the integrity-adjusted threshold ($r_{MD} + k_r\sigma_r$). The continuity buffer ensures this case occurs with a probability less than or equal to C_r (if C_r is allocated as a continuity requirement specifically for r_{CPA}).

P_{FA} must meet an overall predefined continuity requirement, C_{SS} . The conti-

nuity risk criterion is expressed as:

$$P_{FA} \leq C_{SS} \quad (4.6)$$

The following paragraphs describe a rigorous approach to establish an upper-bound on P_{FA} , and to allocate C_{SS} to each hazard state. The approach is also computationally efficient.

The hazard state estimates $\hat{\tau}_{mod}$, \hat{r}_{CPA} , and \hat{z}_p will be correlated in general. P_{FA} is a joint trivariate normal probability over the three hazard states:

$$P_{FA} = \frac{\int_{-z_{MD}-k_z\sigma_z}^{z_{MD}+k_z\sigma_z} \int_0^{r_{MD}+k_r\sigma_r} \int_0^{\tau_{SS}+k_\tau\sigma_\tau} e^{(-\frac{1}{2}[\psi'-\boldsymbol{\mu}]^T \mathbf{P}_{\tau r z}^{-1}[\psi'-\boldsymbol{\mu}])} d\tau' dr' dz'}{\sqrt{(2\pi)^3 |\mathbf{P}_{\tau r z}|}} \quad (4.7)$$

where $\boldsymbol{\psi}'$ is the vector of hazard state integration variables:

$$\boldsymbol{\psi}' = \begin{bmatrix} \tau' \\ r' \\ z' \end{bmatrix} \quad (4.8)$$

and $\boldsymbol{\mu}$ is the mean vector, which are now the protection levels:

$$\boldsymbol{\mu} = \begin{bmatrix} \tau_{SS} + k_\tau\sigma_\tau + \ell_\tau\sigma_\tau \\ r_{MD} + k_r\sigma_r + \ell_r\sigma_r \\ z_{MD} + k_z\sigma_z + \ell_z\sigma_z \end{bmatrix} \quad (4.9)$$

and $\mathbf{P}_{\tau r z}$ is the hazard state estimate error covariance matrix from equation (2.20).

As was done for integrity to determine the k coefficients, an easy-to-compute bound

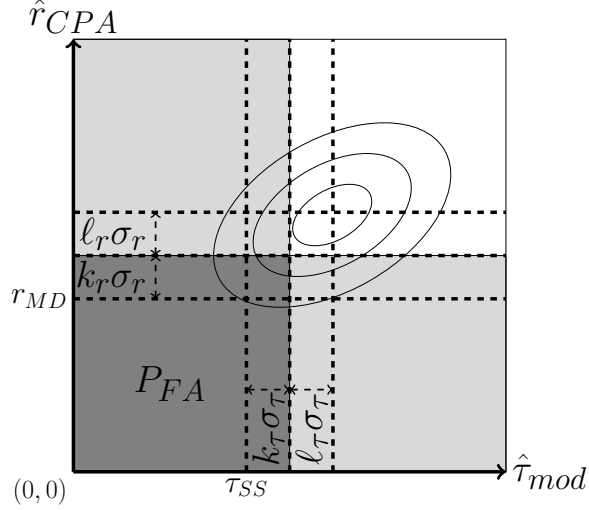


Figure 4.3. 2D Continuity Risk Correlation

on P_{FA} is used to determine ℓ coefficients, which will be explained in the following paragraphs.

For illustrative purposes, Figure 4.3, depicts the 2D FA probability ellipse between \hat{r}_{mod} and \hat{r}_{CPA} . The ellipse is centered at the protection levels $(\tau_{SS} + k_{\tau}\sigma_{\tau} + \ell_{\tau}\sigma_{\tau}, r_{MD} + k_r\sigma_r + \ell_r\sigma_r)$. P_{FA} is the dark shaded area of the lower left corner. The probability of being in the shaded areas to the left of the line $\hat{r} = \tau_{SS} + k_{\tau}\sigma_{\tau}$ is given by the Φ function, $\Phi(-\ell_{\tau})$. Likewise, the probability of being in the shaded areas below line $\hat{r}_{CPA} = r_{MD} + k_r\sigma_r$ is given by the Φ function, $\Phi(-\ell_r)$. The probability of the overlap between these two shaded areas cannot be evaluated analytically. Instead, an upper bound on P_{FA} is used, which is expressed as:

$$P_{FA} \leq \frac{\Phi(-\ell_{\tau}) + \Phi(-\ell_r)}{2} \quad (4.10)$$

The conservative upper bound in equation (4.10) accounts for the probability of being in the overlapping lower-left, shaded quadrant and the excess probabilities in the lighter shaded areas.

Extending this bounding to the full 3D case, the continuity risk is upper bounded by the following:

$$P_{FA} \leq \frac{\Phi(-\ell_\tau) + \Phi(-\ell_r) + \Phi(-\ell_z)}{3} \quad (4.11)$$

To ensure equation (4.6) is satisfied, this continuity risk upper bound must be less than or equal to the continuity risk requirement:

$$\frac{\Phi(-\ell_\tau) + \Phi(-\ell_r) + \Phi(-\ell_z)}{3} \leq C_{SS} \quad (4.12)$$

This continuity risk upper bound accounts for the overlaps and excesses between $\Phi(-\ell_\tau)$, $\Phi(-\ell_r)$, and $\Phi(-\ell_z)$. This bound also includes an excess in the extreme case, which would not be a false alert, where actual z_p is at the upper vertical continuity buffer, but the estimated \hat{z}_p is below the lower vertical continuity buffer, $-z_{MD} - k_z\sigma_z - \ell_z\sigma_z$.

Equation (4.12) is used to determine coefficients ($\ell_\tau, \ell_r, \ell_z$) that guarantee that the continuity risk is less than the continuity risk requirement. This could be done, for example, by evenly allocating C_{SS} to the three hazard states. Equations (4.11) and (4.12) give a conservative way to satisfy equation (4.6) while considering the three different hazard states. As discussed in the previous chapter for the integrity coefficients (k 's), the selection of continuity coefficients (ℓ 's) results in a tradeoff between safety and airspace capacity further discussed in Chapter 5.

4.3 Continuity Risk Evaluation Summary

This chapter introduced the new idea of using continuity, the probability of false alert, in conjunction with integrity, as absolute safety metrics for SAA systems. A continuity risk evaluation methodology was established, recognizing a continuity

buffer beyond the integrity-adjusted warning alert thresholds of the previous chapter. The continuity buffer is a multiple of each hazard state estimate error standard deviation. Then a computationally efficient upper bound on the continuity risk was developed to determine the continuity buffer coefficients. As in the previous chapter, the selection of coefficients results in a tradeoff between safety and airspace capacity further discussed in Chapter 5.

CHAPTER 5

OPERATIONAL LIMITS AND SENSOR REQUIREMENTS

The previous two chapters introduced new methods for evaluating integrity risk and continuity risk for sense and avoid by surrounding the well clear threshold with a protection level comprised of multiples of the hazard state estimate error standard deviations. This first part of this chapter will introduce the concept of an operational limit on the protection level to minimize the impact on surrounding airspace. The tradeoff on limiting the protection level is the need for better sensor performance. The last part of this chapter will outline how applying the integrity and continuity risk evaluation methodology with operational limits leads to certifiable requirements on sense and avoid sensors.

5.1 Operational Limits

In the previous two chapters, the integrity-adjusted threshold and the continuity buffer together formed a protection level that surrounds the well clear threshold. This protection level must be reasonably close to the original WCT before a hazard test can be executed. Otherwise, the resulting protected separation distances can be very large, leading to airspace capacity issues. To mitigate this, a certification authority will need to determine an acceptable fractional margin, ϵ , on all three original hazard thresholds (τ_{SS} , r_{MD} , and z_{MD}) to limit how big the protection level around the well clear threshold can get. This is expressed mathematically as:

$$\epsilon_{\tau} = \frac{(k_{\tau} + \ell_{\tau})\sigma_{\tau}}{\tau_{SS}} \quad (5.1)$$

$$\epsilon_r = \frac{(k_r + \ell_r)\sigma_r}{r_{MD}} \quad (5.2)$$

$$\epsilon_z = \frac{(k_z + \ell_z)\sigma_z}{z_{MD}} \quad (5.3)$$

Obviously, to limit the impact on the surrounding airspace, it is desirable that ϵ is small. However, smaller ϵ requires better sensor performance. Achieving $\epsilon = 0$ is impossible because it would require perfect sensors such that $\sigma_\tau = \sigma_r = \sigma_z = 0$. The fractional margin, ϵ , is used to define practical operational limits (denoted by a tilde) on hazard state estimate error standard deviations, $\tilde{\sigma}$. The hazard state estimate error standard deviation operational limits are:

$$\tilde{\sigma}_\tau \triangleq \frac{\epsilon \tau_{SS}}{k_\tau + \ell_\tau} \quad (5.4)$$

$$\tilde{\sigma}_r \triangleq \frac{\epsilon r_{MD}}{k_r + \ell_r} \quad (5.5)$$

$$\tilde{\sigma}_z \triangleq \frac{\epsilon z_{MD}}{k_z + \ell_z} \quad (5.6)$$

At the aircraft, the SAA hazard detection test described in equation (3.7) can be carried out with required integrity and continuity when σ_τ , σ_r , and σ_z all reach below their respective operational limits ($\tilde{\sigma}_\tau$, $\tilde{\sigma}_r$, and $\tilde{\sigma}_z$).

However, the intruder aircraft is approaching the own aircraft while the hazard state estimate error standard deviations are decreasing. Not all sensors or sensor-suites have the necessary performance to be ready to perform a hazard detection test before a maneuver is warranted. In other words, the hazard detection test must be performed with required integrity and continuity before a hazard actually occurs. To identify sensors that can meet this additional requirement, operational limits on hazard states are set as follows:

$$\begin{aligned} \tilde{\tau} &\triangleq (1 + \epsilon) \tau_{SS} \\ \tilde{r} &\triangleq (1 + \epsilon) r_{MD} \\ \tilde{z} &\triangleq (1 + \epsilon) z_{MD} \end{aligned} \quad (5.7)$$

Horizontal Range (r) vs Time to CPA

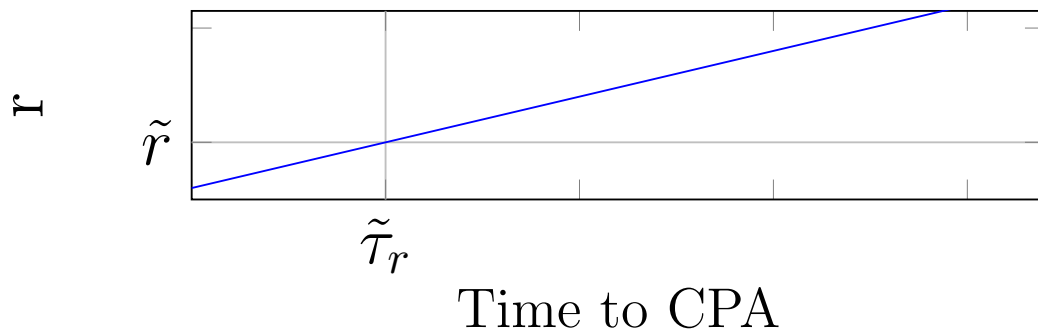


Figure 5.1. Horizontal Operational Limits

From this point on, a reference to τ without a subscript refers to true tau, the actual time to CPA. This methodology compares hazard state estimate error standard deviations to a precise actual time to CPA, true tau. Modified tau is an approximation that lacks this precision. Modified tau will retain its subscript and is still a hazard state.

The distance-based hazard state operational limits (\tilde{r} and \tilde{z}) can be translated to temporal operational limits on the actual time to closest point of approach (true tau) because there is an associated time when these distance limits are reached. Assuming intruder constant velocity, the corresponding times to closest point of approach can be determined when the horizontal range, r , and the vertical position, z , cross their respective operational limits (\tilde{r} , \tilde{z}). Figure 5.1 depicts an example of this for the intruder horizontal range, r , where the x-axis is actual time to closest point of approach. The horizontal temporal operational limit ($\tilde{\tau}_r$) is the time when the horizontal range crosses the horizontal range operational limit, \tilde{r} .

Because the detection test is simultaneously performed on all three hazard states, the operational limit on true tau for all three hazard states, labeled as $\tilde{\tau}$, can

be taken as the maximum of the three hazard state $\tilde{\tau}$'s:

$$\tilde{\tau} = \max(\tilde{\tau}_\tau, \tilde{\tau}_r, \tilde{\tau}_z) \quad (5.8)$$

For realistic well clear thresholds and aircraft velocities, $\tilde{\tau}_r$ and $\tilde{\tau}_z$ will typically be much lower than $\tilde{\tau}_\tau$. Therefore, $\tilde{\tau}$ will usually be determined by $\tilde{\tau}_\tau$. However, for very slow intruder-aircraft-to-own-aircraft closure rates, $\tilde{\tau}_r$ and $\tilde{\tau}_z$ may need to be considered.

5.2 Relating Operational Limits to Sensor Requirements

Figure 5.2 depicts an illustrative example of how the operational limit relates to sensor requirements for one hazard state estimate error standard deviation, in this case σ_τ . Within the plot are three curves representing three different sensors. The plot is the τ_{mod} hazard state estimate error standard deviation, σ_τ , versus the actual time to CPA, true tau. On the x-axis, time starts on the right at the time to closest point of approach at initial intruder detection, τ_0 , and decreases until it reaches the time at the CPA, where tau is zero ($\tau_{CPA} = 0$). Additional labels on the x-axis are the tau threshold, τ_{SS} , and the tau operational limit, $\tilde{\tau}$. For a sensor to meet τ_{mod} integrity and continuity requirements, the τ_{mod} standard deviation curve must cross the τ_{mod} standard deviation operational limit, $\tilde{\sigma}_\tau$, at an actual time to CPA, τ , greater than the time to CPA operational limit, $\tilde{\tau}$. If a sensor's hazard state estimate error standard deviation curve crosses its operational limit at a τ less than $\tilde{\tau}$, it will cross into the gray shaded area, which indicates a sensor that will false alert at a probability higher than the continuity risk requirement and a sensor that might produce hazardously misleading information at a rate higher than the integrity risk requirement. In Figure 5.2, Sensors 2 and 3 meet the τ_{mod} continuity risk and integrity risk requirements.

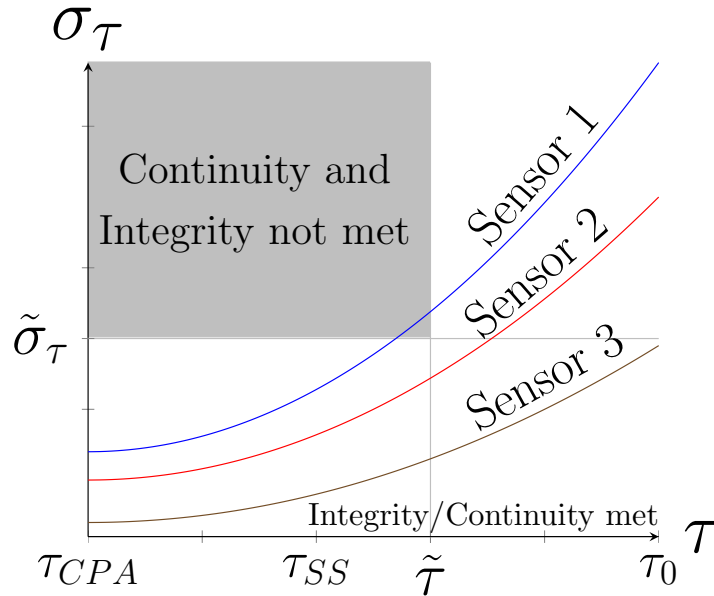


Figure 5.2. τ_{mod} Operational Limits and Sensor Requirements

Figure 5.3 extends this illustrative example to all three hazard states. Each hazard state has its own plot and within each plot there are three curves representing three different sensors. For a sensor to meet the full system integrity and continuity requirements, each hazard state estimate error standard deviation curve must cross its respective operational limit at a τ greater than $\tilde{\tau}$. If any of the sensor's σ curves cross its respective $\tilde{\sigma}$ at a τ less than $\tilde{\tau}$ (and penetrates the gray shaded area), that sensor will not meet continuity and integrity risk requirements. In the figure, only the bottom sensor, Sensor 3, meets the continuity risk and integrity risk requirements.

5.3 Applying Self-Separation Tests

To meet self-separation requirements, a sensor must have characteristics (measurement uncertainty, sensor range, and sample interval) to reduce each hazard state estimate error standard deviation below its operational limit $\tilde{\sigma}$ prior to its τ operational limit, $\tilde{\tau}$, as depicted for Sensor 3 in Figure 5.3. If a given sensor is not good enough, sensor uncertainty must be improved, sensor range must be extended, and/or

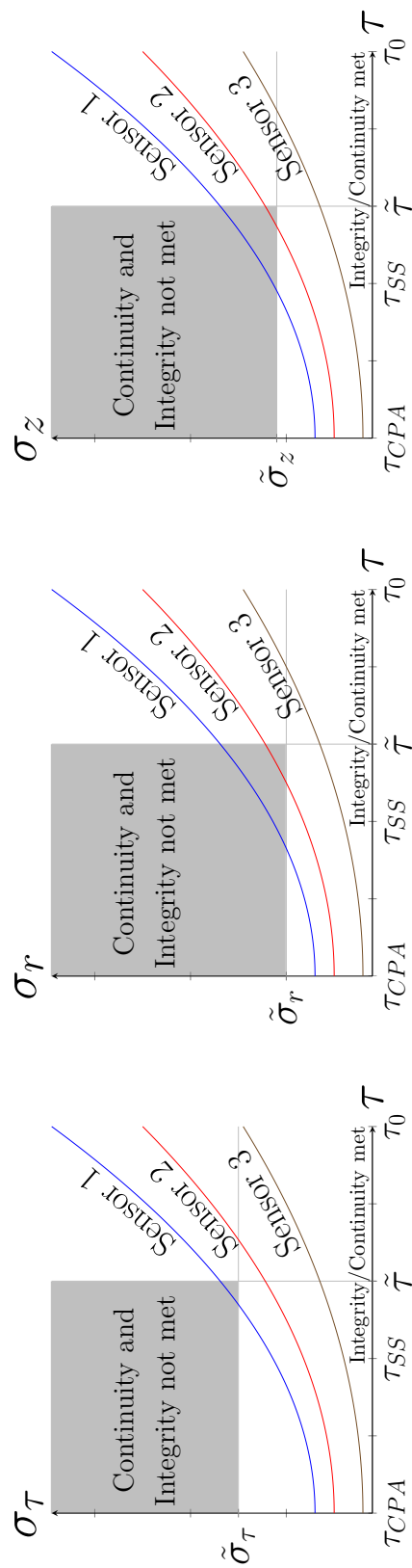


Figure 5.3. Applying All Operational Limits to Sensor Requirements

the intervals between independent samples must be reduced.

In order to maintain continuity, a minimal number of self-separation tests must be accomplished. For a constant velocity model, once all three hazard state estimate error standard deviations are reduced below their operational limits, $\tilde{\sigma}$'s, there only needs to be one test for a warning alert. From there, an alerted UAS can maneuver based on timing: when $\hat{\tau}_{mod} < \tilde{\tau}$.

5.4 Summary of Operational Limits and Sensor Requirements

This chapter introduced the concept of an operational limit on the protection level to minimize the impact on surrounding airspace. The tradeoff on limiting the protection level was the need for better sensor performance. A methodology was introduced to evaluate integrity and continuity risks with operational limits to determine certifiable requirements on SAA sensors.

CHAPTER 6

ANALYSIS OF 2D AND 3D ENCOUNTERS

The previous four chapters established a hazard state estimation process based on the DAA MOPS SAA hazard definition, developed an integrity risk evaluation methodology for SAA, developed a complementary continuity risk evaluation methodology for SAA, and related integrity and continuity risks to SAA sensor requirements. This chapter illustrates these contributions through simulated performance analyses. The first analysis looks at two dimensional, co-altitude encounters to explore how the entire SAA sensor characteristic trade space can impact integrity and continuity risk requirements. The second analysis expands the two dimensional work and focuses on three dimensional trajectories requiring a SAA sensor characteristic adjustment to meet integrity and continuity risk requirements.

6.1 Nominal Composite Sensor

The same nominal composite sensor is used for all analyses in this chapter. In the draft DAA MOPS, the input intruder measurements from an SAA radar includes relative slant range (ρ), relative range rate ($\dot{\rho}$), relative bearing (θ), and elevation angle (ϕ) [72]. The nominal sensor will be assumed to measure ρ , $\dot{\rho}$, θ , and ϕ . Chen, et al., described nominal characteristics for SAA sensors, reproduced in Table 6.1 [12]. This table includes cooperative and non-cooperative sensors. The cooperative sensors are the Traffic Collision Avoidance System (TCAS) and Automatic Dependent Surveillance-Broadcast (ADS-B). The non-cooperative sensors in this table are radar and electro-optical (EO). This research is concerned with non-cooperative sensors. The radar accuracy is defined in terms of range, range rate, azimuth angle and elevation angle. The electro-optical accuracy is defined in terms of azimuth and elevation angles. Chen does not define a range accuracy for electro-optical sensors explaining that “EO (monoscopic) does not inherently generate range information and the

detection range is typically poor” [12].

Table 6.1. SAA Sensor Characteristics [12]

	TCAS	ADS-B	Radar	Electro-optical
Accuracy	ρ : 175 - 300 ft	x, y : 25 - 250 ft z : 50 - 100 ft	θ : 0.5 - 2°	θ : 0.1 - 0.5° ϕ : 0.1 - 0.5°
	θ : 9 - 15 deg		ϕ : 0.5 - 2°	
	z : 50 - 100 ft		ρ : 10 - 200 ft $\dot{\rho}$: 1 - 10 $\frac{ft}{s}$	
Update rate	1 Hz	1 Hz	0.2 - 5 Hz	20 Hz
Detection range	≥ 14 NM	≥ 20 NM	5 - 10 NM	2 - 5 NM

Given the inputs from Table 6.1 for non-cooperative SAA sensor measurements, and assuming $2\text{-}\sigma$ accuracy, the composite nominal sensor will have the following characteristics: $\sigma_\rho = 5$ feet, $\sigma_\theta = 0.05^\circ$, $\sigma_\phi = 0.05^\circ$, and $\sigma_{\dot{\rho}} = 5$ ft/s. The sensor detection range, ρ_0 , is 8 nautical miles (NM), derived from [23, 24, 73] and is within the radar range from Table 6.1. The nominal sample rate, Δt , is 1 Hz, taken directly from the DAA MOPS [72, 73]. In aviation, distance is typically measured in nautical miles, airspeed is typically measured in knots (nautical miles per hour), and altitude is measured in feet. Given the aviation application of this research, these units will be used instead of the International System of Units (SI).

The well clear threshold used is based on the warning alert thresholds from the DAA MOPS: τ_{SS} of 35 seconds, r_{MD} of 4000 feet, and z_{MD} of 450 feet, and a lookahead time of 25 seconds [72]. All operational limit fractional margins are arbitrarily selected to be 10% ($\epsilon_\tau = \epsilon_r = \epsilon_z = 10\%$) leading to $\tilde{\tau} = 38.5$ seconds, $\tilde{r} = 4400$ feet, and $\tilde{z} = 495$ feet. The desired integrity requirement, $I_{SS} = 10^{-6}$, and the continuity requirement, $C_{SS} = 10^{-3}$, are based on the FAA’s definition of major and minor failure conditions [28].

6.2 Two Dimensional Analysis

Table 6.2. Nominal Sensor for Analyses

Characteristic	Value
Range Uncertainty, σ_ρ	5 feet
Azimuth Uncertainty, σ_θ	0.05°
Elevation Uncertainty, σ_ϕ	0.05°
Range Rate Uncertainty, $\sigma_{\dot{\rho}}$	5 ft/s
Detection Range, ρ_0	8 NM
Sample Rate, Δt	1 Hz
Fractional Margin, ϵ	10%
Integrity Requirement, I_{SS}	10^{-6}
Continuity Requirement, C_{SS}	10^{-3}

Based on the DAA MOPS, the maximum relative closure velocity is 370 knots for non-cooperative intruders [72]. Also, for simplicity, the integrity and continuity risk probability multipliers are set to be equal: $k_\tau = k_r = 4.89$ and $\ell_\tau = \ell_r = 3.09$. Applying these integrity and continuity coefficients to equations (5.4) - (5.8), the corresponding operational limits are $\tilde{\tau} = 38.5$ seconds, $\tilde{\sigma}_\tau = 0.44$ seconds, and $\tilde{\sigma}_r = 50.1$ feet. Based on the prior work from the initial iterations of this research, the most restrictive 2D intruder trajectories are either head-on to the intruder or tangent to the horizontal miss distance (r_{CPA}) circle [41, 43]. As a result, the 2D encounters in this analysis will use intruder head-on and tangent trajectories. These trajectories are depicted in Figure 6.1.

The intent of this 2D analysis is to explore the full sensor requirement trade space, investigating sensor performance sensitivities to adjustments of all possible sensor characteristic parameters. The most restrictive trajectory is identified in each case, to be used as the representative trajectory for that parameter at the end of the analysis, when all parameter adjustments are compared simultaneously.

6.2.1 Nominal Sensor Results. The results from the nominal case are in Fig-

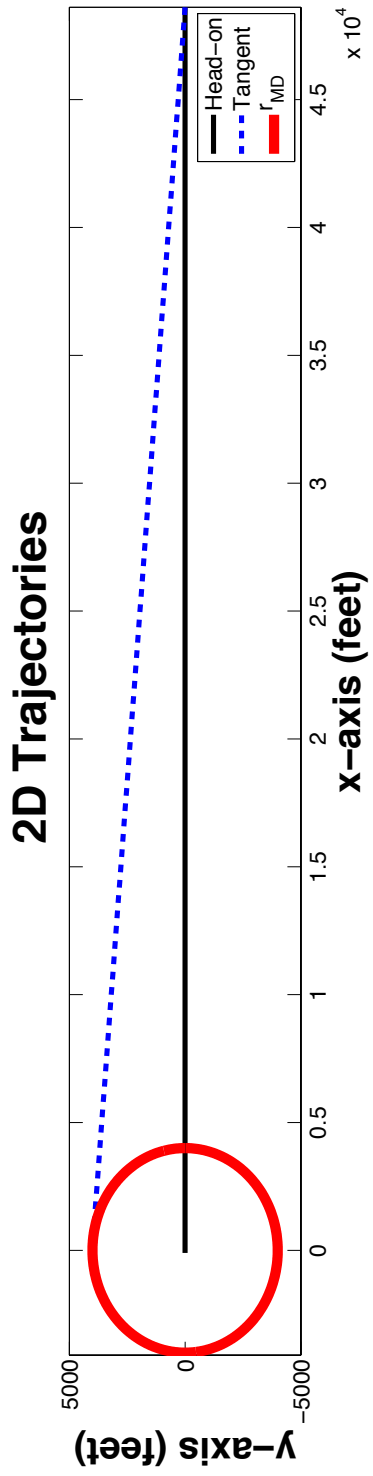


Figure 6.1. Two Dimensional Trajectories

ure 6.2. Following the methodology described in Section 5.2, integrity and continuity are met if the σ vs τ curves stay out of the upper left quadrant (the gray shaded region) of the figure. The horizontal cyan line is the $\tilde{\sigma}$ operational limit and the vertical magenta line is the $\tilde{\tau}$ operational limit.

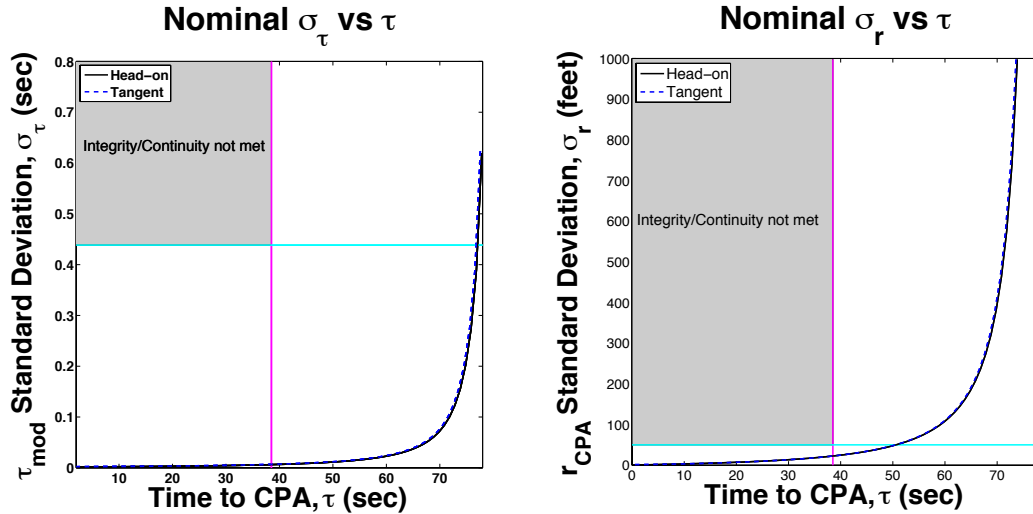


Figure 6.2. Results of a Nominal Sensor

For this nominal sensor, both trajectories meet both σ_{τ} and σ_r requirements for integrity and continuity. In the σ_{τ} curve, performance is similar for both trajectories and the curve falls below the $\tilde{\sigma}_{\tau}$ operational limit (cyan line) within the first few epochs. In the σ_r curve, performance is also similar for both trajectories and the curve falls below the $\tilde{\sigma}_r$ operational limit (cyan line) about 12 seconds prior to the $\tilde{\tau}$ operational limit (magenta line).

The difference in performance between each trajectory for both σ_{τ} and σ_r is small, as depicted in Figure 6.3. Here, the normalized hazard state standard deviation difference ($\Delta\sigma$) between the head-on and tangent trajectories are below 10% before both curves reach the $\tilde{\tau}$ magenta line from the right. It turns out that the tangent trajectory is slightly more restrictive than the others. Since this is the case, the

tangent trajectory will represent the nominal sensor for comparison with each of the following sensor adjustments until the final comparison of all sensor adjustments in section 6.2.5.

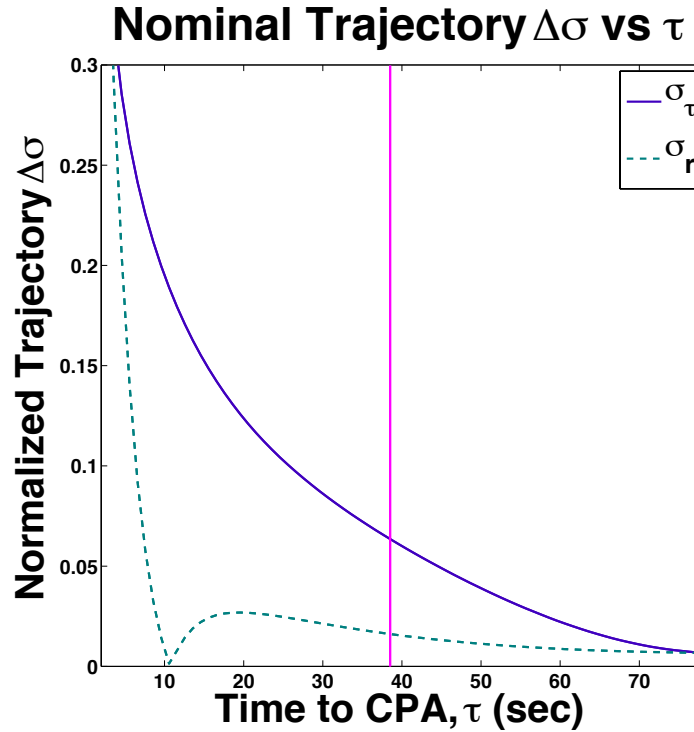


Figure 6.3. Nominal Normalized $\Delta\sigma$ Between Trajectories

The sensor characteristic trade space is explored in the following subsections, where adjustments are made one parameter at a time. Since the nominal sensor met requirements, the adjustments will loosen the sensor characteristics.

6.2.2 Sensor Slant Range Uncertainty Adjustment. The first adjustment is to relax sensor slant range uncertainty to $\sigma_\rho = 100$ feet, representing the loosest radar slant range accuracy in Table 6.1. The results in Figure 6.4 depict this ρ -adjusted sensor meeting both σ_τ and σ_r requirements. The adjustment does bring the σ_τ curve closer to the integrity and continuity requirement (the upper left quadrant), a sensitivity resulting from τ_{mod} being a function of horizontal range in equation (2.6).

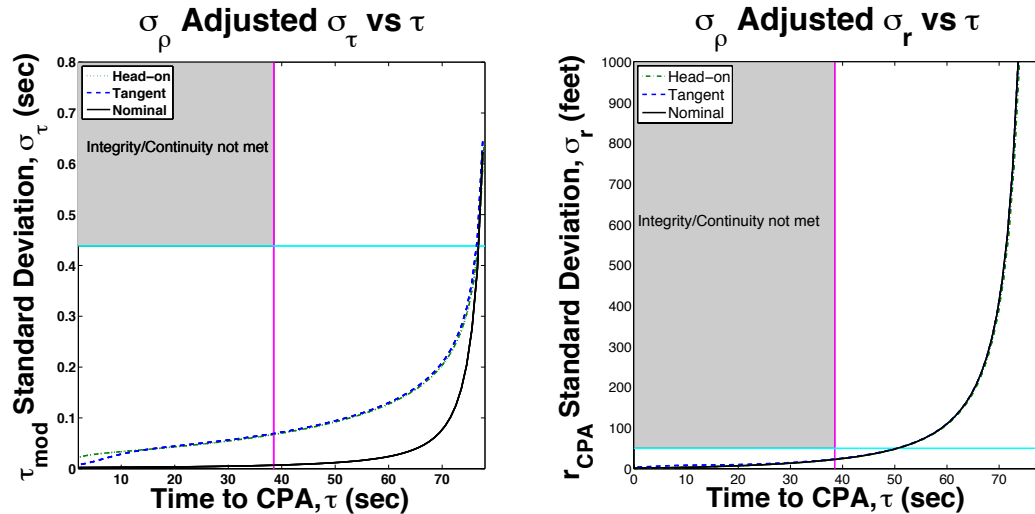


Figure 6.4. Results of a ρ -Adjusted Sensor: $\sigma_\rho = 100$ feet

However, the slant range adjustment has negligible impact on the σ_r curve.

Both head-on and tangent trajectories have similar performance for each σ curve. To determine which one is most restrictive, the ρ -adjusted sensor results are cataloged in Table 6.3 noting where the curves cross each $\tilde{\sigma}$ operational limit. In both cases the most restrictive trajectory is the tangent trajectory (with the lower τ at $\tilde{\sigma}$) and these trajectories will represent the slant range adjusted sensor in the final comparison.

Table 6.3. Results of a ρ -Adjusted Sensor

Trajectory	τ at $\tilde{\sigma}_\tau$	τ at $\tilde{\sigma}_r$
Nominal	76.8 s	50.5 s
Head-on	76.7 s	50.6 s
Tangent	76.4 s	50.3 s

6.2.3 Sensor Azimuth Uncertainty Adjustment. The next adjustment is to loosen sensor azimuth uncertainty to $\sigma_\theta = 0.1^\circ$. The sensor slant range uncertainty is returned to the nominal $\sigma_\rho = 5$ feet. The results in Figure 6.5 depict the θ -adjusted

sensor meeting both σ_τ and σ_r requirements. The adjustment has negligible impact

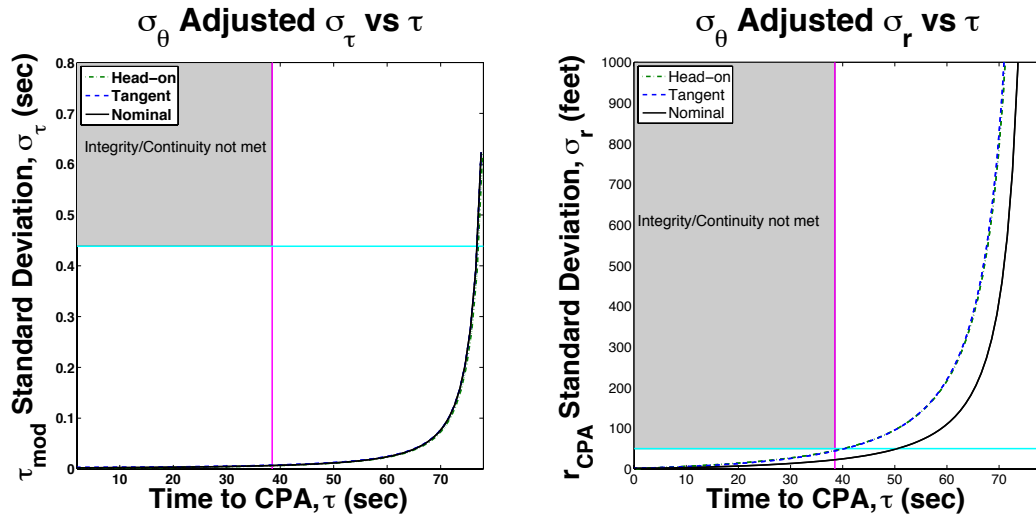


Figure 6.5. Results of a θ -Adjusted Sensor: $\sigma_\theta = 0.1^\circ$

on the σ_τ curve, but it brings the σ_r curve very close to the integrity and continuity limit. This σ_r sensitivity to azimuth results from small variations in azimuth leading to significant variations in r_{CPA} . As an example, the change in azimuth at the 8 NM detection range that would result in a 400 foot variation in r_{CPA} is less than a half degree:

$$\Delta\theta = \sin^{-1}\left(\frac{4400\text{ft}}{8\text{NM}}\right) - \sin^{-1}\left(\frac{4000\text{ft}}{8\text{NM}}\right) = 0.47^\circ \quad (6.1)$$

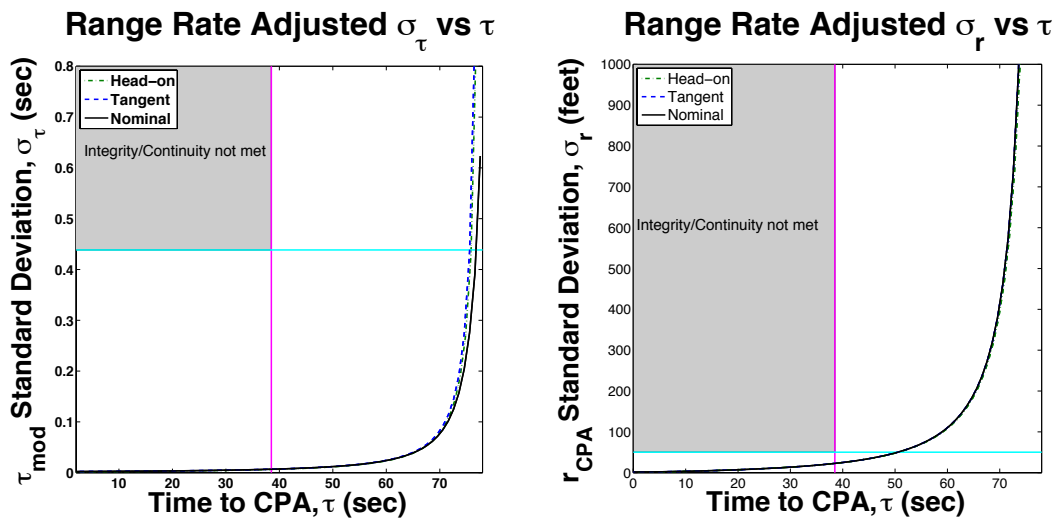
This represents an ϵ of 10%, where the difference from the edge of the 4400 foot protection level to the 4000 foot horizontal miss distance threshold is 400 feet.

Both head-on and tangent trajectories have similar performance for each σ curve. To determine which one is most restrictive, the azimuth-adjusted sensor results are cataloged in Table 6.4. For the σ_τ curve, the most restrictive trajectory is the tangent trajectory while for the σ_r curve, the head-on trajectory is most restrictive. These trajectories will represent the azimuth-adjusted sensor in the final comparison of all sensor adjustments in section 6.2.5.

Table 6.4. Results of a θ -Adjusted Sensor

Trajectory	τ at $\tilde{\sigma}_\tau$	τ at $\tilde{\sigma}_r$
Nominal	76.78 s	50.5 s
Head-on	77.05 s	40.1 s
Tangent	76.77 s	40.4 s

6.2.4 Sensor Range Rate Uncertainty Adjustment. The next adjustment is to relax sensor $\dot{\rho}$ uncertainty to $\sigma_{\dot{\rho}} = 100$ ft/s, representing a wide loosening. The sensor azimuth uncertainty is returned to the nominal $\sigma_\theta = 0.05^\circ$. The results in Figure 6.6 depict this $\dot{\rho}$ -adjusted sensor meeting both σ_τ and σ_r requirements. The adjustment

Figure 6.6. Results of a $\dot{\rho}$ -Adjusted Sensor: $\sigma_{\dot{\rho}} = 100$ ft/s

only has minimal impact on the first few epochs of the σ_τ curve, presumably since those epochs are estimating constant velocity. This adjustment has negligible impact on the σ_r curve. Both head-on and tangent trajectories have similar performance for each σ curve and the $\dot{\rho}$ -adjusted sensor results are cataloged in Table 6.5, where the tangent is the most restrictive trajectory for both curves.

6.2.5 All Sensor Adjustments. The analysis is repeated for sample rate and

Table 6.5. Results of a $\dot{\rho}$ -Adjusted Sensor

Trajectory	τ at $\tilde{\sigma}_\tau$	τ at $\tilde{\sigma}_r$
Nominal	76.8 s	50.499 s
Head-on	75.8 s	50.602 s
Tangent	75.6 s	50.498 s

detection range in Appendix E. The results of the nominal and all five parameter adjustments are compiled in Figure 6.7, where the most restrictive trajectories are applied.

All σ_τ curves reflect sensitivities to detection range and the slant range uncertainty (σ_ρ). All σ_r curves reflect sensitivities to detection range, azimuth uncertainty (σ_θ), and sample rate. This would suggest that to influence σ_τ , adjust detection range and slant range uncertainty and to influence σ_r , adjust detection range, azimuth uncertainty, and sample rate. Both curves are sensitive to detection range due to the reduction in the initial detection distance between the own aircraft and intruder as well as the reduction in corresponding time available for the SAA system to take measurements. The sensitivities associated with decreasing the sample rate can also be explained by reduction in the number of measurements available to inform the estimator. Sensitivities to azimuth and slant range uncertainties were explained in the preceding subsections.

A summary of the sensor parameter adjustments are in Table 6.6, where the values are the adjustments that put the curve right at the integrity and continuity limit (where the $\tilde{\sigma}$ and $\tilde{\tau}$ operational limits meet). The range rate uncertainty could not get to the integrity and continuity limit. Its performance only varied during the initial epochs, when the constant trajectory state velocity is initially estimated. The slant range uncertainty could be loosened to 1150 feet, which is much greater than the 200 foot accuracy in Table 6.1. The minimal impact of slant range uncertainty and

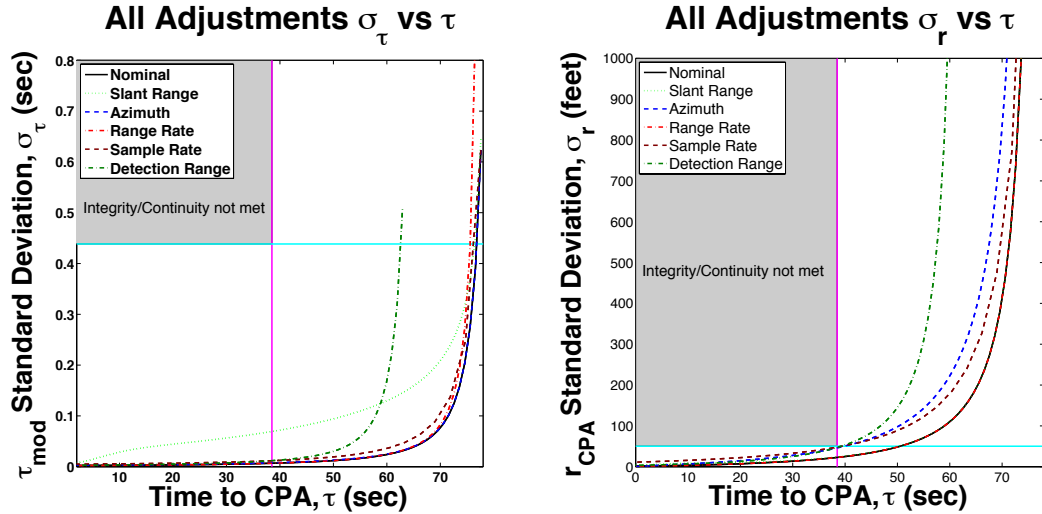


Figure 6.7. Results of All Sensor Parameter Adjustments

no impact of range rate uncertainty suggests the importance of azimuth uncertainty, explained in section 6.2.3, which can be loosened to 0.11° . The sample rate (which can be reduced to 0.32 Hz), as explained in the previous paragraph, produces sensitivities due to the reduction of measurements. Finally, the detection range (which can be reduced to 6.4 NM) produces sensitivities due to the reduction in measurements resulting from the shorter time between detection and when an alert is warranted. It is worth noting that all sensor adjustments in Table 6.6 were applied individually. Combining all of these adjustments simultaneously would lead to a sensor that is unable to meet integrity and continuity risk requirements.

Table 6.6. Summary of Sensor Adjustments

Sensor Characteristic	Adjustment at Integrity/Continuity Limit
Slant Range, σ_ρ	1150 feet
Azimuth, σ_θ	0.11°
Range Rate, $\sigma_{\dot{\rho}}$	N/A
Sample Rate, Δt	0.32 Hz
Detection Range, ρ_0	6.4 NM

6.2.6 Allocating Integrity and Continuity. Another sensitivity parameter is the allocation of integrity and continuity between hazard states. The nominal allocation is arbitrarily even across hazard states. However, in this example, σ_r is more restrictive than σ_τ . It is possible to maximize the risk allocation on r_{CPA} by reducing k_r and ℓ_r to increase $\tilde{\sigma}_r$. The trade-off is, following equations (3.15) and (4.10), a corresponding increase of k_τ and ℓ_τ and a decrease of $\tilde{\sigma}_\tau$ in equation (5.4). Following equations (3.15) and (4.10) again, there is a limit to how much risk can be allocated to r_{CPA} based on I_{SS} and C_{SS} . In this example case, the minimum k_r of 4.76 and ℓ_r of 2.88 leads to a maximum $\tilde{\sigma}_r$ of 52.36 feet. This leads to $k_\tau = 5.41$, $\ell_\tau = 3.70$ and $\tilde{\sigma}_\tau = 0.38$ seconds. In this case, the $\tilde{\sigma}_r$ increase of 52.36 feet does not provide significant improvement as compared to the nominal case of 50.1 feet.

6.2.7 Increasing Fractional Margin, ϵ . Another option to meet integrity and continuity, if acceptable to the certification authority, is increasing ϵ , which relaxes the operational limits ($\tilde{\tau}$'s and $\tilde{\sigma}$'s). As an illustrative example, increasing ϵ to 25% increases $\tilde{\sigma}_\tau$ to 1.10 seconds, increases $\tilde{\sigma}_r$ to 125.3 feet, and increases $\tilde{\tau}$ to approximately 43.75 seconds. The problem with increasing ϵ is that it increases the protection levels. This, in turn, reduces airspace capacity to the extent that air traffic control now has to account for the amount of protected airspace around the own aircraft. For example, the increase in fractional margin to 25%, increases the horizontal protection level by 600 feet (from 4400 feet to 5000 feet).

6.2.8 Summary of 2D Analysis. Every parameter of the sensor requirement trade space was examined. The nominal sensor met UAS SAA integrity and continuity risk requirements, so the trade space of sensor performance characteristics was loosened to determine impacts of sensor adjustments on integrity and continuity risks. This analysis suggests that detection range and σ_ρ have the most influence on σ_τ and detection range, σ_θ , and sample rate have the most influence on σ_r . Adjustments to

the fractional margin, ϵ , and reallocating integrity and continuity unevenly between the hazard states can also be applied to help meet requirements.

6.3 Three Dimensional Analysis

This section will expand the two dimensional analysis in the previous section. The intent of the 2D analysis was to explore the entire sensor characteristic trade space. The intent of the 3D analysis is to now apply sensor characteristic improvements not only in 3D, but to adjust a sensor that cannot meet integrity and continuity requirements to get acceptable performance. The 3D analysis focuses on seven trajectories, which were originally analyzed in [40] for previous iterations of the hazard states and WCT. These seven trajectories are:

- Head-on, direct collision course descending.
- Head-on, level at z_{MD} .
- Tangent to the r_{MD} circle, level at z_{MD} .
- Head-on, descending, intercepting the top WCT border at the back.
- Tangent to the r_{MD} circle, descending, intercepting the top WCT border.
- Head-on, descending, intercepting the bottom WCT border at the front.
- Tangent to the r_{MD} circle, descending, intercepting the bottom WCT border.

A side view of the head-on trajectories are depicted in the left side of Figure 6.8 and a top down view of the head-on and tangent trajectories are depicted on the right side of Figure 6.8.

These trajectories were selected based on the worst case trajectories in 2D (from the previous section) being head-on and tangent and the vertical profiles were

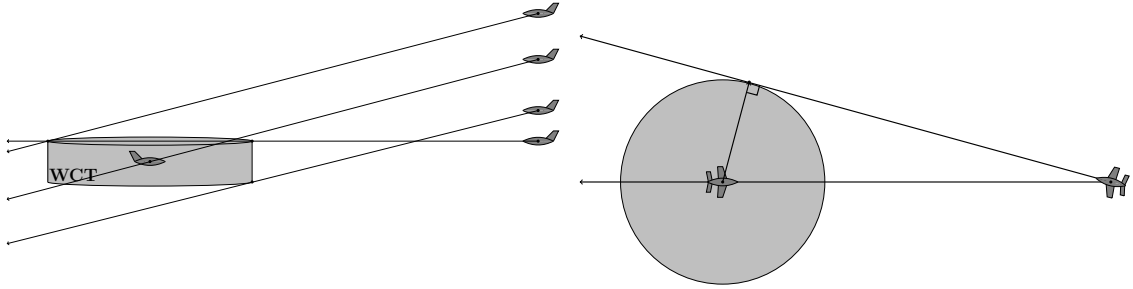


Figure 6.8. Three Dimensional Trajectories

based on level and descending border cases around the WCT cylinder. Based on the DAA MOPS, the maximum relative descent rate is 5000 feet per minute (fpm) and the maximum relative closure velocity is still limited to 370 knots for non-cooperative intruders [72]. Also, for simplicity, the integrity and continuity risk coefficients are set to be equal: $k_\tau = k_r = k_z = 4.98$ and $\ell_\tau = \ell_r = \ell_z = 3.09$. From these integrity and continuity multipliers, the corresponding operational limits are $\tilde{\tau} = 38.5$ seconds, $\tilde{\sigma}_\tau = 0.43$ seconds, $\tilde{\sigma}_r = 49.57$ feet, and $\tilde{\sigma}_z = 5.58$ feet.

6.3.1 Nominal Sensor Results. The results from the nominal case are in Figure 6.9. In these plots, the curve for the most restrictive trajectory is illustrated. Integrity and continuity are met if each σ vs τ curve stays out of the gray shaded, upper left quadrant of the plots. The cyan horizontal line is the $\tilde{\sigma}$ operational limit and the vertical magenta line is the $\tilde{\tau}$ operational limit. Note that time goes from right (representing the initial tau at the detection range, τ_0) to left (representing the final tau at the CPA, $\tau_{CPA} = 0$).

For this nominal sensor, all trajectories meet both σ_τ and σ_r requirements for integrity and continuity, but none of the trajectories meet requirements for σ_z . In the σ_τ curve, performance is similar for all trajectories and the curve falls below the $\tilde{\sigma}_\tau$ operational limit (cyan line) within the first few time-epochs. In the σ_r curve, performance is also similar for all trajectories and the curve falls below the $\tilde{\sigma}_r$ operational

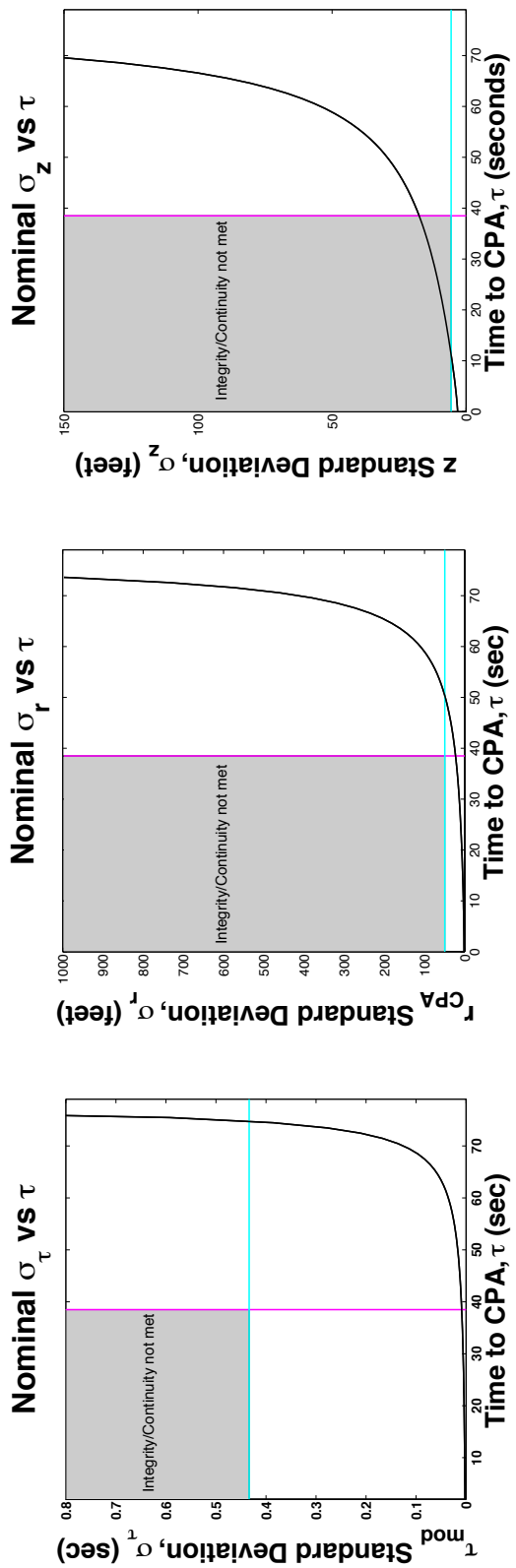


Figure 6.9. 3D Results of a Nominal Sensor

limit (cyan line) about 12 seconds prior to the $\tilde{\tau}$ operational limit (magenta line). In the σ_z curve, performance is also similar for all trajectories, but the curve falls below the $\tilde{\sigma}_z$ cyan line well to the left of the $\tilde{\tau}$ operational limit (magenta line), suggesting a sensor with better performance is required.

One of the issues with σ_z is that the fractional margin, ϵ has a larger impact on adjusting z_{MD} . A 10% inflation on a 450 ft vertical miss distance is a mere 45 feet, as compared to the 400 foot inflation on the 4000 foot horizontal miss distance and the 3.5 second inflation (representing over 2000 feet at 370 knots) of the 35 second tau threshold. All of the σ_z curves for the nominal trajectory reach $\tilde{\tau}$, the vertical magenta line, below 18 feet. Therefore increasing ϵ from 10% to 33% will move $\tilde{\sigma}_z$ (the horizontal cyan line on the σ_z curve) from 5.6 feet to 18.4 feet. This also inflates the z_{MD} threshold from 450 feet to a protection level of 600 feet. Since the RTCA SC-228 Science and Research Panel WCT recommendation had a vertical miss distance of 700 feet [14], a 600 foot vertical protection level is reasonable.

As in the 2D case, performance for all trajectories were similar. The difference in performance between each trajectory for σ_r , σ_r , and σ_z is small, as depicted in Figure 6.10. Here, the normalized hazard state estimate error standard deviation differences between the seven trajectories are below 30% before all three curves reach the $\tilde{\tau}$ magenta line from the right. That normalized $\Delta\sigma$ is less than 10% for the horizontal and vertical $\Delta\sigma$'s. For the σ_r curve, the tangent descending trajectory that crosses the well clear threshold cylinder at the top is slightly more restrictive than the others. For the σ_r and σ_z curves, the tangent level trajectory at the top of the well clear threshold cylinder is slightly more restrictive. As a result, these are the trajectories represented in Figure 6.9 and these trajectories will represent the nominal sensor for comparison purposes in the next subsection.

6.3.2 Adjusted Sensor Results. Since the nominal sensor did not meet σ_z

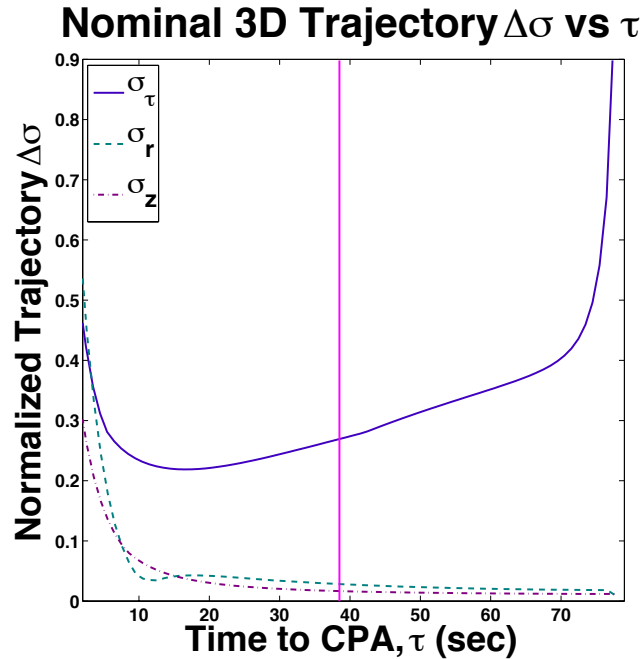


Figure 6.10. Nominal Normalized $\Delta\sigma$ Between 3D Trajectories

requirements, an adjustment is made to the sensor elevation uncertainty. Sensor ϕ uncertainty is improved to $\sigma_\phi = 0.01^\circ$, representing the improvement that now meets integrity and continuity requirements. The results in Figure 6.11 depict this ϕ -adjusted sensor meeting all requirements. The adjustment had minimal impact on the σ_τ curve, negligible impact on the σ_r curve, but it brings the σ_z curve within the integrity and continuity limits. The σ_z sensitivity to σ_ϕ is due to small variations in elevation resulting in large changes in vertical distance. As an example of the sensitivity of vertical distance to small variations of elevation, for a level trajectory at the top z_{MD} and at the 8 NM detection range, the change in elevation that would result in a 45 foot variation above the z_{MD} threshold (representing an ϵ of 10%) is less than a tenth of a degree:

$$\Delta\phi = \tan^{-1}\left(\frac{495\text{ft}}{8\text{NM}}\right) - \tan^{-1}\left(\frac{450\text{ft}}{8\text{NM}}\right) = 0.053^\circ \quad (6.2)$$

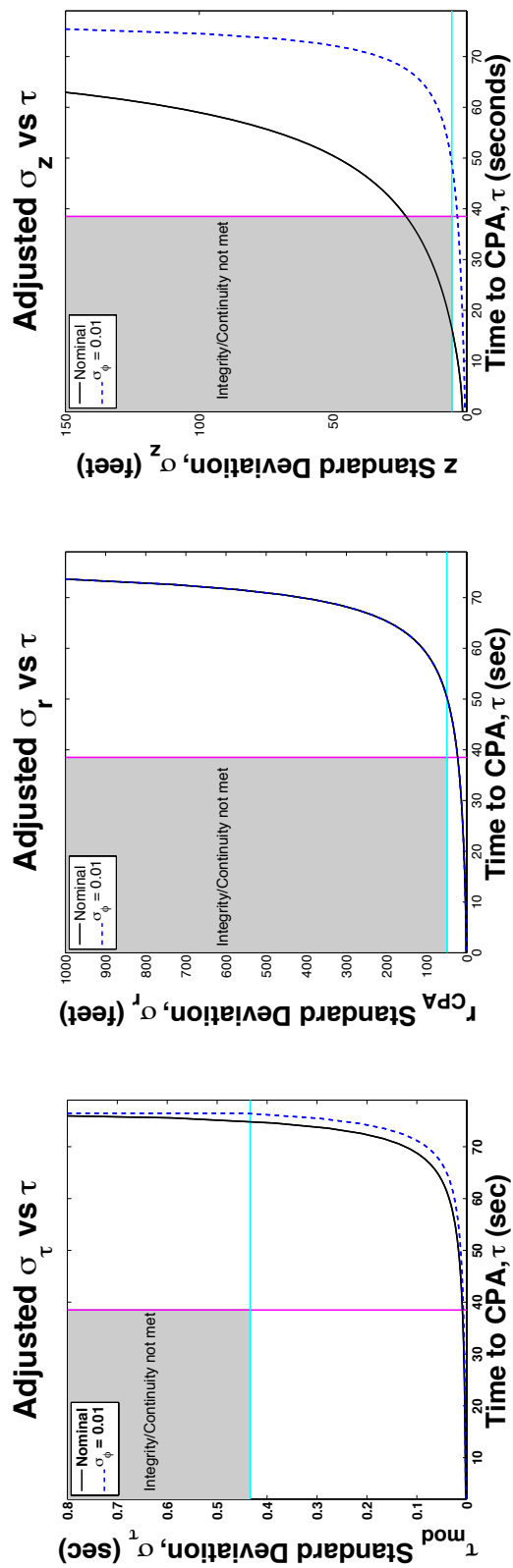


Figure 6.11. 3D Results of a ϕ -Adjusted Sensor: $\sigma_\phi = 0.01^\circ$

All trajectories had similar performance. For completeness, the ϕ -adjusted sensor results are cataloged in Table 6.7 noting where the curves cross each $\tilde{\sigma}$ operational limit. For the σ_r and σ_r curves, the most restrictive trajectories did not change (still tangent-descending-top and tangent-level-top respectively). However, for the σ_z curve, the tangent-descending-top trajectory is now most restrictive.

Table 6.7. Results of a ϕ -Adjusted Sensor

Trajectory	τ at $\tilde{\sigma}_r$	τ at $\tilde{\sigma}_r$	τ at $\tilde{\sigma}_z$
Nominal	74.8 s	50.34 s	11.16 s
Head-on Direct	76.8 s	50.58 s	49.29 s
Head-on Level Top	76.8 s	50.45 s	49.21 s
Head-on Descending Top	76.5 s	50.45 s	49.08 s
Head-on Descending Bottom	77.0 s	50.68 s	49.46 s
Tangent Level Top	76.6 s	50.34 s	48.91 s
Tangent Descending Top	76.4 s	50.41 s	48.89 s
Tangent Descending Bottom	76.7 s	50.52 s	49.07 s

6.3.3 Summary of 3D Analysis. For this 3D example, the nominal sensor did not meet UAS SAA integrity and continuity risk requirements for the vertical separation hazard. This can be attributed to the nature of the ϵ 's increased influence over the vertical hazard state, as compared to the other hazard states. An ϵ increase from 10% to 33% puts the nominal sensor within integrity and continuity requirements. Without this ϵ boost, a sensor elevation uncertainty adjustment was made to bring the performance within integrity and continuity risk limits. This analysis suggests that ϵ and σ_ϕ have significant influence on σ_z due to the smaller (in relation to horizontal and tau) vertical miss distance threshold and the large impact that small variations in elevation have on vertical position.

6.4 Summary of 2D and 3D Sensitivity Analyses

The analyses in this chapter depicted 2D co-altitude encounters and 3D de-

scending and level encounters. The nominal sensor did not require adjustment in the 2D scenario and the entire sensor characteristic trade space was explored, one parameter at a time. Certain hazard states had more sensitivity to certain sensor parameters than others. This 2D analysis was then expanded to 3D, where the nominal sensor did not meet integrity and continuity requirements for the vertical hazard state. An improvement in sensor elevation uncertainty or a relaxing of ϵ was required to meet integrity and continuity requirements. This was an example of how the integrity and continuity risk evaluation methodology could be used to set SAA sensor requirements.

CHAPTER 7

INTRUDER LINEAR ACCELERATIONS

The trajectory state estimation model used to build the integrity and continuity risk methodology is based on a constant velocity assumption outlined in the DAA MOPS [72]. In this chapter, to provide more accurate intruder trajectory estimations, constant velocity is no longer assumed and an estimation model is introduced that can account for constant intruder linear accelerations. An analysis will explore the sensor trade space.

In addition, the performance of a true tau updated with accelerations, is compared to modified tau. According to the TCAS II MOPS, the distance modifier in τ_{mod} is a “safety factor incorporated in range measurements to account for possible accelerations by the intruder” [70]. The true tau and modified tau performance comparison will lead to a recommendation on which tau should be used as a hazard state for linear accelerations.

7.1 Constant Acceleration Kalman Filter

The trajectory state estimation model used to build the integrity and continuity risk methodology is based on a constant velocity assumption outlined in the DAA MOPS [72]. To refine this effort for constant accelerations, the trajectory state vector, \mathbf{x}_n , now includes time variant intruder position and velocity, as well as constant acceleration:

$$\mathbf{x}_n = \begin{bmatrix} x_n & y_n & z_n & \dot{x}_n & \dot{y}_n & \dot{z}_n & \ddot{x} & \ddot{y} & \ddot{z} \end{bmatrix}^T \quad (7.1)$$

The discrete-time process-noise-free state-transition equation in the form of

equation (A.22) is used. However, the constant state-transition matrix \mathbf{F} is now:

$$\mathbf{F} = \begin{bmatrix} \mathbf{I}_{3 \times 3} & \Delta t \mathbf{I}_{3 \times 3} & \frac{\Delta t^2}{2} \mathbf{I}_{3 \times 3} \\ \mathbf{0}_{3 \times 3} & \mathbf{I}_{3 \times 3} & \Delta t \mathbf{I}_{3 \times 3} \\ \mathbf{0}_{3 \times 3} & \mathbf{0}_{3 \times 3} & \mathbf{I}_{3 \times 3} \end{bmatrix} \quad (7.2)$$

The measurement equation, in the form of equation (A.25) is used, with the exception of the linearized observation matrix, \mathbf{H}_n . This observation matrix, \mathbf{H}_n , is now 4×9 to account for the acceleration trajectory states in equation (7.1).

The Kalman filter initial conditions are modified. Now, the distribution of the error associated with the initial estimation, $\hat{\mathbf{x}}_0$, is:

$$\mathbf{x}_0 - \hat{\mathbf{x}}_0 \sim N \left(\left[\begin{array}{c} \mathbf{0}_{6 \times 1} \\ \mathbf{0}_{3 \times 1} \end{array} \right], \left[\begin{array}{c|c} \bar{\mathbf{P}}_0 & \mathbf{0}_{6 \times 3} \\ \hline \mathbf{0}_{3 \times 6} & \boldsymbol{\Sigma}_a \end{array} \right] \right) \quad (7.3)$$

where $\bar{\mathbf{P}}_0$ is the initial position and velocity estimate error covariance (no prior knowledge is assumed on these states), and $\boldsymbol{\Sigma}_a$ is based on an expected distribution of pilot action. For example, a maximum $3\text{-}\sigma$ intruder acceleration of 1 knot/s can be derived from the intruder aircraft behavior distribution of the MIT Lincoln Lab Uncorrelated Encounter Model for the NAS [50, 72].

This research only looks at changes in the magnitude of the velocity vector, which is assumed aligned with the direction of intruder aircraft velocity. The standard deviation of the specific force of the pilot action is noted σ_a and is in the head-on direction of the intruder body frame. This is converted into the own aircraft frame

using the following equation:

$$\Sigma_a = \mathbf{B} \begin{bmatrix} \sigma_a^2 & 0 & 0 \\ 0 & 0 & 0 \\ 0 & 0 & 0 \end{bmatrix} \mathbf{B}^T \quad (7.4)$$

where \mathbf{B} is the transformation matrix from the intruder body frame to the own body frame.

The Kalman filter (equations (A.27) - (A.31)) is used to estimate trajectory states and their estimate error covariance matrix, $\hat{\mathbf{P}}_n$, at each epoch n .

7.2 Hazard States for Linear Accelerations

Removing the constant velocity assumption adds another level of complexity to the SAA problem. Because the acceleration is linear, the trajectory geometry does not change relative to the constant velocity case, and the geometric horizontal CPA in equation (2.13) is still valid. However, the modified tau in equation (2.7) and the predicted vertical separation in equation (2.15), must be refined. This thesis proposes an adjusted true tau and an adjusted predicted vertical separation to refine or replace the constant velocity versions of τ_{mod} and z_p .

7.2.1 True Tau Adjusted for Accelerations. The expressions for x_{CPA} and y_{CPA} are as follows:

$$x_{CPA} = x + \dot{x}\tau + \frac{1}{2}\ddot{x}\tau^2 \quad (7.5)$$

$$y_{CPA} = y + \dot{y}\tau + \frac{1}{2}\ddot{y}\tau^2 \quad (7.6)$$

Because the direction of the velocity does not change and remains perpendicular to

\mathbf{r}_{CPA} , the vector from the own aircraft to the CPA, the following dot product holds:

$$\mathbf{r}_{CPA} \cdot \dot{\mathbf{x}} = x_{CPA}\dot{x} + y_{CPA}\dot{y} = 0 \quad (7.7)$$

This results in the following quadratic:

$$\dot{x}(x + \dot{x}\tau + \frac{1}{2}\ddot{x}\tau^2) + \dot{y}(y + \dot{y}\tau + \frac{1}{2}\ddot{y}\tau^2) = 0 \quad (7.8)$$

Written another way:

$$\left(\frac{\dot{x}\ddot{x} + \dot{y}\ddot{y}}{2}\right)\tau^2 + (\dot{x}^2 + \dot{y}^2)\tau + (x\dot{x} + y\dot{y}) = 0 \quad (7.9)$$

Solving for τ , the new true tau becomes:

$$\tau_{true} = \frac{-(\dot{x}^2 + \dot{y}^2) + \sqrt{(\dot{x}^2 + \dot{y}^2)^2 - 2(\dot{x}\ddot{x} + \dot{y}\ddot{y})(x\dot{x} + y\dot{y})}}{\dot{x}\ddot{x} + \dot{y}\ddot{y}} \quad (7.10)$$

7.2.2 Predicted Vertical Separation Adjusted for Accelerations. The predicted vertical separation equation (2.15) now needs to be adjusted for constant accelerations resulting in the following equation:

$$z_p = z_n + p\Delta t\dot{z} + \frac{(p\Delta t)^2}{2}\ddot{z} \quad (7.11)$$

where p are the all the future epochs up to the 25 second lookahead time.

7.3 Intruder Linear Acceleration Sensitivity Analysis

This sensitivity analysis assumes constant straight line relative intruder accelerations, reflecting potential intruder pilot thrust inputs. The composite nominal sensor of Chapter 6 is applied: σ_ρ is 5 feet, σ_θ is 0.05° , σ_ϕ is 0.05° , $\sigma_{\dot{\rho}}$ is 5 ft/s, and detection range is 8 NM. The DAA MOPS well clear threshold is also used: τ_{SS}

of 35 seconds, r_{MD} of 4000 feet, and z_{MD} of 450 feet, and a lookahead time of 25 seconds [72]. All operational limit fractional margins are 10% ($\epsilon_\tau = \epsilon_r = \epsilon_z = 10\%$) leading to $\tilde{\tau} = 38.5$ seconds, $\tilde{r} = 4400$ feet, and $\tilde{z} = 495$ feet. The desired integrity requirement, $I_{SS} = 10^{-6}$, and the continuity requirement, $C_{SS} = 10^{-3}$, are based on the FAA's definition of major and minor failure conditions [28]. For simplicity, the integrity and continuity risk coefficients are set to be equal: $k_\tau = k_r = k_z = 4.98$ and $\ell_\tau = \ell_r = \ell_z = 3.09$.

Based on the DAA MOPS, the nominal update rate is selected to be 1 Hz, the worst-case relative closure velocity is limited to 370 knots for non-cooperative intruders, and the worst case relative vertical velocity for non-cooperative intruders is 5000 feet per minute [72]. The predicted standard deviation on intruder acceleration, σ_a , is selected to be 0.33 knots/sec, based on a maximum 3- σ intruder acceleration of 1 knot/s taken from the intruder aircraft behavior distribution of the MIT Lincoln Lab Uncorrelated Encounter Model for the NAS [50, 72]. Each trajectory with this $\sigma_a = 0.33$ knots/sec will be compared to the case with assumed perfect knowledge of the intruder pilot acceleration, where $\sigma_a = 0$.

For the trajectories, there are the same seven trajectories from the previous chapter: tangent even at the top z_{MD} threshold, tangent descending at the top z_{MD} threshold, tangent descending at the bottom $-z_{MD}$ threshold, head-on even at the top z_{MD} threshold, head-on descending at the top z_{MD} threshold, head-on descending at the bottom $-z_{MD}$ threshold, and head-on direct collision course. There were three cases for each trajectories: one starting at the maximum 370 knots and decelerating at 1 knot/s until the CPA, one accelerating at 1 knot/s until reaching the maximum 370 knots at the CPA, and one constant velocity at the maximum 370 knots.

7.3.1 Results. The results of the nominal sensor is in Figure 7.1. As in the constant velocity case of the previous chapter, the nominal sensor meets τ (in this section, τ

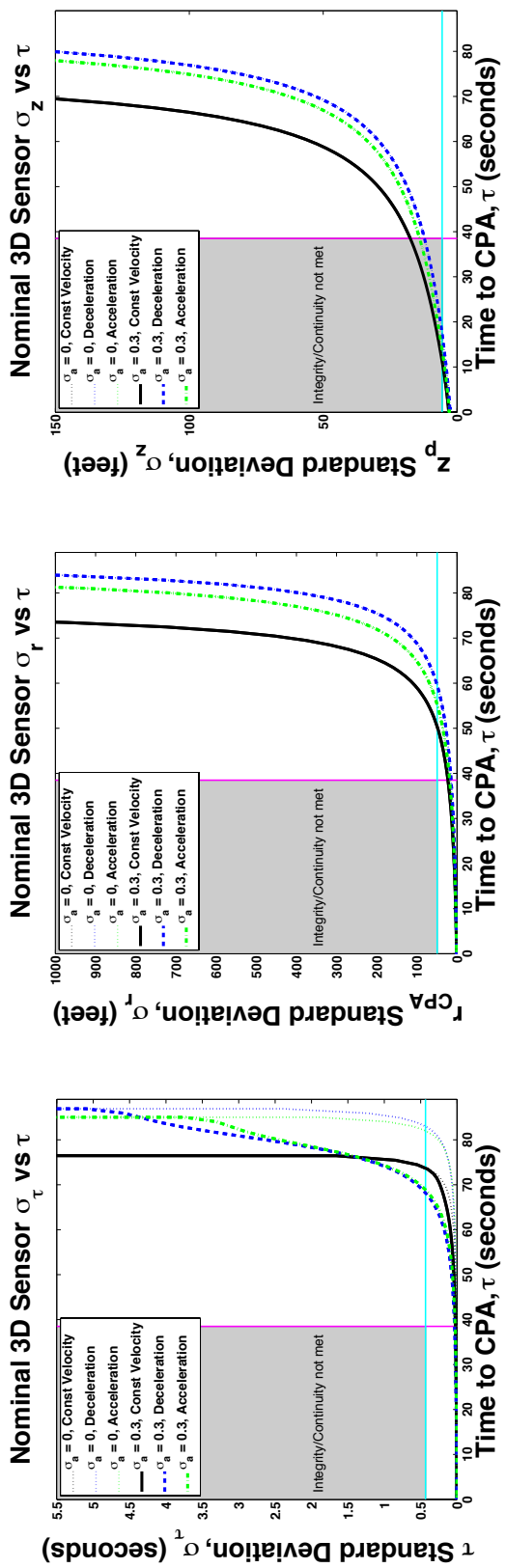


Figure 7.1. Results of a Nominal Sensor

without a subscript is the true tau from equation (7.10)) and r_{CPA} requirements for all trajectories and accelerations. Also, in a similar manner to the constant velocity case, the nominal sensor does not meet predicted vertical separation requirements. The only difference of note is that the accelerated trajectories result in longer times (and more measurements) within the sensor range than the constant velocity case, because the latter is always at maximum velocity. As for the impact of accounting for an unknown intruder thrust action, it is minimal with respect to σ_r , mostly because r_{CPA} is a function of position and velocity only, and is minimal with respect to σ_z , because the linear acceleration results in a maximum vertical acceleration of only $\ddot{z} = 0.23 \frac{ft}{s^2}$.

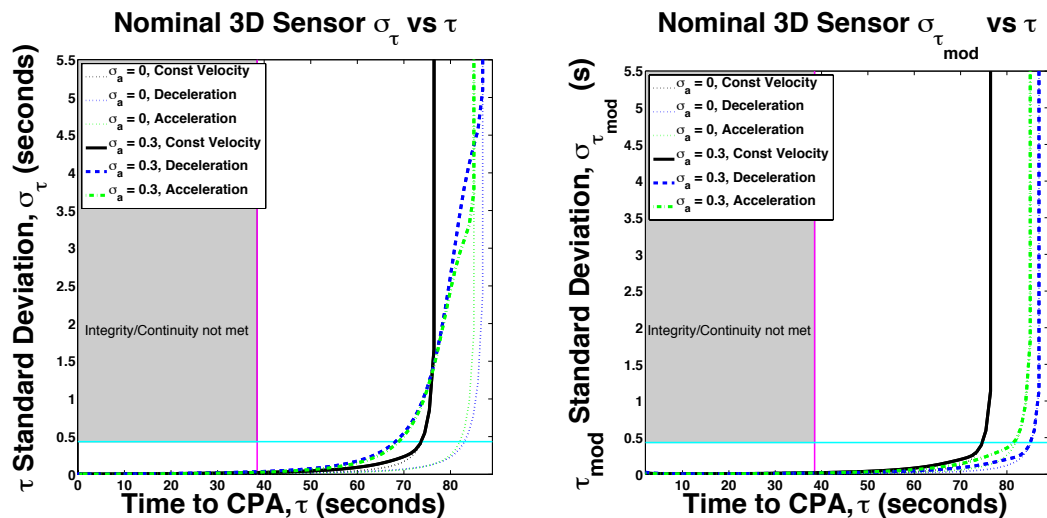


Figure 7.2. Nominal Sensor Tau Comparison

What is notable is the difference between τ_{mod} and the true tau that accounts for accelerations, depicted in Figure 7.2. Here, there is a significant difference between the curves. Since the expression for τ_{true} includes the constant acceleration states, it is more accurate than τ_{mod} which is an approximation that only includes position and velocity states. The TCAS II MOPS described the D_{mod} term in τ_{mod} as a “safety factor incorporated in range measurements to account for possible accelerations by the

intruder” [70]. The τ_{true} curve separated from the constant velocity case much earlier into a more restrictive position (closer to the upper left quadrant whose boundary signifies the integrity and continuity risk requirement) than the τ_{mod} curve.

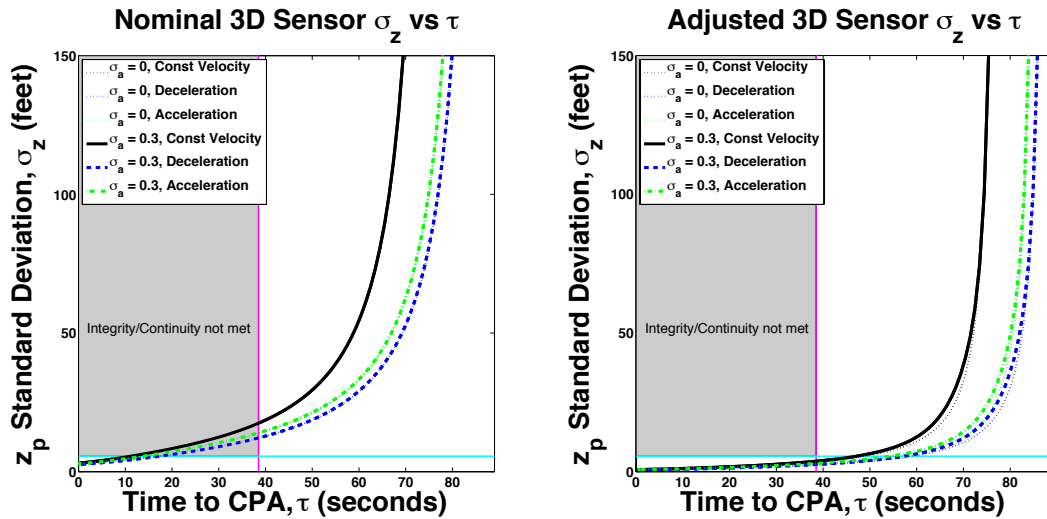


Figure 7.3. Results of an Adjusted Sensor, $\sigma_\phi = 0.01^\circ$

As in the constant velocity case, the sensor can be adjusted to meet integrity and continuity requirements. An example of this is in Figure 7.3. Here, the sensor elevation uncertainty was improved to $\sigma_\phi = 0.01^\circ$. Now, as in the constant velocity case, the sensor does meet integrity and continuity requirements. This is an example of exploring the sensor requirement trade space.

7.4 Summary of Intruder Linear Accelerations

This analysis shows it is possible to account for uncertainties in straight line intruder dynamics while finding sensor uncertainty characteristics that meet integrity and continuity requirements. However, the uncertainties in straight line intruder dynamics impact τ more than the other hazard states. Also, the constant acceleration τ_{true} was more restrictive and accurate than the τ_{mod} . This version of τ_{true} may be a more appropriate τ hazard state when addressing SAA accelerations. Opportunities

for future work include accounting for intruder turning trajectories and wind gusts.

CHAPTER 8

MULTIPLE INTRUDERS

The last significant contribution of this thesis is developing a methodology to evaluate integrity and continuity risks of multiple intruders. The first iteration of this multiple intruder research was published in [42]. Integrity risk is addressed through determination of the probability of data mis-associations for multiple intruders. A mis-association occurs when the system incorrectly associates one intruder's measurement with another intruder's trajectory. If an intruder is threatening the well clear threshold, then an incorrect intruder association is hazardously misleading information impacting integrity.

The methodology in this research for determining a mis-association is based on the nearest neighbor method, commonly found in tracking and data association literature [6–8]. The nearest neighbor method involves determining the correct association based on a minimization of the Mahalanobis distance of the innovation vector [6–8, 45, 55]. Based on this data association criterion, a new methodology is developed to determine an analytic upper bound of the probability of incorrect association for the encounter, which is the integrity risk. This analytic upper bound is a departure from previous work, which used computationally expensive numerical methods to determine probability of incorrect associations [6]. A sensitivity analysis is then performed based on two two-intruder encounters. The resulting impact of mis-associations between multiple intruders on integrity and continuity is quantified for a nominal composite SAA sensor. The sensor characteristic trade space is then explored.

8.1 Multiple Intruder Integrity Risk

The following is an innovation domain methodology for determining the im-

pact, or integrity risk, of mis-associating m number of intruders. Figure 8.1 depicts a correctly associated two-intruder encounter. Here, the blue intruder is associated with the blue measurements and the orange intruder is associated with the orange measurements.

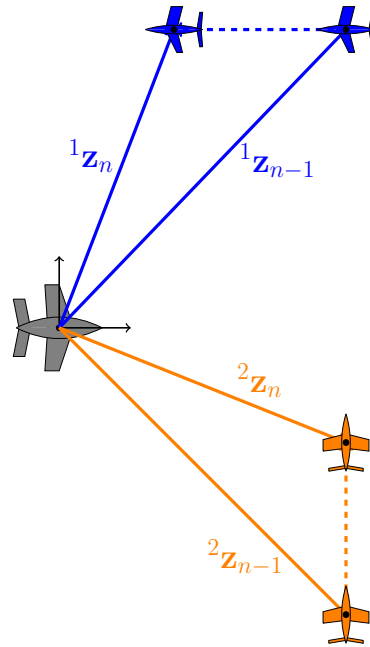


Figure 8.1. Correctly Associated Measurements of Two Intruders

Figure 8.2 depicts a mis-associated two-intruder encounter. The current blue measurement is incorrectly associated with the orange intruder and the current orange measurement is incorrectly associated with the blue intruder. This leads to the system incorrectly estimating the orange and blue trajectories (denoted by the orange and blue dotted lines) with large errors. The estimation error in position is represented by the black dotted line. If either the orange or blue intruder violates the well clear threshold, this incorrect association is hazardously misleading information, impacting integrity risk. The position and velocity of each intruder are depicted as follows:

- ${}^i\mathbf{x}$ = position of intruder i .

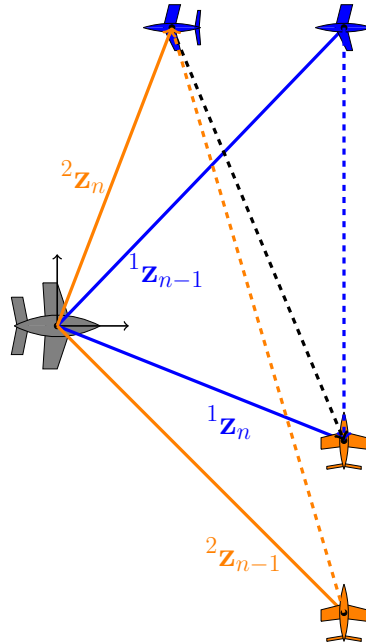


Figure 8.2. Measurement Incorrectly Associated for Two Intruders

- ${}^i\dot{\mathbf{x}}$ = velocity of intruder i .

The discrete-time process-noise-free state-transition equation is:

$$\mathbf{x}_n = \mathbf{F}_m \mathbf{x}_{(n-1)} \quad (8.1)$$

where \mathbf{F}_m represents the constant state-transition matrix for a constant relative velocity encounter for m intruders. For two intruders, \mathbf{F}_2 is:

$$\mathbf{F}_2 = \left[\begin{array}{cc|cc} \mathbf{I}_{3 \times 3} & \Delta t \mathbf{I}_{3 \times 3} & & \\ \mathbf{0}_{3 \times 3} & \mathbf{I}_{3 \times 3} & & \\ \hline & & \mathbf{I}_{3 \times 3} & \Delta t \mathbf{I}_{3 \times 3} \\ & & \mathbf{0}_{3 \times 3} & \mathbf{I}_{3 \times 3} \end{array} \right] \quad (8.2)$$

and the two-intruder trajectory state vector, \mathbf{x} , is based on intruder position and

constant velocity:

$$\mathbf{x} = \begin{bmatrix} {}^1\mathbf{x} & {}^1\dot{\mathbf{x}} & {}^2\mathbf{x} & {}^2\dot{\mathbf{x}} \end{bmatrix}^T \quad (8.3)$$

For m intruders:

$$\mathbf{F}_m = \left[\begin{array}{cc|cc} \mathbf{F}_2 & \cdots & & \\ \vdots & \ddots & & \\ \hline & & \mathbf{0}_{(6m-6) \times 6} & \\ \hline & & \mathbf{I}_{3 \times 3} & \Delta t \mathbf{I}_{3 \times 3} \\ & & \mathbf{0}_{3 \times 3} & \mathbf{I}_{3 \times 3} \end{array} \right] \quad (8.4)$$

and

$$\mathbf{x} = \begin{bmatrix} {}^1\mathbf{x} & {}^1\dot{\mathbf{x}} & {}^2\mathbf{x} & {}^2\dot{\mathbf{x}} & \cdots & {}^m\mathbf{x} & {}^m\dot{\mathbf{x}} \end{bmatrix}^T \quad (8.5)$$

8.1.1 Measurement Model. The own aircraft senses intruders, as in Figure 8.1, in spherical coordinates and range rate. The ordering of the measurements is arbitrary. The intruder i measurement ${}^i\mathbf{z}$, is:

$$\begin{aligned} {}^i\mathbf{z} &= \begin{bmatrix} {}^i\rho & {}^i\theta & {}^i\phi & {}^i\dot{\rho} \end{bmatrix}^T \\ &= \mathfrak{h}({}^i\mathbf{x}, {}^i\dot{\mathbf{x}}) + {}^i\mathbf{v}, \quad {}^i\mathbf{v} \sim N(\mathbf{0}, {}^i\mathbf{R}) \end{aligned} \quad (8.6)$$

$N(\mathbf{a}, \mathbf{B})$ represents a normal distribution with mean, \mathbf{a} , and covariance, \mathbf{B} . ${}^i\mathbf{v}$ is the measurement error, which is assumed to be over-bounded in the cumulative distribution function (CDF) sense by a Gaussian function with covariance matrix ${}^i\mathbf{R}$ [16, 68]. The nonlinear function, \mathfrak{h} , is the transformation of any intruder from Cartesian tra-

jectory states, $\begin{bmatrix} {}^i\mathbf{x} \\ {}^i\dot{\mathbf{x}} \end{bmatrix}$, to the spherical measurements:

$$\mathfrak{h}({}^i\mathbf{x}, {}^i\dot{\mathbf{x}}) = \begin{bmatrix} \sqrt{{}^ix^2 + {}^iy^2 + {}^iz^2} \\ \tan^{-1} \frac{{}^iy}{{}^ix} \\ \sin^{-1} \frac{{}^iz}{\sqrt{{}^ix^2 + {}^iy^2 + {}^iz^2}} \\ {}^i\dot{\mathbf{x}} \cdot \frac{{}^i\mathbf{x}}{\|{}^i\mathbf{x}\|} \end{bmatrix} \quad (8.7)$$

This leads to the form:

$$\mathbf{z} = \mathbf{h}(\mathbf{x}) + \mathbf{v} \quad (8.8)$$

where the stacked measurements are for m intruders:

$$\mathbf{z} = \begin{bmatrix} \mathbf{z}_1 & \mathbf{z}_2 & \dots & \mathbf{z}_m \end{bmatrix}^T \quad (8.9)$$

and the nonlinear observation, $\mathbf{h}(\mathbf{x})$, is:

$$\mathbf{h}(\mathbf{x}) = \begin{bmatrix} \mathfrak{h}({}^1\mathbf{x}, {}^1\dot{\mathbf{x}}) \\ \mathfrak{h}({}^2\mathbf{x}, {}^2\dot{\mathbf{x}}) \\ \vdots \\ \mathfrak{h}({}^m\mathbf{x}, {}^m\dot{\mathbf{x}}) \end{bmatrix} \quad (8.10)$$

The stacked measurement error is:

$$\mathbf{v} = \begin{bmatrix} {}^1\mathbf{v} \\ {}^2\mathbf{v} \\ \vdots \\ {}^m\mathbf{v} \end{bmatrix} \sim N(\mathbf{0}, \mathbf{V}), \mathbf{V} = \begin{bmatrix} {}^1\mathbf{R} & \mathbf{0} & \cdots & \mathbf{0} \\ \mathbf{0} & {}^2\mathbf{R} & \cdots & \mathbf{0} \\ \vdots & \vdots & \ddots & \vdots \\ \mathbf{0} & \mathbf{0} & \cdots & {}^m\mathbf{R} \end{bmatrix} \quad (8.11)$$

The same sensor performance characteristics are assumed for all measurements, so the measurement error covariance for each measurement is \mathbf{R} . It is also assumed that a sample interval, Δt , is selected large enough to ensure independence of sequential sensor measurement errors.

8.1.2 Prediction Estimate and Covariance. The following equations show the implementation of the state transition equation (8.1) and measurement equation (8.8) into the Kalman filter [35] for a correct association (CA). No prior knowledge is assumed on the trajectory states. The state estimate prediction is:

$$\bar{\mathbf{x}}_n = \mathbf{F}\hat{\mathbf{x}}_{(n-1)} \quad (8.12)$$

and the estimate error prediction covariance:

$$\bar{\mathbf{P}}_n = \mathbf{F}\hat{\mathbf{P}}_{(n-1)}\mathbf{F}^T \quad (8.13)$$

8.1.3 Measurement Association. Considering m intruders, there are $m!$ possible measurement associations. An arbitrary ordering of \mathbf{z} for the measurement vector is chosen. Then the observation function, \mathbf{h}_j , is varied to match the correct observation,

\mathbf{h}_* . For the measurement, \mathbf{z} , the innovation vector, $\boldsymbol{\gamma}_j$, is:

$$\boldsymbol{\gamma}_j = \mathbf{z} - \mathbf{h}_j(\bar{\mathbf{x}}), \quad j = 1, \dots, m! \quad (8.14)$$

where

$$\mathbf{z} = \mathbf{h}_*(\mathbf{x}) + \mathbf{v}, \quad \mathbf{v} \sim N(\mathbf{0}, \mathbf{V}) \quad (8.15)$$

therefore

$$\begin{aligned} \boldsymbol{\gamma}_j &= \mathbf{h}_*(\mathbf{x}) + \mathbf{v} - \mathbf{h}_j(\bar{\mathbf{x}}) \\ &\approx \mathbf{h}_*(\mathbf{x}) + \mathbf{v} - \mathbf{h}_j(\mathbf{x}) - \mathbf{H}_j \bar{\boldsymbol{\varepsilon}} \end{aligned} \quad (8.16)$$

Here, a first order Taylor series approximation is applied to the nonlinear observation $\mathbf{h}_j(\mathbf{x})$ about a state estimate, $\bar{\mathbf{x}}$:

$$\mathbf{h}_j(\mathbf{x}) \approx \mathbf{h}_j(\bar{\mathbf{x}}) - \mathbf{H}_j(\bar{\mathbf{x}} - \mathbf{x}) \quad (8.17)$$

the approximate observation matrix, \mathbf{H}_j , is:

$$\mathbf{H}_j \triangleq \left. \frac{\partial \mathbf{h}_j}{\partial \mathbf{x}} \right|_{\bar{\mathbf{x}}} \quad (8.18)$$

and $\bar{\boldsymbol{\varepsilon}}$ is the state estimate error.

A fault term, \mathbf{y}_j , is defined representing the error between the correct observation, $\mathbf{h}_*(\mathbf{x})$, and the observation in question, $\mathbf{h}_j(\mathbf{x})$:

$$\mathbf{y}_j \triangleq \mathbf{h}_*(\mathbf{x}) - \mathbf{h}_j(\mathbf{x}) \quad (8.19)$$

therefore, the innovation vector is:

$$\boldsymbol{\gamma}_j \approx \mathbf{y}_j - \mathbf{H}_j \bar{\boldsymbol{\varepsilon}} + \mathbf{v} \quad (8.20)$$

with a mean of \mathbf{y}_j and a covariance, $\mathbf{\Lambda}_j$:

$$\boldsymbol{\gamma}_j \sim N(\mathbf{y}_j, \mathbf{\Lambda}_j) \quad (8.21)$$

where

$$\mathbf{\Lambda}_j \triangleq \mathbf{H}_j \bar{\mathbf{P}} \mathbf{H}_j^T + \mathbf{V} \quad (8.22)$$

8.1.4 Criterion for Measurement Assignment. A nearest neighbor test based on minimizing the Mahalanobis distance of the normalized innovation vector is employed to determine the observation function with the correct measurement assignment [6–8, 55]. This data association rule is to associate the correct observation to the measurement, $\mathbf{h}_{j^*}(\mathbf{x}) \rightarrow \mathbf{z}$ if:

$$j^* = \underset{j}{\operatorname{argmin}} \|\boldsymbol{\gamma}_j\|_{\mathbf{\Lambda}_j^{-1}} \quad (8.23)$$

where $\|\boldsymbol{\gamma}_j\|_{\mathbf{\Lambda}_j^{-1}}$ is:

$$\|\boldsymbol{\gamma}_j\|_{\mathbf{\Lambda}_j^{-1}} = \sqrt{\boldsymbol{\gamma}_j^T \mathbf{\Lambda}_j^{-1} \boldsymbol{\gamma}_j} \quad (8.24)$$

8.1.5 Estimate Update and Estimate Error Covariance. With an observation, j^* , associated with the measurement, the state estimate update is:

$$\hat{\mathbf{x}}_n = \bar{\mathbf{x}}_n + \mathbf{K}_n \boldsymbol{\gamma}_{j^*} \quad (8.25)$$

and the estimate error covariance is:

$$\hat{\mathbf{P}}_n = (\mathbf{I} - \mathbf{K}_n \mathbf{H}_{j^*}) \bar{\mathbf{P}}_n \quad (8.26)$$

where the Kalman gain matrix is:

$$\mathbf{K}_n = \bar{\mathbf{P}}_n \mathbf{H}_{j^*}^T (\mathbf{H}_{j^*} \bar{\mathbf{P}}_n \mathbf{H}_{j^*}^T + \mathbf{V}_n)^{-1} \quad (8.27)$$

8.1.6 Bounds on Probability of Correct and Incorrect Associations. The following is a methodology to place analytic bounds on the probability of correct association, $P(CA)$, and the probability of incorrect association, $P(IA)$. Bar-Shalom, et al., provides a detailed derivation of the probability of correct association given measurements [7]. However, a risk prediction capability, desired for safety critical applications such as SAA, is lacking in this Bayesian approach. Another disadvantage of this approach and the approach in [11] is the the problem of bounding the posterior probability of association. Areta's approach to determining the probability of incorrect association makes approximations that would not guarantee safe operation [6]. In addition, Areta presents an exact solution that could only be evaluated using computationally expensive numerical integration methods [6]. In response, this research presents a different methodology, placing an analytic bound on the probability of incorrect association in offline analysis for sensor certification, with the intention of expanding this methodology to the future application of online analysis for the avoidance maneuver function of SAA.

Offline, the correct ordering of $\mathbf{h}_j(\mathbf{x})$ is known. Correct association is indicated with a subscript 0. The remaining incorrect observation functions are renumbered from $\mathbf{h}_1(\mathbf{x})$ to $\mathbf{h}_{m-1}(\mathbf{x})$. Also, the correct normalized innovation vector is zero mean, since $\mathbf{y}_0 = 0$.

$P(IA)$ can be found by summing the probabilities that the normalized correct

innovation is larger than each of the other normalized innovations:

$$P(IA) = P\left(\bigcup_{j=1}^{m!-1} \|\boldsymbol{\gamma}_j\|_{\boldsymbol{\Lambda}_j^{-1}} \leq \|\boldsymbol{\gamma}_0\|_{\boldsymbol{\Lambda}_0^{-1}}\right) \quad (8.28)$$

The innovation vector in equation (8.20) is rewritten:

$$\boldsymbol{\gamma}_j = \mathbf{y}_j + \begin{bmatrix} -\mathbf{H}_j & \mathbf{I} \end{bmatrix} \begin{bmatrix} \bar{\boldsymbol{\varepsilon}} \\ \mathbf{v} \end{bmatrix} = \mathbf{y}_j + \mathbf{M}_j^T \mathbf{w} \quad (8.29)$$

where

$$\mathbf{M} = \begin{bmatrix} -\mathbf{H}_j & \mathbf{I} \end{bmatrix}^T \quad (8.30)$$

$$\mathbf{w} = \begin{bmatrix} \bar{\boldsymbol{\varepsilon}} \\ \mathbf{v} \end{bmatrix}, \quad \mathbf{w} \sim N(\mathbf{0}, \mathbf{W}) \quad (8.31)$$

$$\mathbf{W} = \begin{bmatrix} \bar{\mathbf{P}} & \mathbf{0} \\ \mathbf{0} & \mathbf{V} \end{bmatrix} \quad (8.32)$$

Now the incorrect association inequality per pair, $\|\boldsymbol{\gamma}_j\|_{\boldsymbol{\Lambda}_j^{-1}} \leq \|\boldsymbol{\gamma}_0\|_{\boldsymbol{\Lambda}_0^{-1}}$, becomes:

$$\|\mathbf{y}_j + \mathbf{M}_j^T \mathbf{w}\|_{\boldsymbol{\Lambda}_j^{-1}} \leq \|\mathbf{M}_0^T \mathbf{w}\|_{\boldsymbol{\Lambda}_0^{-1}} \quad (8.33)$$

The left hand side can be bounded:

$$\|\mathbf{y}_j\|_{\boldsymbol{\Lambda}_j^{-1}} - \|\mathbf{M}_j^T \mathbf{w}\|_{\boldsymbol{\Lambda}_j^{-1}} \leq \|\mathbf{y}_j + \mathbf{M}_j^T \mathbf{w}\|_{\boldsymbol{\Lambda}_j^{-1}} \quad (8.34)$$

The incorrect association per pair inequality is now:

$$\|\mathbf{y}_j\|_{\Lambda_j^{-1}} - \|\mathbf{M}_j^T \mathbf{w}\|_{\Lambda_j^{-1}} \leq \|\mathbf{M}_0^T \mathbf{w}\|_{\Lambda_0^{-1}} \quad (8.35)$$

This is equivalent to:

$$\|\mathbf{y}_j\|_{\Lambda_j^{-1}} \leq \|\mathbf{M}_0^T \mathbf{w}\|_{\Lambda_0^{-1}} + \|\mathbf{M}_j^T \mathbf{w}\|_{\Lambda_j^{-1}} \quad (8.36)$$

λ_j^2 is defined as the maximum eigenvalue of $\mathbf{W}^{\frac{1}{2}}(\mathbf{M}_j \Lambda_j^{-1} \mathbf{M}_j^T) \mathbf{W}^{\frac{1}{2}}$ and λ_0^2 is defined as the maximum eigenvalue of $\mathbf{W}^{\frac{1}{2}}(\mathbf{M}_0 \Lambda_0^{-1} \mathbf{M}_0^T) \mathbf{W}^{\frac{1}{2}}$. Defining vector $\mathbf{q} = \mathbf{W}^{-\frac{1}{2}} \mathbf{w}$ and $q^2 = \mathbf{q}^T \mathbf{q}$, the incorrect association inequality becomes:

$$\|\mathbf{y}_j\|_{\Lambda_j^{-1}}^2 \leq q^2 (\lambda_j + \lambda_0)^2, \quad q^2 \sim \chi^2(n_w) \quad (8.37)$$

where q^2 is chi-squared distributed with n_w degrees of freedom. n_w is the length of \mathbf{w} , which is the number of measurements plus the number of states.

Defining $y_j^2 = \|\mathbf{y}_j\|_{\Lambda_j^{-1}}^2$, the probability of incorrect association per epoch in equation (8.28) is now rewritten as an upper bound:

$$P(IA_n) \leq P\left(\bigcup_{j=1}^{m-1} y_{j,n}^2 \leq q^2 (\lambda_{j,n} + \lambda_{0,n})^2\right) \quad (8.38)$$

Placing the test statistic on one side, the upper bound on the probability of incorrect association per epoch is now:

$$P(IA_n) \leq P\left(q^2 \geq \min_j \left(\frac{y_{j,n}^2}{(\lambda_{j,n} + \lambda_{0,n})^2}\right)\right) \quad (8.39)$$

The probability of correct association per epoch is $1 - P(IA_n)$, which is now lower

bounded:

$$P(CA_n) \geq 1 - P\left(q^2 \geq \min_j \left(\frac{y_{j,n}^2}{(\lambda_{j,n} + \lambda_{0,n})^2}\right)\right) \quad (8.40)$$

8.1.7 Integrity Risk. At any epoch, n , the probability of correct association for the entire encounter up to that point is:

$$P(CA_N) = \prod_{\ell=1}^n P(CA_\ell | CA_{\ell-1}), \quad L \triangleq 1, \dots, \ell \quad (8.41)$$

where N is a notation to designate all time increments: $\{1, \dots, n\}$. Event CA_N is a correct association from 1 to n , or the intersection of CA_1, \dots, CA_n . CA_{N-1} assumes that correct associations from $1, \dots, n-1$. Note, at the initial epoch ($n=0$), the assignment of intruders is arbitrary, so the probability of correct association is one ($P(CA_0) = 1$) and the probability of incorrect association is zero ($P(IA_0) = 0$).

If at any time in the past, there was an incorrect association, the resulting integrity risk at the current time, n , is assumed to be one. Computing the integrity risk at time n due to previous potential incorrect associations is not practical, because of the number of possible cases. The probability of being in this state at time n is $1 - P(CA_N)$ because state CA_N requires correct associations all the way to the current time n .

Therefore the integrity risk at time n is upper bounded as:

$$P(HMI_n) \leq 1 - [1 - P(HMI_n | CA_N)]P(CA_N) \quad (8.42)$$

where $P(HMI_n | CA_N)$ is the integrity risk for a single threatening intruder based on the hazard states, as described in Chapter 3, as well as the previous work [40, 43, 44]. This upper bound needs to be less than, I_{SS} , the full integrity risk requirement for

self-separation:

$$1 - [1 - P(HMI_n|CA_N)]P(CA_N) \leq I_{SS} \quad (8.43)$$

or written another way:

$$P(HMI_n|CA_N) \leq 1 + \frac{I_{SS} - 1}{P(CA_N)} \quad (8.44)$$

This expression is another way to write equation (3.8), with the right hand side of equation (8.44) replacing the right hand side of equation (3.8).

8.2 Continuity Risk

Continuity risk is indirectly impacted by the data association's influence on integrity. As described in Chapter 4, and the previous work [40, 43, 44], integrity and continuity requirements together are used to select coefficients of integrity and continuity that when summed together, result in a protection level around the own aircraft. Since the integrity risk in equation (8.44) is now influenced by data association, the resulting selection of integrity risk coefficients used to determine $P(HMI_n|CA_N)$ could change to ensure the I_{SS} requirement is met. This has a second order effect on continuity and the selection of a continuity risk coefficient. For example, if the certification authority desires to keep a strict fractional margin, ϵ , on the protection level around the well clear threshold, an increase in the integrity adjusted thresholds ($k\sigma$'s) would require a corresponding decrease in the continuity buffers ($\ell\sigma$'s). This would have to be done by either lowering the continuity requirement (decreasing ℓ 's) or improving sensor performance (decreasing σ 's).

8.3 Analysis

This analysis looks at two two-intruder encounters. The composite nominal sensor of Chapter 6 is applied: σ_ρ is 5 feet, σ_θ is 0.05° , σ_ϕ is 0.05° , $\sigma_{\dot{\rho}}$ is 5 ft/s, and

detection range is 8 NM. The DAA MOPS WCT is also used: τ_{SS} of 35 seconds, r_{MD} of 4000 feet, and z_{MD} of 450 feet, and a lookahead time of 25 seconds [72]. All operational limit fractional margins are 10% ($\epsilon_\tau = \epsilon_r = \epsilon_z = 10\%$) leading to $\tilde{\tau} = 38.5$ seconds, $\tilde{r} = 4400$ feet, and $\tilde{z} = 495$ feet. The desired integrity requirement, $I_{SS} = 10^{-6}$, and the continuity requirement, $C_{SS} = 10^{-3}$, are based on the FAA's definition of major and minor failure conditions [28]. For simplicity, the integrity and continuity risk coefficients are set to be equal: $k_\tau = k_r = k_z = 4.98$ and $\ell_\tau = \ell_r = \ell_z = 3.09$. Based on the DAA MOPS, the nominal update rate is selected to be 1 Hz and the worst-case relative closure velocity is limited to 370 knots for non-cooperative intruders [72].

For the encounters, the first encounter is where the intruder trajectories are co-altitude, but relatively far within the detection range, and the other encounter is where both intruders are on parallel trajectories, head-on to the own aircraft at ± 500 feet. The intent is to show an encounter with what should be a large fault term, \mathbf{y}_j , and to show another encounter with as small of a fault term, \mathbf{y}_j , as can be reasonably expected, with 1000 feet of altitude separation, but the same velocities and horizontal positions.

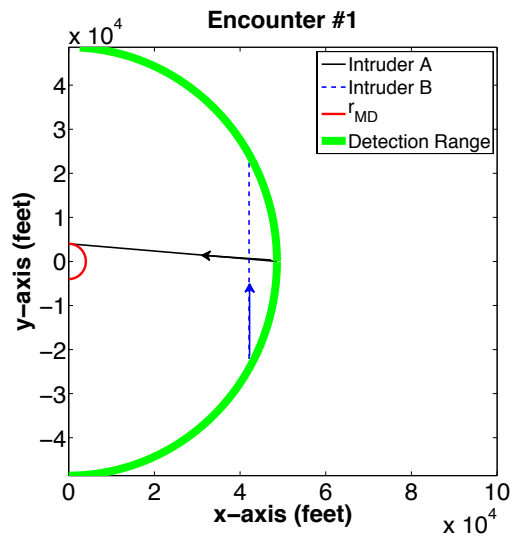


Figure 8.3. First Intruder Encounter

In the first encounter, reflected in Figure 8.3, there is one co-altitude intruder initiating directly in front of the own aircraft at the detection range then continues toward the own aircraft at 370 knots on course with a CPA that is tangent to the 4000 foot horizontal miss distance circle, which would require a warning alert. The other intruder starts at the the detection range at a relative azimuth of -30° and at 370 knots crosses in front of the own aircraft at a perpendicular trajectory (not requiring a warning alert).

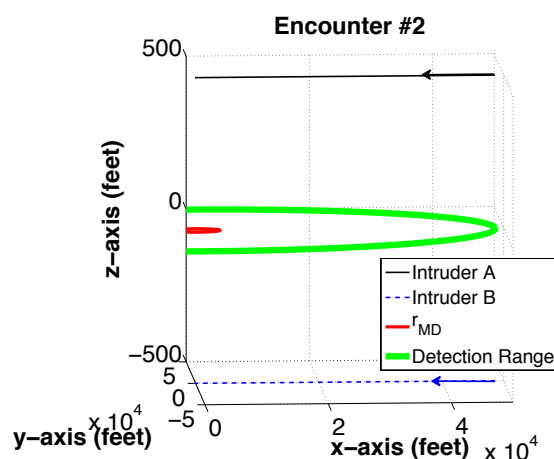


Figure 8.4. Second Intruder Encounter

In the second encounter, reflected in Figure 8.4, a situation is assumed where both intruders are flying under visual flight rules (VFR) and offset from the own aircraft's altitude by ± 500 feet. According to 14 CFR 91.159, any VFR level cruising aircraft higher than 3000 feet above ground level will maintain the following altitudes below 18,000 feet mean sea level: if on a magnetic course 0 - 179 degrees, any odd thousand plus 500 feet (3500, 5500, etc...) or if on a magnetic course 180 - 359 degrees, any even thousand plus 500 feet (4500, 6500, etc...) [2]. The VFR intruders will be assumed to fly in the same boundary heading (either 179.5 degrees or 359.5 degrees) and have a separation of 1000 feet, otherwise, the intruders would normally either

be flying in opposite directions or be separated by 2000 feet. The instrument flight rules (IFR) own aircraft will be assumed to fly on an even 1000 foot IFR altitude in the exact opposite direction, resulting in a 500 foot separation between the own aircraft and the intruders. According to FAA Order JO 7110.65W Section 5-2-17 and Eurocontrol, air traffic controllers consider altitude readouts within ± 300 feet to be valid [27, 32]. This margin for error is greater the ± 50 feet required for a well clear violation if either intruder falls within the own aircraft vertical miss distance, z_{MD} , of ± 450 [72]. Both intruders are assumed to fly at the maximum 370 knots.

8.3.1 Results. To determine the integrity and continuity risks, $P(CA_N)$ and $P(IA_N)$ must be determined. Both of these probabilities are functions of y_j^2 and $(\lambda_j + \lambda_0)^2$. Since there are only two intruders ($m = 2$), $j = 1$ so the j subscript will be removed for the remainder of this subsection. The nature of the probabilities of correct association and incorrect association can be visualized by the y^2 vs τ curve in Figure 8.5. The value of λ_j and λ_0 are both approximately one throughout the encounter, so any differences in probabilities of correct association and incorrect association come from y^2 . The normalized fault term is large throughout the encounter.

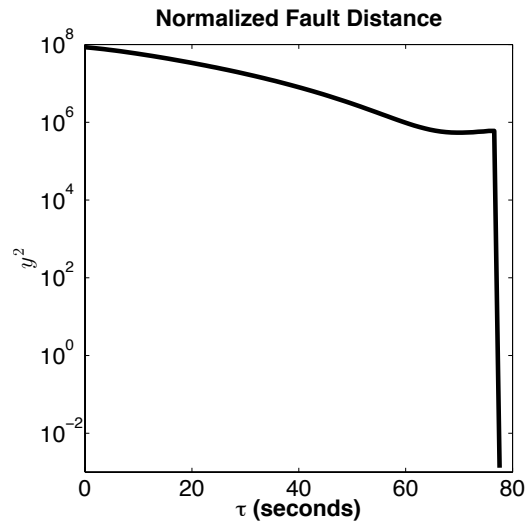


Figure 8.5. Fault Term During the First Encounter

This combination of large y^2 and near constant λ 's lead to a probability of incorrect association of zero during the encounter. This is reflected in Figure 8.6. The

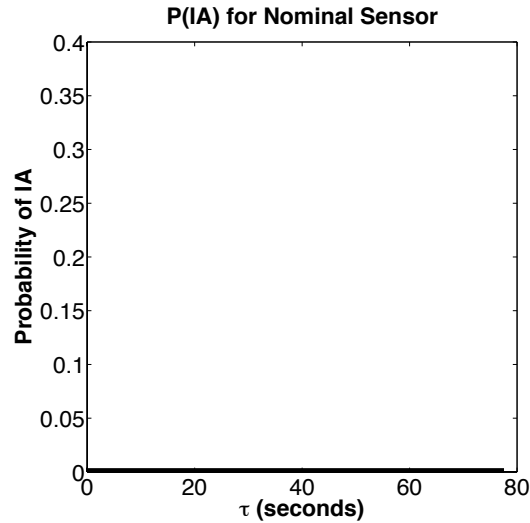


Figure 8.6. First Encounter Probability of Incorrect Association

corresponding $P(CA)$ is one throughout the encounter. This makes sense, since the intruders are so far apart.

For the second encounter, the value of λ_j and λ_0 are both also approximately one throughout the encounter, so again any difference in probabilities of correct association and incorrect association come from y^2 . The result on the upper bound of $P(IA)$, reflected in Figure 8.7, is a spike at the second epoch of over 99.97%, before returning to zero. The resulting lower bound on $P(CA)$ is about 0.03% for the encounter, which includes the 50-50 case, is not acceptable. The normalized fault term in Figure 8.8, which is focused on the initial epochs ($\tau = 72 - 78s$), can help explain why this spike in the $P(IA)$ bound occurred. Here, the fault term is small at $n = 2$, or $\tau = 77s$. This reflects a need for better sensors for velocity, since velocity requires two epochs to estimate.

To improve the $P(IA)$ bound, the sensor range rate uncertainty, $\sigma_{\dot{\rho}}$, was ad-

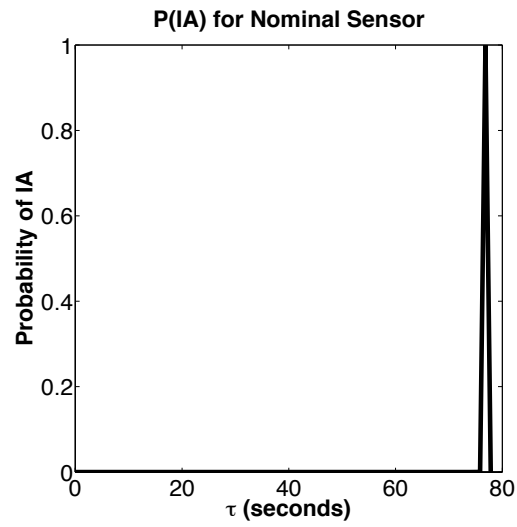


Figure 8.7. Second Encounter Bound on Probability of Incorrect Association

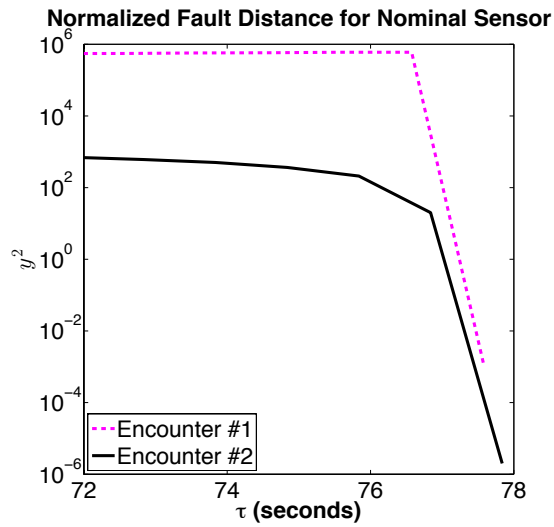


Figure 8.8. Fault Term During the Second Encounter

justed from 5 ft/s to 0.95 ft/s. This adjustment is reflected in Figure 8.9. Here, it is clear that the improved sensor increased the y^2 value at the second epoch, leading to improved integrity. This is an example of how the sensor requirement trade space can be explored to meet data association integrity requirements. The corresponding y^2

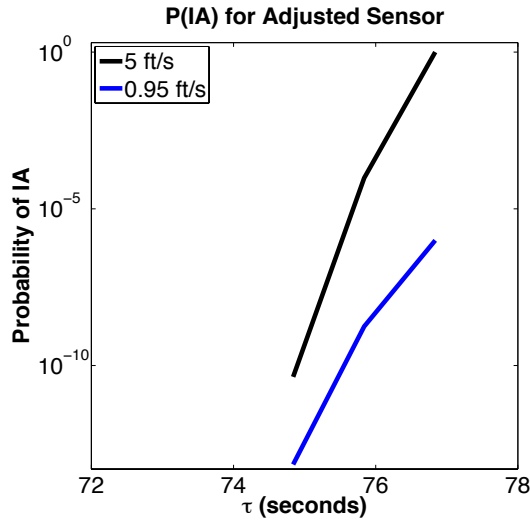


Figure 8.9. Adjusted Sensor $P(IA)$ Bound for Second Encounter

for this improved $P(IA)$ upper bound at the early epochs is depicted in Figure 8.10.

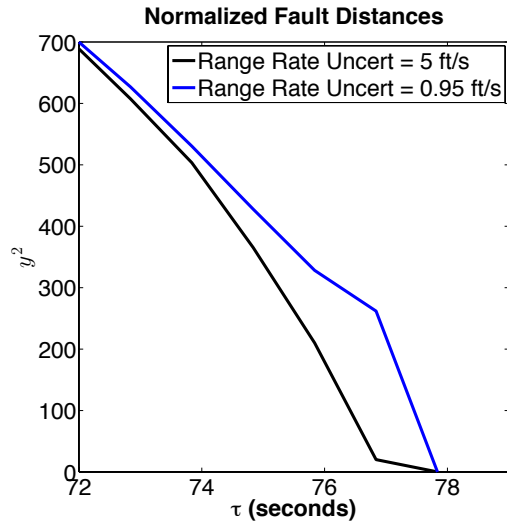


Figure 8.10. Second Encounter Fault Term Sensor Performance Comparison

At a range rate uncertainty of 0.95 ft/s, the $P(IA)$ upper bound is an acceptable 9.82×10^{-7} , leading to a $P(CA)$ lower bound near one. If the original I_{SS} requirement was 10^{-5} , this adjustment would lead to an individual intruder integrity requirement of 0.9×10^{-5} to be applied to equation (3.8) for any intruder threatening to violate the well clear threshold.

8.4 Summary of Multiple Intruders

The integrity risk was determined for mis-associating multiple intruders. This multiple intruder methodology is general and can be used for any number of intruders. Two two-intruder encounters were analyzed to illustrate the methodology. The sensor trade space was explored to meet integrity risk requirements. Suggestions for future work include analysis on greater than two intruders and determining reasonable intruder trajectories, based on encounter models, for all multiple intruder encounters, including for two intruders. This methodology can be used by a certification authority to certify potential SAA sensors.

CHAPTER 9

CONCLUSION

There is currently high interest in providing greater UAS access into the National Airspace System. The FAA will require UAS to employ SAA systems. To ensure an acceptable level of safety, UAS SAA systems must sense intruders to initiate avoidance maneuvers. This dissertation has directly addressed the need to quantify SAA safety through development of new integrity and continuity risk evaluation methods. These methods can ensure safety and lead to certifiable SAA sensor requirements. This dissertation has also explored integrity and continuity for intruder linear accelerations and developed a general method for determining integrity risk of multiple intruders.

9.1 SAA Integrity and Continuity

SAA safety must be guaranteed. This requires methods to quantify safety performance as a function of sensor uncertainty. In response, this dissertation introduced *integrity risk* and *continuity risk* as new UAS SAA safety performance metrics. Integrity and continuity risk are absolute safety metrics [45, 71], as opposed to the current relative UAS safety performance metrics, such as risk ratios [31]. This thesis demonstrated that these new methods to evaluate integrity and continuity risk can be used to establish sensor performance requirements to ensure a predefined level of safety.

9.2 Summary of Achievements

This dissertation directly addressed the need to quantify SAA safety through development of new integrity and continuity risk evaluation methods, which can lead to certifiable SAA sensor requirements. This dissertation has also explored integrity and continuity for intruder linear accelerations and developed a general method for

determining integrity risk of multiple intruders.

9.2.1 Integrity Risk Methodology. This dissertation developed an integrity risk evaluation methodology to quantify SAA safety. Previous research into SAA safety focused on relative safety metrics, such as risk ratios, which is a failure rate with the SAA system divided by the failure rate without the SAA system [48]. The methods developed in this thesis focused directly on the established aviation navigation certification standards that quantify integrity and continuity as absolute safety factors in aircraft approach applications [39, 71]. The methodology ensured an integrity risk requirement was met by surrounding the original WCT by a volume, defined as the integrity-adjusted threshold.

9.2.2 Continuity Risk Methodology. This dissertation also developed a continuity risk evaluation methodology to further quantify SAA safety. As a complement to integrity, continuity is also an absolute safety metric [45, 71]. The methodology ensured a continuity risk requirement was met by accounting for a continuity buffer beyond the integrity-adjusted thresholds. This combination of integrity-adjusted thresholds and continuity buffers result in a protection level that further surrounds the WCT.

9.2.3 Relating Integrity and Continuity Risk to Sensor Requirements. The integrity-adjusted threshold and the continuity buffer together formed a protection level that surrounds the WCT. This protection level resulted in a tradeoff between SAA safety and airspace capacity requirements. To minimize the impact on airspace capacity, an operational limit, based on a fractional margin, was placed on the protection level, resulting in restrictions on sensor performance. A sensitivity analysis explored the sensor requirement trade space for a given operational limit.

9.2.4 Accounting for Linear Accelerations. The trajectory state estimation

model used to build the integrity and continuity risk methodology is based on a constant velocity assumption outlined in the DAA MOPS [72]. Constant velocity was no longer assumed and the estimation model accounted for constant accelerations. Only linear constant intruder accelerations were evaluated, leaving turning and leveling intruder trajectories for future work. An analysis explored the sensor trade space as well as compared modified tau, which does not address accelerations, with a version of true tau, the actual horizontal time to CPA, that included acceleration trajectory states.

9.2.5 Accounting for Multiple Intruders. The final contribution of this dissertation accounted for multiple intruders. A general innovation-based methodology was developed, bounding the probability of mis-associating any number of intruders, which bounded the integrity risk. An analysis explored the sensor requirement trade space for the multiple intruder methodology.

9.3 Future Work

A number of recommendations for future work are given in the following subsections to include expanding the intruder acceleration research to account for all intruder accelerations, further exploring likely intruder trajectories, addressing sensor fault detection, and testing the methods presented in this dissertation on hardware.

9.3.1 Intruder Turning Accelerations. In the draft DAA MOPS, it is assumed that intruder track prediction will be extrapolated using constant velocity [72]. However, it is more realistic to consider intruder trajectories with accelerations. Chapter 7 of this thesis addressed constant linear accelerations. That assumes the intruder will maintain a straight line trajectory. To complete the work on intruder accelerations, intruder trajectories that turn and/or change climb and descent rates will need to be addressed. This will involve hazard state definitions that take the full relative

intruder dynamics into account. The impact of wind gusts on intruder dynamics can also be considered.

9.3.2 Exploring Likely Intruder Trajectories. The intruder trajectories analyzed in Chapters 6, 7, and 8 were based on inspection, flying regulations, and the author’s aviation experience. More detailed research on intruder trajectories can be found in the MIT LL’s correlated and uncorrelated encounter models, which can also be found in Appendix A of the DAA MOPS [49, 50].

9.3.3 Sensor Fault Detection. Sensors can be noisy and this thesis developed an integrity and continuity risk methodology based on the standard deviations associated with sensor uncertainty. At the same time, sensors can be faulty and these faults need to be detected. Then these undetected faults need to be evaluated for their impact on integrity and continuity risk.

9.3.4 Hardware Testing. The Illinois Institute of Technology’s Navigation Laboratory has procured an octocopter and a LIDAR sensor with the intent of flight testing the methods presented in this dissertation. The intent of the flight test would be to determine if the integrity and continuity risk evaluation methodology can be applied online and determine if there are any shortfalls resulting from the linearizations and bounds used within the methodology. Figure 9.1 shows the DJI Spreading Wings S1000 Octocopter. It has a center frame diameter of 33.7 cm, a frame arm length of 38.6 cm and a propeller size of 15 in x 5.2 in [20]. Figure 9.2 shows the Velodyne VLP-16 LIDAR PUCK™. It has a target range of 150-200 m, power consumption of less than 10 Watts, a weight of 830 grams, a size of 10 cm x 6.5 cm, a vertical field of view of $\pm 15^\circ$, and a horizontal field of view of 360° [82].

9.4 Closing

Integrity and continuity risk are absolute measures of safety that can be used



Figure 9.1. DJI Spreading Wings S1000



Figure 9.2. Velodyne VLP-16 LIDAR PUCK™

to set requirements on UAS SAA sensors for integration into the NAS.

APPENDIX A
INTRUDER TRAJECTORY STATE ESTIMATION

The SAA problem is presented as a three dimensional, two-body problem. The two bodies are the own aircraft and the intruder aircraft. The coordinate frame is an own-aircraft-centered body frame. The intruder aircraft is assumed to have a constant relative velocity. The case of straight-line constant intruder accelerations is addressed in Chapter 7.

Figure 2.1 is a graphical depiction of the own aircraft and the intruder aircraft in the horizontal and vertical planes. In the horizontal plane, the x and y axes are oriented such that the x -axis is directly out of the nose of the own aircraft. The azimuth, θ is the angle counterclockwise from the x -axis to the horizontal range vector, \mathbf{r} (from the origin to the intruder position on the xy -plane). In the vertical plane, ϕ is the angle from the \mathbf{r} vector up to the slant range vector, ρ .

A.1 Intruder Spherical Measurements

SAA sensors can measure the intruder's relative position (with error) in spherical, Cartesian, or cylindrical coordinates. In Table 2-8 of the draft DAA MOPS, the input intruder measurements from an SAA radar includes relative slant range (ρ), relative range rate ($\dot{\rho}$), relative bearing (θ), and elevation angle (ϕ) [72]. As a result, this measurement model will assume intruder measurements of range, range rate, azimuth angle and elevation angle as expressed in equation (A.1):

$$\mathbf{z} = \begin{bmatrix} \rho & \theta & \phi & \dot{\rho} \end{bmatrix}^T \quad (\text{A.1})$$

This development assumes spherical measurement vectors. However, the relative intruder trajectory states, intruder position and velocity, are in Cartesian coordinates. Therefore, the spherical measurements will need to be converted to Cartesian states.

A.2 Measurement Model

The own aircraft makes a scan at time n measuring the the intruder position:

$$\mathbf{z}_n = \mathbf{h}(\mathbf{x}_n) + \mathbf{v}_n \quad \mathbf{v}_n \sim N(\mathbf{0}, \mathbf{V}_n) \quad (\text{A.2})$$

\mathbf{z}_n is the measurement at time n :

$$\mathbf{z}_n = \left[\begin{array}{cccc} \rho_n & \theta_n & \phi_n & \dot{\rho}_n \end{array} \right]^T \quad (\text{A.3})$$

The measurement vector (\mathbf{z}_n) is a nonlinear function ($\mathbf{h}(\mathbf{x}_n)$) of the trajectory states (\mathbf{x}_n) which are intruder Cartesian position and velocity. \mathbf{v}_n is the measurement error, which is assumed to be over-bounded in the cumulative distribution function (CDF) sense by Gaussian distributions [16, 68]. The measurement error covariance matrix at each time is \mathbf{V}_n . In equation (A.2), $N(\mathbf{a}, \mathbf{B})$ represents a normal distribution with mean \mathbf{a} and covariance \mathbf{B} . It is assumed that the sample interval, Δt , is selected large enough to ensure independence of sequential sensor measurement errors.

The measurement equation (A.2) can be linearized. Using a first order Taylor series:

$$\mathbf{h}(\mathbf{x}) \approx \mathbf{h}(\bar{\mathbf{x}}) + \mathbf{H}\delta\mathbf{x} \quad (\text{A.4})$$

where \mathbf{H} is the observation matrix:

$$\mathbf{H} = \frac{\partial \mathbf{h}}{\partial \mathbf{x}} \quad (\text{A.5})$$

The partial derivatives of \mathbf{h} with respect to \mathbf{x} are derived in Appendix F.

$\bar{\mathbf{x}}$ is an estimate of the trajectory states, and $\delta\mathbf{x}$ is the estimate error $\bar{\mathbf{x}} - \mathbf{x}$. Substituting into equation (A.2), \mathbf{z}_n becomes:

$$\mathbf{z}_n \approx \mathbf{h}(\bar{\mathbf{x}}_n) + \mathbf{H}\delta\mathbf{x}_n + \mathbf{v}_n \quad (\text{A.6})$$

Then expanding $\delta \mathbf{x}$ and putting all known quantities on the left hand side, \mathbf{z}_n becomes:

$$\mathbf{z}_n - \mathbf{h}(\bar{\mathbf{x}}_n) + \mathbf{H}\bar{\mathbf{x}}_n \approx +\mathbf{H}\mathbf{x}_n + \mathbf{v}_n \quad (\text{A.7})$$

Defining the left hand side of the equation to be $\mathbf{z}' \triangleq \mathbf{z} - \mathbf{h}(\bar{\mathbf{x}}) + \mathbf{H}\bar{\mathbf{x}}$, a linear measurement model is obtained:

$$\mathbf{z}'_n = \mathbf{H}\mathbf{x}_n + \mathbf{v}_n \quad (\text{A.8})$$

A.3 Constant Velocity Batch Model

This research uses two different methods to evaluate trajectory state estimates, $\hat{\mathbf{x}}$, and their estimate error covariance matrix, $\hat{\mathbf{P}}$. The first is the batch model presented in this section. The other is a Kalman filter presented in the next section. The first iteration of this research employed a batch model [43]. In this batch model, the trajectory states (\mathbf{x}) are constant:

$$\mathbf{x} = \begin{bmatrix} \mathbf{x}_0 & \dot{\mathbf{x}} \end{bmatrix}^T \quad (\text{A.9})$$

The trajectory states are broken down into initial Cartesian relative intruder position, $\mathbf{x}_0 = \begin{bmatrix} x_0 & y_0 & z_0 \end{bmatrix}^T$, and intruder relative velocity, $\dot{\mathbf{x}} = \begin{bmatrix} \dot{x} & \dot{y} & \dot{z} \end{bmatrix}^T$. In this case, Δt is between time t_0 and time t_1 such that $\begin{bmatrix} x_1 & y_1 & z_1 \end{bmatrix}^T = \begin{bmatrix} x_0 & y_0 & z_0 \end{bmatrix}^T + \Delta t \dot{\mathbf{x}}$. The first measurement \mathbf{z}_1 is:

$$\mathbf{z}_1 = \mathbf{h}_1(\mathbf{x}) + \mathbf{v}_1 \quad \mathbf{v}_1 \sim N(\mathbf{0}, \mathbf{V}_1) \quad (\text{A.10})$$

For the batch model, the nonlinear observation \mathbf{h} is a time-variant function of the

constant trajectory states:

$$\mathbf{h}_n(\mathbf{x}) = \begin{bmatrix} \sqrt{(x_0 + n\Delta t\dot{x})^2 + (y_0 + n\Delta t\dot{y})^2 + (z_0 + n\Delta t\dot{z})^2} \\ \tan^{-1} \frac{y_0 + n\Delta t\dot{y}}{x_0 + n\Delta t\dot{x}} \\ \sin^{-1} \frac{z_0 + n\Delta t\dot{z}}{\sqrt{(x_0 + n\Delta t\dot{x})^2 + (y_0 + n\Delta t\dot{y})^2}} \\ \frac{x_0\dot{x} + y_0\dot{y} + z_0\dot{z} + n\Delta t(\dot{x}^2 + \dot{y}^2 + \dot{z}^2)}{\sqrt{(x_0 + n\Delta t\dot{x})^2 + (y_0 + n\Delta t\dot{y})^2 + (z_0 + n\Delta t\dot{z})^2}} \end{bmatrix} \quad (\text{A.11})$$

Once linearized, the first measurement becomes:

$$\mathbf{z}'_1 = \mathbf{H}_1 \mathbf{x} + \mathbf{v}_1 \quad (\text{A.12})$$

Stacking the linearized measurements after each epoch into the standard $z = Hx + v$ measurement equation form:

$$\mathbf{z}'_N = \mathbf{H}_N \mathbf{x} + \mathbf{v}_N \quad (\text{A.13})$$

where the batch measurement vector, \mathbf{z}'_N , the batch observation matrix, \mathbf{H}_N , the trajectory state vector, \mathbf{x} , and batch measurement error vector, \mathbf{v}_N , are:

$$\mathbf{z}'_N = \begin{bmatrix} \mathbf{z}'_0^T & \mathbf{z}'_1^T & \dots & \mathbf{z}'_n^T \end{bmatrix}^T \quad (\text{A.14})$$

$$\mathbf{H}_N = \begin{bmatrix} \mathbf{H}_0 \\ \mathbf{H}_1 \\ \vdots \\ \mathbf{H}_n \end{bmatrix} \quad (\text{A.15})$$

$$\mathbf{x} = \begin{bmatrix} \mathbf{x}_0 \\ \dot{\mathbf{x}} \end{bmatrix} = \begin{bmatrix} x_0 & y_0 & z_0 & \dot{x} & \dot{y} & \dot{z} \end{bmatrix}^T \quad (\text{A.16})$$

$$\mathbf{v}_N = \begin{bmatrix} \mathbf{v}_0^T & \mathbf{v}_1^T & \dots & \mathbf{v}_n^T \end{bmatrix}^T \sim N(\mathbf{0}, \mathbf{V}_N) \quad (\text{A.17})$$

The batch measurement error covariance, \mathbf{V}_N , for all time steps is a block diagonal matrix of the individual time step measurement error covariance matrices (\mathbf{V}_i for $i = 1, \dots, n$) which are not necessarily diagonal themselves:

$$\mathbf{V}_N = \begin{bmatrix} \mathbf{V}_0 & \mathbf{0} & \dots & \mathbf{0} \\ \mathbf{0} & \mathbf{V}_1 & \dots & \mathbf{0} \\ \vdots & \vdots & \ddots & \vdots \\ \mathbf{0} & \mathbf{0} & \dots & \mathbf{V}_n \end{bmatrix} \quad (\text{A.18})$$

A weighted least squares estimator is used to get the *trajectory state* estimate vector, $\hat{\mathbf{x}}_n$:

$$\hat{\mathbf{x}}_n = (\mathbf{H}_N^T \mathbf{V}_N^{-1} \mathbf{H}_N)^{-1} \mathbf{H}_N^T \mathbf{V}_N^{-1} \mathbf{z}'_N \quad (\text{A.19})$$

In addition, the corresponding trajectory state estimate error covariance, $\hat{\mathbf{P}}_N$, is then:

$$\hat{\mathbf{P}}_N = (\mathbf{H}_N^T \mathbf{V}_N^{-1} \mathbf{H}_N)^{-1} \quad (\text{A.20})$$

A.4 Kalman Filter Estimation Model

This section presents a Kalman filter model to get the trajectory state estimates, $\hat{\mathbf{x}}$, and estimate error covariance, $\hat{\mathbf{P}}$. A batch model can become extremely computationally expensive as the number of epochs increases. A Kalman filter, on

the other hand, is more computationally efficient. In this Kalman filter model, the trajectory state vector, \mathbf{x}_n , is time variant, based on current intruder position and velocity:

$$\mathbf{x}_n = \begin{bmatrix} x_n & y_n & z_n & \dot{x}_n & \dot{y}_n & \dot{z}_n \end{bmatrix}^T \quad (\text{A.21})$$

The following equations are based on the Kalman filter equations in Gelb's Table 4.2-1 [35]. The discrete-time process-noise-free state-transition equation is:

$$\mathbf{x}_n = \mathbf{F}\mathbf{x}_{(n-1)} \quad (\text{A.22})$$

where \mathbf{F} represents the constant state-transition matrix:

$$\mathbf{F} = \begin{bmatrix} \mathbf{I}_{3 \times 3} & \Delta t \mathbf{I}_{3 \times 3} \\ \mathbf{0}_{3 \times 3} & \mathbf{I}_{3 \times 3} \end{bmatrix} \quad (\text{A.23})$$

The measurement model in equation (A.2) and the measurement vector in equation (A.3) remains the same. However, the nonlinear observation \mathbf{h} for the batch was a time variant function of constant trajectory states and current epoch (n). The Kalman filter nonlinear observation is only a function of the current trajectory states:

$$\mathbf{h}(\mathbf{x}_n) = \begin{bmatrix} \sqrt{x_n^2 + y_n^2 + z_n^2} \\ \tan^{-1} \frac{y_n}{x_n} \\ \sin^{-1} \frac{z_n}{\sqrt{x_n^2 + y_n^2 + z_n^2}} \\ \frac{x_n \dot{x}_n + y_n \dot{y}_n + z_n \dot{z}_n}{\sqrt{x_n^2 + y_n^2 + z_n^2}} \end{bmatrix} \quad (\text{A.24})$$

The linearized approximate observation matrix, \mathbf{H} is found by applying equation

(A.5), leading to the linearized measurement model at each epoch:

$$\mathbf{z}'_n = \mathbf{H}_n \mathbf{x}_n + \mathbf{v}_n, \quad \mathbf{v}_n \sim N(\mathbf{0}, \mathbf{V}_n) \quad (\text{A.25})$$

To apply the Kalman filter, the initial ($n = 0$) conditions are:

$$\begin{aligned} \bar{\mathbf{x}}_0 &= \mathbf{0} \\ \mathbf{K}_0 &= \bar{\mathbf{P}}_0 \mathbf{H}_0^T (\mathbf{H}_0 \bar{\mathbf{P}}_0 \mathbf{H}_0^T + \mathbf{V}_0)^{-1} \\ \hat{\mathbf{P}}_0 &= (\mathbf{I} - \mathbf{K}_0 \mathbf{H}_0) \bar{\mathbf{P}}_0 \end{aligned} \quad (\text{A.26})$$

where $\bar{\mathbf{P}}_0$ is the initial a-priori position and velocity estimate error covariance and no prior knowledge is assumed on these states.

For $n > 0$, state estimate extrapolation is:

$$\bar{\mathbf{x}}_n = \mathbf{F} \hat{\mathbf{x}}_{(n-1)} \quad (\text{A.27})$$

and the error covariance extrapolation matrix is:

$$\bar{\mathbf{P}}_n = \mathbf{F} \hat{\mathbf{P}}_{(n-1)} \mathbf{F}^T \quad (\text{A.28})$$

The state estimate update is:

$$\hat{\mathbf{x}}_n = \bar{\mathbf{x}}_n + \mathbf{K}_n (\mathbf{z}_n - \mathbf{H}_n \bar{\mathbf{x}}_n) \quad (\text{A.29})$$

and the error covariance update matrix is:

$$\hat{\mathbf{P}}_n = (\mathbf{I} - \mathbf{K}_n \mathbf{H}_n) \bar{\mathbf{P}}_n \quad (\text{A.30})$$

where the Kalman gain matrix is:

$$\mathbf{K}_n = \bar{\mathbf{P}}_n \mathbf{H}_n^T (\mathbf{H}_n \bar{\mathbf{P}}_n \mathbf{H}_n^T + \mathbf{V}_n)^{-1} \quad (\text{A.31})$$

APPENDIX B
ALTERNATE HAZARD STATES

With the current hazard states dictated by the DAA MOPS, there other derived hazard states, based on previous definitions and assumptions about the WCT, that are discarded. Given the fluid nature of SAA hazard threshold definitions and the draft state of the DAA MOPS, these hazard states could prove useful again if the SAA hazards are changed again.

B.1 Simplified Tau

Simplified tau, τ_{simp} , is the range divided by the range rate [31]:

$$\tau_{simp} = \frac{\rho}{\dot{\rho}} \quad (\text{B.1})$$

B.2 Time to Well Clear Threshold Entry

NASA Langley did a comparison of four different tau's: τ_{simp} , τ_{mod} , τ_{true} , and τ_{ep} [57]. τ_{ep} is the time to the horizontal threshold entry point, which is the point where the intruder is expected to cross the r_{MD} circle.

To get τ_{ep} , where $r_{CPA} = r_{MD}$, equation (2.13) is converted into a quadratic:

$$r_{MD}^2 = (x + \dot{x}\tau_{\pm})^2 + (y + \dot{y}\tau_{\pm})^2 \quad (\text{B.2})$$

where τ_{\pm} is the multiple solution to the quadratic equation and represents both the time to entry point and time to exit point. The corresponding quadratic is:

$$(\dot{x}_n^2 + \dot{y}_n^2)\tau_{\pm}^2 + (2x_n\dot{x}_n + 2y_n\dot{y}_n)\tau_{\pm} + (x_n^2 + y_n^2 - r_{MD}^2) = 0 \quad (\text{B.3})$$

Solving this quadratic for τ_{\pm} , the time to entry, τ_{ep} , is the smaller solution:

$$\tau_{ep} = \tau_{true} - \frac{\sqrt{(x\dot{x} + y\dot{y})^2 - (\dot{x}^2 + \dot{y}^2)(x^2 + y^2 - r_{MD}^2)}}{\dot{x}^2 + \dot{y}^2} \quad (\text{B.4})$$

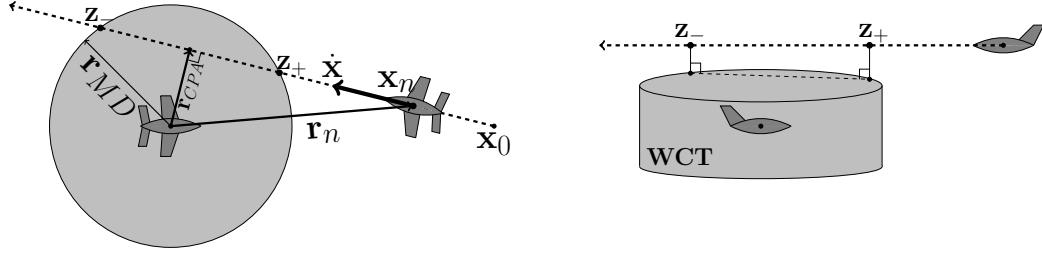


Figure B.1. Vertical Position at Horizontal Entry and Exit

Note, the larger solution for τ_{\pm} is τ_{ex} , the time to well clear exit:

$$\tau_{ex} = \tau_{true} + \frac{\sqrt{(x\dot{x} + y\dot{y})^2 - (\dot{x}^2 + \dot{y}^2)(x^2 + y^2 - r_{MD}^2)}}{\dot{x}^2 + \dot{y}^2} \quad (\text{B.5})$$

B.3 Vertical Position at Well Clear Threshold Entry and Exit

Previous versions of the WCD were represented as cylinders, as in Figure B.1 [14]. An iteration of this research was based on hazards defined by the threshold cylinder [40]. The left part of Figure B.1 is an overhead depiction of the horizontal CPA. For a well clear violation, the intruder must be within the cylinder. That means r_{CPA} is smaller than or equal to the horizontal miss distance (MD), r_{MD} .

For 3D, the SAA system must project intruder trajectories to determine if there is an impending well clear violation. However, determining the z at the CPA is not sufficient. There are some trajectories where either the vertical distance at the 3D CPA or the vertical distance at the 2D horizontal CPA are outside the well clear distance cylinder, but the intruder still penetrates the well clear distance cylinder. For example, consider the head-on trajectories depicted in Figure B.2. Because the distance thresholds define a cylinder and not a sphere, the trajectory intercepting the cylinder at the top-back has a 3D CPA, labeled x_{CPA1} , which is outside the cylinder occurring prior to cylinder entry. Also, the trajectory that intercepts the bottom-

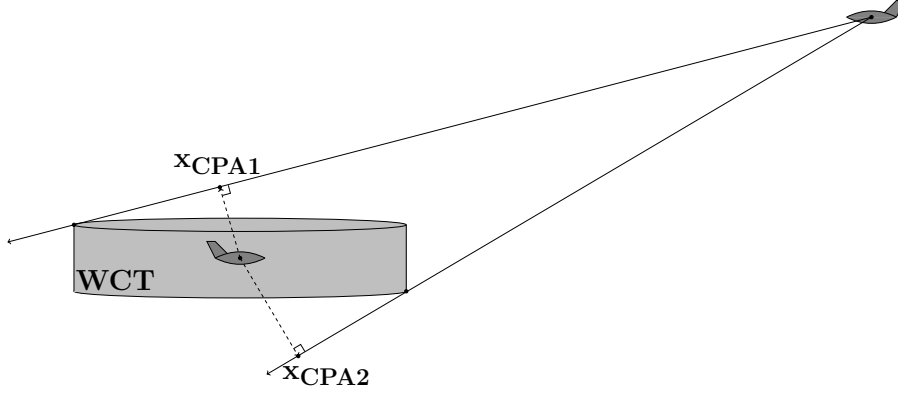


Figure B.2. Head-on Trajectories with 3D Closest Points of Approach

front edge of the cylinder has a 3D CPA, labeled x_{CPA2} , which is outside the cylinder occurring after the well clear violation.

To account for this, there are two vertical hazard states, z_+ and z_- , depicted in Figure B.1. Given that an intruder trajectory penetrates the horizontal miss distance circle, z_+ is the vertical distance when the intruder trajectory enters the 2D horizontal miss distance circle and z_- is the vertical distance when the intruder trajectory exits the 2D horizontal miss distance circle. Figure B.3 shows all nine ways an intruder trajectory can approach the cylinder, based on its z_+ and z_- . In the upper-right section, the intruder passes completely above the cylinder ($z_+ > z_{MD} \cap z_- > z_{MD}$). In the lower-left section, the intruder passes completely below the cylinder ($z_+ < -z_{MD} \cap z_- < -z_{MD}$). In all other cases, the intruder violates the cylinder.

B.3.1 Deriving Vertical Position at Well Clear Entry and Exit. Since only straight line trajectories apply, the slope of the trajectory does not change:

$$\frac{\dot{z}}{\dot{x}} = \frac{z - z_{\pm}}{x - x_{\pm}} \quad (\text{B.6})$$

$$\frac{\dot{z}}{\dot{y}} = \frac{z - z_{\pm}}{y - y_{\pm}} \quad (\text{B.7})$$

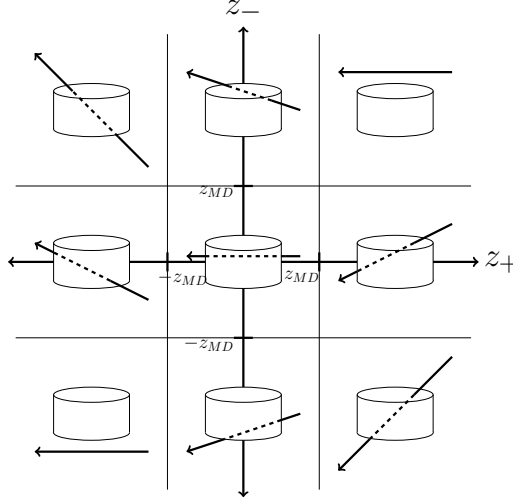


Figure B.3. Possible Intruder Trajectories in $(\hat{z}_+; \hat{z}_-)$ Plane

This can be rewritten to:

$$\dot{z}(x - x_{\pm}) = \dot{x}(z - z_{\pm}) \quad (\text{B.8})$$

$$\dot{z}(y - y_{\pm}) = \dot{y}(z - z_{\pm}) \quad (\text{B.9})$$

Solving for x_{\pm} and y_{\pm}

$$x_{\pm} = x + \frac{\dot{x}}{\dot{z}}(z_{\pm} - z) \quad (\text{B.10})$$

$$y_{\pm} = y + \frac{\dot{y}}{\dot{z}}(z_{\pm} - z) \quad (\text{B.11})$$

Applying the following equation:

$$r_{MD} = \sqrt{x_{\pm}^2 + y_{\pm}^2} = \sqrt{\left(x + \frac{\dot{x}}{\dot{z}}(z_{\pm} - z)\right)^2 + \left(y + \frac{\dot{y}}{\dot{z}}(z_{\pm} - z)\right)^2} \quad (\text{B.12})$$

Leads to the following quadratic:

$$\begin{aligned} & \left(\frac{\dot{x}^2 + \dot{y}^2}{\dot{z}^2}\right)z_{\pm}^2 + \left(\frac{2(x\dot{x} + y\dot{y})}{\dot{z}} - \frac{2z(\dot{x}^2 + \dot{y}^2)}{\dot{z}^2}\right)z_{\pm} \\ & + \left(\frac{z^2(\dot{x}^2 + \dot{y}^2)}{\dot{z}^2} - \frac{2z(x\dot{x} + y\dot{y})}{\dot{z}} + x^2 + y^2 - r_{MD}^2\right) = 0 \end{aligned} \quad (\text{B.13})$$

Solving this quadratic for z_{\pm} leads to expressions for z_+ and z_- :

$$\begin{aligned} z_+ &= z + \frac{\dot{z}}{\dot{x}^2 + \dot{y}^2} (-x\dot{x} - y\dot{y} - \sqrt{(x\dot{x} + y\dot{y})^2 - (\dot{x}^2 + \dot{y}^2)(x^2 + y^2 - r_{MD}^2)}) \\ z_- &= z + \frac{\dot{z}}{\dot{x}^2 + \dot{y}^2} (-x\dot{x} - y\dot{y} + \sqrt{(x\dot{x} + y\dot{y})^2 - (\dot{x}^2 + \dot{y}^2)(x^2 + y^2 - r_{MD}^2)}) \end{aligned} \quad (\text{B.14})$$

APPENDIX C
THE DISTANCE MODIFICATION

There are several similar but different definitions for the Distance Modification, D_{mod} , depending on the reference. This appendix will catalog each definition. Note the DAA MOPS does not define the distance modification beyond being the “distance modification of modified tau” [72].

From the TCAS II MOPS [70]: “Distance Modification (DMOD) - Safety factor incorporated in range measurements to account for possible accelerations by the intruder. The value of distance modification varies with the sensitivity level for this own intruder set. The value is chosen such that a sustained acceleration of $g/3$ will produce this displacement in range threshold time.”

From the FAA Second SAA Workshop [31]: “To provide protection in encounters with a low rate of closure, the tau boundaries may need to have a distance modification (DMOD), similar to that used in TCAS.”

From the Introduction to TCAS II 7.1 [29]: “...at close ranges and at slower closure rates the modified tau boundaries converge to a non-zero range called DMOD. This modification allows TCAS to issue TAs and RAs at or before the fixed DMOD range threshold in these slow-closure-rate encounters.”

APPENDIX D
DERIVATION OF GEOMETRIC HORIZONTAL CPA

The geometric r_{CPA} derived here will prove useful in Chapter 7, where the constant velocity assumption is removed, but the linear trajectory remains.

Since only straight line trajectories apply, the slope of the trajectory does not change:

$$\frac{\dot{y}}{\dot{x}} = \frac{dy}{dx} = \frac{y - y_{CPA}}{x - x_{CPA}} \quad (\text{D.1})$$

This can be rewritten to:

$$\dot{y}(x - x_{CPA}) = \dot{x}(y - y_{CPA}) \quad (\text{D.2})$$

and

$$\dot{y}x_{CPA} - \dot{x}y_{CPA} = \dot{y}x - \dot{x}y \quad (\text{D.3})$$

Coupled with equation (2.9), the following system of equations arise:

$$\begin{bmatrix} \dot{x} & \dot{y} \\ \dot{y} & -\dot{x} \end{bmatrix} \begin{bmatrix} x_{CPA} \\ y_{CPA} \end{bmatrix} = \begin{bmatrix} 0 \\ \dot{y}x - \dot{x}y \end{bmatrix} \quad (\text{D.4})$$

Solving for this system of equations:

$$x_{CPA} = \frac{\dot{y}(\dot{y}x - \dot{x}y)}{\dot{x}^2 + \dot{y}^2} \quad (\text{D.5})$$

$$y_{CPA} = \frac{-\dot{x}(\dot{y}x - \dot{x}y)}{\dot{x}^2 + \dot{y}^2} \quad (\text{D.6})$$

The expression for r_{CPA} is:

$$r_{CPA} = \sqrt{x_{CPA}^2 + y_{CPA}^2} = \frac{\dot{y}x - \dot{x}y}{\sqrt{\dot{x}^2 + \dot{y}^2}} \quad (\text{D.7})$$

APPENDIX E
2D ANALYSIS SENSOR ADJUSTMENTS

This appendix includes the analysis of sample rate and detection range adjustments from the nominal sensor to support section 6.2.

E.1 Sensor Sample Rate Uncertainty Adjustment

Lowering the sensor sample rate to $\Delta t = 0.35$ Hz, represents a relaxation that can still meet integrity and continuity requirements. The results in Figure E.1 depict this Δt -adjusted sensor meeting both σ_τ and σ_r requirements. The adjustment has

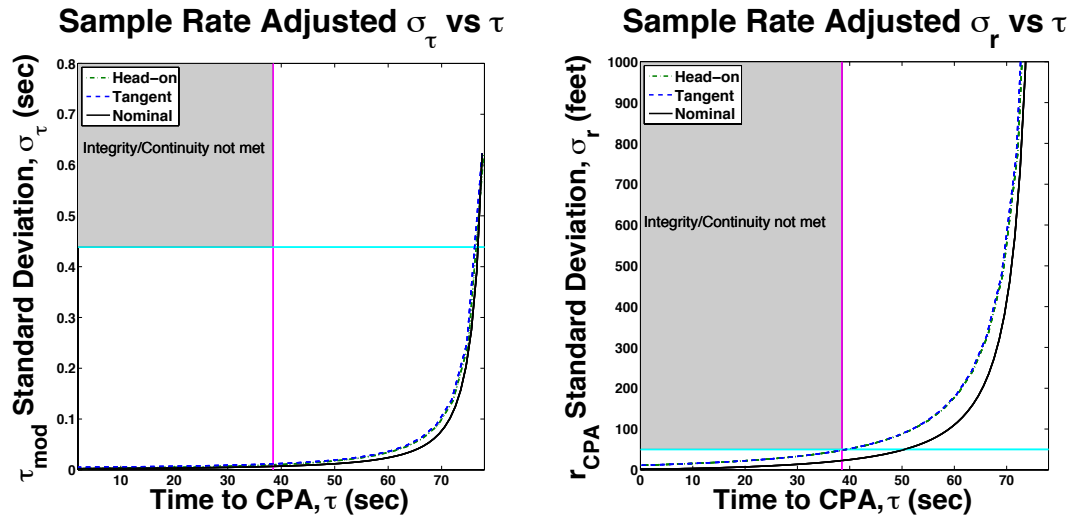


Figure E.1. Results of a Δt -Adjusted Sensor: $\Delta t = 0.35$ Hz

minimal impact on the σ_τ curve, but it brings the σ_r curve very close to the integrity and continuity limit. This sensitivity arises from having less measurements to inform the estimator. Both trajectories have similar performance, as cataloged in Table E.1. Here, for both curves, the most restrictive trajectory is the tangent trajectory.

Table E.1. Results of a Δt -Adjusted Sensor

Trajectory	τ at $\tilde{\sigma}_\tau$	τ at $\tilde{\sigma}_r$
Nominal	76.8 s	50.5 s
Head-on	76.4 s	39.4 s
Tangent	76.2 s	39.3 s

E.2 Sensor Detection Range Adjustment

The next adjustment is to reduce sensor detection range to 6.5 NM, representing the tightest detection range that can still meet integrity and continuity requirements. The sensor sample rate is returned to the nominal 1 Hz. The results in Figure E.2 depict this detection range adjusted sensor meeting both σ_τ and σ_r requirements. Both curves are sensitive to detection range since the tighter detection

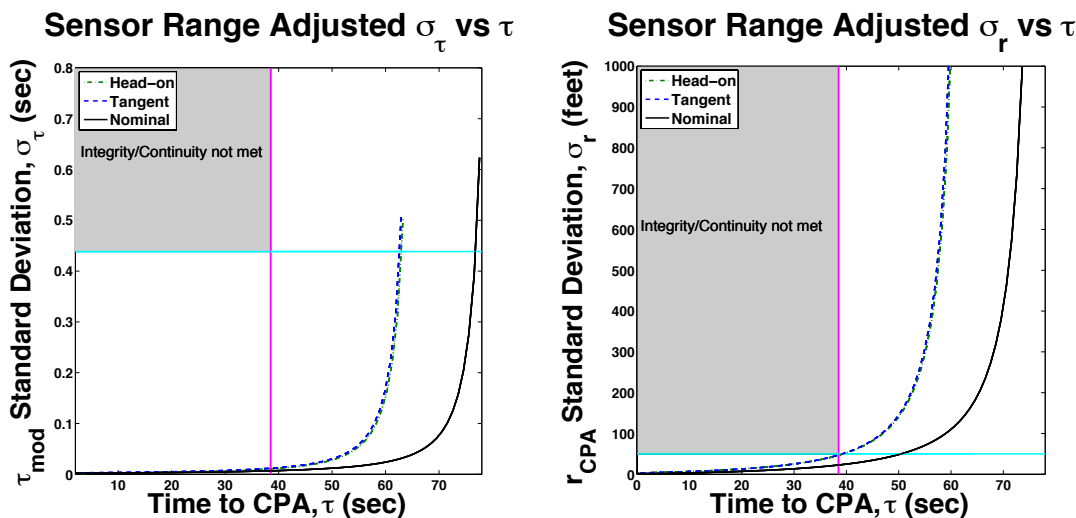


Figure E.2. Results of a ρ_0 -Adjusted Sensor: $\rho_0 = 6.5$ NM

range results in less time to the CPA (and thus a smaller initial tau) as well as less measurements. Both trajectories have similar performance, as cataloged in Table E.2. Here, for both curves, the most restrictive trajectory is the tangent trajectory.

Table E.2. Results of a ρ_0 -Adjusted Sensor

Trajectory	τ at $\tilde{\sigma}_\tau$	τ at $\tilde{\sigma}_r$
Nominal	76.8 s	50.5 s
Head-on	62.9 s	39.4 s
Tangent	62.6 s	39.2 s

APPENDIX F
CARTESIAN TO SPHERICAL PARTIAL DERIVATIVES

The following is the nonlinear transformation of the cartesian position and velocity states to the spherical position and range rate measurements:

$$\begin{bmatrix} \rho \\ \theta \\ \phi \\ \dot{\rho} \end{bmatrix} = \mathbf{h}(\mathbf{x}) = \begin{bmatrix} \sqrt{x^2 + y^2 + z^2} \\ \tan^{-1} \frac{y}{x} \\ \sin^{-1} \frac{z}{\sqrt{x^2 + y^2 + z^2}} \\ \frac{x\dot{x} + y\dot{y} + z\dot{z}}{\sqrt{x^2 + y^2 + z^2}} \end{bmatrix} \quad (\text{F.1})$$

$$\text{for } \mathbf{x} = \begin{bmatrix} x & y & z & \dot{x} & \dot{y} & \dot{z} \end{bmatrix}^T.$$

The following are the partials of the spherical position and range rate with respect to \mathbf{x} . For slant range, ρ :

$$\frac{\partial \rho}{\partial x} = \frac{x}{\rho} \quad (\text{F.2})$$

$$\frac{\partial \rho}{\partial y} = \frac{y}{\rho} \quad (\text{F.3})$$

$$\frac{\partial \rho}{\partial z} = \frac{z}{\rho} \quad (\text{F.4})$$

$$\frac{\partial \rho}{\partial \dot{x}} = \frac{\partial \rho}{\partial \dot{y}} = \frac{\partial \rho}{\partial \dot{z}} = 0 \quad (\text{F.5})$$

where $\rho = \sqrt{x^2 + y^2 + z^2}$.

For azimuth, θ :

$$\frac{\partial \theta}{\partial x} = \frac{-y}{x^2 + y^2} \quad (\text{F.6})$$

$$\frac{\partial \theta}{\partial y} = \frac{x}{x^2 + y^2} \quad (\text{F.7})$$

$$\frac{\partial \theta}{\partial z} = \frac{\partial \theta}{\partial \dot{x}} = \frac{\partial \theta}{\partial \dot{y}} = \frac{\partial \theta}{\partial \dot{z}} = 0 \quad (\text{F.8})$$

For elevation, ϕ :

$$\frac{\partial \phi}{\partial x} = \frac{-xz}{r\rho^2} \quad (\text{F.9})$$

$$\frac{\partial \phi}{\partial y} = \frac{-yz}{r\rho^2} \quad (\text{F.10})$$

$$\frac{\partial \phi}{\partial z} = \frac{r}{\rho^2} \quad (\text{F.11})$$

$$\frac{\partial \phi}{\partial \dot{x}} = \frac{\partial \rho}{\partial \dot{y}} = \frac{\partial \rho}{\partial \dot{z}} = 0 \quad (\text{F.12})$$

where $r = \sqrt{x^2 + y^2}$.

For range rate, $\dot{\rho}$:

$$\frac{\partial \dot{\rho}}{\partial x} = \frac{\dot{x}(y^2 + z^2)}{\rho^3} \quad (\text{F.13})$$

$$\frac{\partial \dot{\rho}}{\partial y} = \frac{\dot{y}(x^2 + z^2)}{\rho^3} \quad (\text{F.14})$$

$$\frac{\partial \dot{\rho}}{\partial z} = \frac{\dot{z}(x^2 + y^2)}{\rho^3} \quad (\text{F.15})$$

$$\frac{\partial \dot{\rho}}{\partial \dot{x}} = \frac{x}{\rho} \quad (\text{F.16})$$

$$\frac{\partial \dot{\rho}}{\partial \dot{y}} = \frac{y}{\rho} \quad (\text{F.17})$$

$$\frac{\partial \dot{\rho}}{\partial \dot{z}} = \frac{z}{\rho} \quad (\text{F.18})$$

The resulting matrix of \mathbf{h} partials is as follows:

$$\frac{\partial \mathbf{h}}{\partial \mathbf{x}} = \begin{bmatrix} \frac{x}{\rho} & \frac{y}{\rho} & \frac{z}{\rho} & 0 & 0 & 0 \\ \frac{-y}{x^2+y^2} & \frac{x}{x^2+y^2} & 0 & 0 & 0 & 0 \\ \frac{-xz}{r\rho^2} & \frac{-yz}{r\rho^2} & \frac{r}{\rho^2} & 0 & 0 & 0 \\ \frac{\dot{x}(y^2+z^2)}{\rho^3} & \frac{\dot{y}(x^2+z^2)}{\rho^3} & \frac{\dot{z}(x^2+y^2)}{\rho^3} & \frac{x}{\rho} & \frac{y}{\rho} & \frac{z}{\rho} \end{bmatrix} \quad (\text{F.19})$$

APPENDIX G
HAZARD STATE PARTIAL DERIVATIVES

A first order Taylor series expansion is used to obtain the linearized approximation of the hazard state estimates in relation to the trajectory state estimates in equation (2.17). This requires the partial derivatives of the hazard states in relation to the trajectory states.

G.1 Modified Tau

The modified tau equation does not use z or \dot{z} :

$$\tau_{mod} = \frac{D_{mod}^2 - x^2 - y^2}{x\dot{x} + y\dot{y}} \quad (\text{G.1})$$

Using the quotient rule, the resulting partial derivatives of τ_{mod} with respect to the horizontal position states x and y are:

$$\frac{\partial \tau_{mod}}{\partial x} = \frac{-2x - \dot{x}\tau_{mod}}{x\dot{x} + y\dot{y}} \quad (\text{G.2})$$

$$\frac{\partial \tau_{mod}}{\partial y} = \frac{-2y - \dot{y}\tau_{mod}}{x\dot{x} + y\dot{y}} \quad (\text{G.3})$$

The quotient rule is used again to find the resulting partial derivatives of τ_{mod} with respect to the horizontal velocity states \dot{x} and \dot{y} :

$$\frac{\partial \tau_{mod}}{\partial \dot{x}} = \frac{-x\tau_{mod}}{x\dot{x} + y\dot{y}} \quad (\text{G.4})$$

$$\frac{\partial \tau_{mod}}{\partial \dot{y}} = \frac{-y\tau_{mod}}{x\dot{x} + y\dot{y}} \quad (\text{G.5})$$

All four partials of τ_{mod} together are as follows:

$$\begin{aligned}
\frac{\partial \tau_{mod}}{\partial x} &= \frac{-2x - \dot{x}\tau_{mod}}{x\dot{x} + y\dot{y}} \\
\frac{\partial \tau_{mod}}{\partial y} &= \frac{-2y - \dot{y}\tau_{mod}}{x\dot{x} + y\dot{y}} \\
\frac{\partial \tau_{mod}}{\partial \dot{x}} &= \frac{-x\tau_{mod}}{x\dot{x} + y\dot{y}} \\
\frac{\partial \tau_{mod}}{\partial \dot{y}} &= \frac{-y\tau_{mod}}{x\dot{x} + y\dot{y}}
\end{aligned} \tag{G.6}$$

G.2 True Tau

True tau is not a function of z or \dot{z} . The true tau equation is:

$$\tau_{true} = \frac{-(\dot{x}x + \dot{y}y)}{\dot{x}^2 + \dot{y}^2} \tag{G.7}$$

The resulting partial derivatives of τ_{true} with respect to the states x and y are easy to calculate:

$$\begin{aligned}
\frac{\partial \tau_{true}}{\partial x} &= -\frac{\dot{x}}{\dot{x}^2 + \dot{y}^2} \\
\frac{\partial \tau_{true}}{\partial y} &= -\frac{\dot{y}}{\dot{x}^2 + \dot{y}^2}
\end{aligned} \tag{G.8}$$

The partials with respect to the rates, \dot{x} and \dot{y} , are a bit more complicated. For $\frac{\partial \tau_{true}}{\partial \dot{x}}$, this can be written as:

$$\frac{\partial \tau_{true}}{\partial \dot{x}} = \frac{\partial(\frac{\alpha}{\beta})}{\partial \dot{x}} \tag{G.9}$$

where $\alpha = -(\dot{x}x + \dot{y}y)$ and $\beta = \dot{x}^2 + \dot{y}^2$. Using the quotient rule, the partial becomes:

$$\frac{\partial \tau_{true}}{\partial \dot{x}} = \frac{\beta \frac{\partial \alpha}{\partial \dot{x}} - \alpha \frac{\partial \beta}{\partial \dot{x}}}{\beta^2} = \frac{(\dot{x}^2 + \dot{y}^2)(-x) + (\dot{x}x + \dot{y}y)2\dot{x}}{(\dot{x}^2 + \dot{y}^2)^2} \tag{G.10}$$

Reducing terms:

$$\frac{\partial \tau_{true}}{\partial \dot{x}} = -\frac{x}{\dot{x}^2 + \dot{y}^2} + \frac{2\dot{x}(\dot{x}x + \dot{y}y)}{(\dot{x}^2 + \dot{y}^2)^2} \tag{G.11}$$

Since true tau is:

$$\tau = \frac{-(\dot{x}x + \dot{y}y)}{\dot{x}^2 + \dot{y}^2} \quad (\text{G.12})$$

The partial becomes:

$$\frac{\partial \tau_{true}}{\partial \dot{x}} = \frac{-(x + 2\dot{x}\tau)}{\dot{x}^2 + \dot{y}^2} \quad (\text{G.13})$$

Applying the same procedure to the partial with respect to \dot{y} :

$$\frac{\partial \tau_{true}}{\partial \dot{y}} = \frac{-(y + 2\dot{y}\tau)}{\dot{x}^2 + \dot{y}^2} \quad (\text{G.14})$$

All four partials of τ_{true} together are as follows:

$$\begin{aligned} \frac{\partial \tau_{true}}{\partial x} &= -\frac{\dot{x}}{\dot{x}^2 + \dot{y}^2} \\ \frac{\partial \tau_{true}}{\partial y} &= -\frac{\dot{y}}{\dot{x}^2 + \dot{y}^2} \\ \frac{\partial \tau_{true}}{\partial \dot{x}} &= \frac{-(x + 2\dot{x}\tau)}{\dot{x}^2 + \dot{y}^2} \\ \frac{\partial \tau_{true}}{\partial \dot{y}} &= \frac{-(y + 2\dot{y}\tau)}{\dot{x}^2 + \dot{y}^2} \end{aligned} \quad (\text{G.15})$$

G.3 Horizontal CPA

In the horizontal plane, the relative altitude, z , and altitude rate, \dot{z} , are both zero. The horizontal CPA, r_{CPA} , equation is:

$$r_{CPA} = \sqrt{x_{CPA}^2 + y_{CPA}^2} = \sqrt{x^2 + y^2 + 2\tau(\dot{x}x + \dot{y}y) + \tau^2(\dot{x}^2 + \dot{y}^2)} \quad (\text{G.16})$$

where x_{CPA} , y_{CPA} and true tau, τ , are:

$$x_{CPA} = x + \tau\dot{x} \quad (\text{G.17})$$

$$y_{CPA} = y + \tau\dot{y} \quad (\text{G.18})$$

$$\tau = \frac{-(\dot{x}x + \dot{y}y)}{\dot{x}^2 + \dot{y}^2} \quad (\text{G.19})$$

Starting with the partial about x , $\frac{\partial r_{CPA}}{\partial x}$ can be solved using the chain rule:

$$\frac{\partial r_{CPA}}{\partial x} = \frac{\partial r_{CPA}}{\partial \alpha} \frac{\partial \alpha}{\partial x} \quad (\text{G.20})$$

where $\alpha = x^2 + y^2 + 2\tau(\dot{x}x + \dot{y}y) + \tau^2(\dot{x}^2 + \dot{y}^2)$. Since $r_{CPA} = \sqrt{\alpha}$, the partial of r_{CPA} with respect to α is:

$$\frac{\partial r_{CPA}}{\partial \alpha} = \frac{1}{2r_{CPA}} = \frac{1}{2\sqrt{\alpha}} \quad (\text{G.21})$$

The partial of α with respect to x is:

$$\frac{\partial \alpha}{\partial x} = 2x + 2\frac{\partial[\tau(\dot{x}x + \dot{y}y)]}{\partial x} + (\dot{x}^2 + \dot{y}^2)\frac{\partial \tau^2}{\partial x} \quad (\text{G.22})$$

where

$$\frac{\partial[\tau(\dot{x}x + \dot{y}y)]}{\partial x} = \tau \frac{\partial(\dot{x}x + \dot{y}y)}{\partial x} + (\dot{x}x + \dot{y}y) \frac{\partial \tau}{\partial x} = \dot{x}\tau + \frac{-\dot{x}(\dot{x}x + \dot{y}y)}{\dot{x}^2 + \dot{y}^2} = 2\dot{x}\tau \quad (\text{G.23})$$

$$\frac{\partial \tau^2}{\partial x} = \frac{2\dot{x}(\dot{x}x + \dot{y}y)(\dot{x}^2 + \dot{y}^2)^2}{(\dot{x}^2 + \dot{y}^2)^4} = \frac{-2\dot{x}\tau}{\dot{x}^2 + \dot{y}^2} \quad (\text{G.24})$$

Substituting into equation (G.22):

$$\frac{\partial \alpha}{\partial x} = 2x + 2(2\dot{x}\tau) + (\dot{x}^2 + \dot{y}^2) \frac{-2\dot{x}\tau}{\dot{x}^2 + \dot{y}^2} = 2x + 4\dot{x}\tau - 2\dot{x}\tau = 2x + 2\dot{x}\tau = 2x_{CPA} \quad (\text{G.25})$$

Substituting into equation (G.20):

$$\frac{\partial r_{CPA}}{\partial x} = \frac{x_{CPA}}{r_{CPA}} \quad (\text{G.26})$$

Following the same procedure for $\frac{\partial r_{CPA}}{\partial y}$:

$$\frac{\partial r_{CPA}}{\partial y} = \frac{y_{CPA}}{r_{CPA}} \quad (\text{G.27})$$

The partial about \dot{x} , $\frac{\partial r_{CPA}}{\partial \dot{x}}$ can be solved using the chain rule:

$$\frac{\partial r_{CPA}}{\partial \dot{x}} = \frac{\partial r_{CPA}}{\partial \alpha} \frac{\partial \alpha}{\partial \dot{x}} = \frac{1}{2r_{CPA}} \frac{\partial \alpha}{\partial \dot{x}} \quad (\text{G.28})$$

The partial of α with respect to \dot{x} is:

$$\frac{\partial \alpha}{\partial \dot{x}} = 2 \frac{\partial [\tau(\dot{x}x + \dot{y}y)]}{\partial \dot{x}} + \frac{\partial [\tau^2(\dot{x}^2 + \dot{y}^2)]}{\partial \dot{x}} \quad (\text{G.29})$$

where partial of the first term is broken down using the product rule:

$$\frac{\partial [\tau(\dot{x}x + \dot{y}y)]}{\partial \dot{x}} = \tau \frac{\partial (\dot{x}x + \dot{y}y)}{\partial \dot{x}} + (\dot{x}x + \dot{y}y) \frac{\partial \tau}{\partial \dot{x}} = x\tau + (\dot{x}x + \dot{y}y) \frac{\partial \tau}{\partial \dot{x}} \quad (\text{G.30})$$

and the partial of τ with respect to \dot{x} is broken down using the quotient rule:

$$\frac{\partial \tau}{\partial \dot{x}} = \frac{-x(\dot{x}^2 + \dot{y}^2) - (-\dot{x}x - \dot{y}y)2\dot{x}}{(\dot{x}^2 + \dot{y}^2)^2} = \frac{-x - 2\dot{x}\tau}{\dot{x}^2 + \dot{y}^2} \quad (\text{G.31})$$

Substituting back into equation (G.30):

$$\frac{\partial [\tau(\dot{x}x + \dot{y}y)]}{\partial \dot{x}} = x\tau + (\dot{x}x + \dot{y}y) \frac{-x - 2\dot{x}\tau}{\dot{x}^2 + \dot{y}^2} = 2x\tau + 2\dot{x}\tau^2 \quad (\text{G.32})$$

The partial of the second term of equation (G.29) is broken down using the product rule:

$$\frac{\partial [\tau^2(\dot{x}^2 + \dot{y}^2)]}{\partial \dot{x}} = \tau^2 \frac{\partial (\dot{x}^2 + \dot{y}^2)}{\partial \dot{x}} + (\dot{x}^2 + \dot{y}^2) \frac{\partial \tau^2}{\partial \dot{x}} = 2\dot{x}\tau^2 + (\dot{x}^2 + \dot{y}^2) \frac{\partial \tau^2}{\partial \dot{x}} \quad (\text{G.33})$$

and the partial of τ^2 with respect to \dot{x} is broken down using the quotient rule:

$$\frac{\partial \tau^2}{\partial \dot{x}} = \frac{2x(\dot{x}x + \dot{y}y)(\dot{x}^2 + \dot{y}^2)^2 - 4\dot{x}(\dot{x}^2 + \dot{y}^2)(\dot{x}x + \dot{y}y)^2}{(\dot{x}^2 + \dot{y}^2)^4} = \frac{-2x\tau - 4\dot{x}\tau^2}{\dot{x}^2 + \dot{y}^2} \quad (\text{G.34})$$

Substituting back into equation (G.33):

$$\frac{\partial[\tau^2(\dot{x}^2 + \dot{y}^2)]}{\partial \dot{x}} = 2\dot{x}\tau^2 - 2x\tau - 4\dot{x}\tau^2 = -2x\tau - 2\dot{x}\tau^2 \quad (\text{G.35})$$

Substituting into equation (G.28):

$$\frac{\partial r_{CPA}}{\partial \dot{x}} = \frac{1}{2r_{CPA}} [(2[2x\tau + 2\dot{x}\tau^2]) + (-2x\tau - 2\dot{x}\tau^2)] = \frac{x\tau + \dot{x}\tau^2}{r_{CPA}} \quad (\text{G.36})$$

This reduces to:

$$\frac{\partial r_{CPA}}{\partial \dot{x}} = \frac{\tau x_{CPA}}{r_{CPA}} = \frac{\tau(x + \dot{x}\tau)}{r_{CPA}} \quad (\text{G.37})$$

Following the same procedure for $\frac{\partial r_{CPA}}{\partial \dot{y}}$:

$$\frac{\partial r_{CPA}}{\partial \dot{y}} = \frac{\tau y_{CPA}}{r_{CPA}} = \frac{\tau(y + \dot{y}\tau)}{r_{CPA}} \quad (\text{G.38})$$

All four partials of r_{CPA} together are as follows:

$$\begin{aligned} \frac{\partial r_{CPA}}{\partial x} &= \frac{x_{CPA}}{r_{CPA}} \\ \frac{\partial r_{CPA}}{\partial y} &= \frac{y_{CPA}}{r_{CPA}} \\ \frac{\partial r_{CPA}}{\partial \dot{x}} &= \frac{\tau x_{CPA}}{r_{CPA}} \\ \frac{\partial r_{CPA}}{\partial \dot{y}} &= \frac{\tau y_{CPA}}{r_{CPA}} \end{aligned} \quad (\text{G.39})$$

G.4 Predicted Vertical Separation

To account for the warning alert criteria in the DAA MOPS, there needs to be a predicted vertical separation that can lookahead up to 25 seconds. This is accounted for in the following equation:

$$z_p = z + p\Delta t\dot{z} \quad (\text{G.40})$$

where p are the all the future epochs up to the 25 second lookahead time.

The partial derivative with respect to z is:

$$\frac{\partial z_p}{\partial z} = 1 \quad (\text{G.41})$$

The partial derivative with respect to \dot{z} is:

$$\frac{\partial z_p}{\partial \dot{z}} = p\Delta t \quad (\text{G.42})$$

BIBLIOGRAPHY

- [1] 14 CFR 91.113. Right-of-way Rules: Except Water Operations, Jul 2004.
- [2] 14 CFR 91.159. VFR Cruising Altitude or Flight Level, Dec 2003.
- [3] Miloud-Aouidate Amal and Baba-Ali Ahmed. Survey of Nearest Neighbor Condensing Techniques. *International Journal of Advanced Computer Science and Applications*, 2(11), 2011.
- [4] Ernest E. Anderson, William Watson, Kathleen Johnson, Nathan R. Kimber, and Nicholas J. Weiss. A Legal Analysis of 14 C.F.R. Part 91 See and Avoid Rules to Identify Provisions Focused on Pilot Responsibilities to See and Avoid in the National Airspace System. Technical report, University of North Dakota-U.S. Department of Transportation, Federal Aviation Administration, Dec 2013.
- [5] Alexandr Andoni. *Nearest Neighbor Search: the Old, the New, and the Impossible*. PhD thesis, Massachusetts Institute of Technology, Sep 2009.
- [6] Javier Areta, Yaakov Bar-Shalom, and Ron Rothrock. Misassociation Probability in M2TA and T2TA. *Journal of Advances in Information Fusion*, 2(2):113–127, Dec 2007.
- [7] Yaakov Bar-Shalom, Fred Daum, and Jim Huang. The Probabilistic Data Association Filter. *IEEE Control Syst. Mag.*, 29(6):82–100, Dec 2009.
- [8] Yaakov Bar-Shalom and Thomas E. Fortmann. *Tracking and Data Association*, volume 179 of Mathematics in Science and Engineering Series. Academic Press, San Diego, CA, 1988.
- [9] Javier Barreiro, Minh Do, and David E. Smith. Intelligent UAS Sense-and-Avoid Utilizing Global Constraints. In *ICAPS-2014 Scheduling and Planning Applications Workshop (SPARK)*, Portsmouth, NH, Jun 2014. ICAPS.
- [10] Thomas B. Billingsley, Mykel J. Kochenderfer, and James P. Chryssanthacopoulos. Collision Avoidance for General Aviation. *IEEE Aerospace and Electronic Systems Magazine*, 27(7):4–12, Jul 2012.
- [11] Fang-Cheng Chan, Mathieu Joerger, Samer Khanafseh, and Boris Pervan. Bayesian Fault-Tolerant Position Estimator and Integrity Risk Bound for GNSS Navigation. *Journal of Navigation*, 67(05):753–775, Apr 2014.
- [12] Robert H. Chen, Arthur Gevorkian, Alex Fung, Won-Zon Chen, and Vincent Raska. Multi-Sensor Data Integration for Autonomous Sense and Avoid. In *AIAA Infotech@Aerospace*, St Louis, MO, Mar 2011.
- [13] James P. Chryssanthacopoulos and Mykel J. Kochenderfer. Accounting for State Uncertainty in Collision Avoidance. *AIAA Journal of Guidance, Control, and Dynamics*, 34(4):951–960, Jul 2011.
- [14] Stephen P. Cook, Dallas Brooks, Rodney Cole, Davis Hackenberg, and Vincent Raska. Defining Well Clear for Unmanned Aircraft Systems. In *AIAA Infotech @ Aerospace*, pages 1–20, Kissimmee, FL, Jan 2015. American Institute of Aeronautics and Astronautics (AIAA).

- [15] K. Dalamagkidis, K.P. Valavanis, and L.A. Piegl. On Unmanned Aircraft Systems Issues, Challenges and Operational Restrictions Preventing Integration into the National Airspace System. *Progress in Aerospace Sciences*, 44(7):503–519, Jul 2008.
- [16] Bruce DeCleene. Defining Pseudorange Integrity - Overbounding. In *Institute of Navigation GPS Conference*, pages 1916–1924, Salt Lake City, UT, Sep 2000.
- [17] Department of Defense. Unmanned Aircraft System Airspace Integration Plan, Mar 2011. Version 2.0.
- [18] Department of Defense. Unmanned Systems Integrated Roadmap FY2013-2038, 2013. Reference Number: 14-S-0553.
- [19] Christian Desrosiers and George Karypis. A Comprehensive Survey of Neighborhood-based Recommendation Methods. In *Recommender Systems Handbook*, pages 107–144. Springer Science + Business Media, Oct 2010.
- [20] DJI. *Spreading Wings S1000 - Specs*, Apr 2016 (accessed April 11, 2016). <http://www.dji.com/product/spreading-wings-s1000/spec>.
- [21] Zvi Drezner. Computation of the Trivariate Normal Integral. *Mathematics of Computation*, 62(205):289–294, Jan 1994.
- [22] A.C. Drumm, J.W. Andrews, T.D. Hall, V.M. Heinz, J.K. Kuchar, S.D. Thompson, and J.D. Welch. Remotely Piloted Vehicles in Civil Airspace: Requirements and Analysis Methods for the Traffic Alert and Collision Avoidance System (TCAS) and See-And-Avoid Systems. In *IEEE Digital Avionics Systems Conference*, volume 2, pages 12.D.1–1–14, Salt Lake City, UT, Oct 2004.
- [23] Matthew Edwards. A Safety Driven Approach to the Development of an Airborne Sense and Avoid System. In *Infotech@Aerospace 2012*, pages 1–12, Garden Grove, CA, Jun 2012. American Institute of Aeronautics and Astronautics (AIAA).
- [24] Matthew W. M. Edwards and Michael P. Owen. Validating a Concept for Airborne Sense and Avoid. In *American Control Conference*, pages 1192–1197, Portland, OR, Jun 2014.
- [25] Per Enge. Local Area Augmentation of GPS for the Precision Approach of Aircraft. *Proceedings of the IEEE*, 87(1):111–132, Jan 1999.
- [26] L.P. Espindle, J.D. Griffith, and J.K. Kuchar. Safety Analysis of Upgrading to TCAS Version 7.1 Using the 2008 U.S. Correlated Encounter Model. Technical report, Lincoln Laboratory, Massachusetts Institute of Technology, May 2009.
- [27] Eurocontrol. European Action Plan for the Prevention of Level Bust, Jul 2004.
- [28] Federal Aviation Administration. Advisory Circular 25.1309-1A - System Design and Analysis, Jun 1988.
- [29] Federal Aviation Administration. Introduction to TCAS II Version 7.1, Feb 2011. Reference Number: HQ-111358.
- [30] Federal Aviation Administration. Integration of Civil Unmanned Aircraft Systems (UAS) in the National Airspace System (NAS) Roadmap, Nov 2013.

- [31] Federal Aviation Administration. Sense and Avoid (SAA) for Unmanned Aircraft Systems (UAS), SAA Workshop Second Caucus Report, Jan 2013.
- [32] Federal Aviation Administration. JO 7110.65W: Air Traffic Control, Dec 2015.
- [33] Federal Aviation Administration. FAA Aerospace Forecast, Mar 2016. Reference Number: TC16-0002.
- [34] Federal Aviation Administration TCAS Program Office. Concept of Use for the Airborne Collision Avoidance System X_U, Sep 2015. Version 2, Revision 0.
- [35] Arthur Gelb, editor. *Applied Optimal Estimation*. The MIT Press, sixteenth edition, 2001.
- [36] Scott Graham, Jan De Luca, Won zon Chen, Jacob Kay, Michael Deschenes, Norman Weingarten, Vince Raska, and Xiaogong Lee. Multiple Intruder Autonomous Avoidance Flight Test. In *Infotech@Aerospace 2011*, St Louis, MO, Mar 2011. American Institute of Aeronautics and Astronautics (AIAA).
- [37] Curtis W. Heisey, Adam G. Hendrickson, Barbara J. Chludzinski, Rodney E. Cole, Mark Ford, Larry Herbek, Magnus Ljungberg, Zakir Magdum, D. Marquis, Alexander Mezhirov, John L. Pennell, Ted A. Roe, and Andrew J. Weinert. A Reference Software Architecture to Support Unmanned Aircraft Integration in the National Airspace System. *Journal of Intelligent & Robotic Systems*, 69(1-4):41–55, Jan 2013.
- [38] International Civil Aviation Organization. ICAO 9689-AN/953 Manual on Airspace Planning Methodology for the Determination of Separation Minima, Dec 1998.
- [39] International Civil Aviation Organization. *International Standards and Recommended Practices, Annex 10*, volume I: Radio Navigation Aids. New Zealand, sixth edition, July 2006.
- [40] Michael B. Jamoom, Mathieu Joerger, and Boris Pervan. Sense and Avoid for Unmanned Aircraft Systems: Ensuring Integrity and Continuity for Three Dimensional Intruder Trajectories. In *Institute of Navigation GNSS+*, Tampa, FL, Sep 2015.
- [41] Michael B. Jamoom, Mathieu Joerger, and Boris Pervan. Unmanned Aircraft System Sense and Avoid Integrity and Continuity Risk for Non-Cooperative Intruders. In *AIAA Infotech@Aerospace*, Kissimmee, FL, Jan 2015.
- [42] Michael B. Jamoom, Mathieu Joerger, and Boris Pervan. UAS Sense and Avoid Integrity and Continuity for Multiple Intruders. In *IEEE/ION PLANS*, Savannah, GA, Apr 2016.
- [43] Michael B. Jamoom, Mathieu Joerger, and Boris Pervan. Unmanned Aircraft System Sense-and-Avoid Integrity and Continuity Risk. *Journal of Guidance, Control, and Dynamics*, 39(3):498–509, Mar 2016.
- [44] Michael B. Jamoom, Mathieu Joerger, and Boris Pervan. Unmanned Aircraft System Sense and Avoid Integrity and Continuity: Uncertainty in Aircraft Dynamics. In *AIAA Infotech@Aerospace*, San Diego, CA, Jan 2016.

- [45] Mathieu Joerger, Michael Jamoom, Matthew Spenko, and Boris Pervan. Integrity and Continuity of Feature Extraction and Data Association. In *IEEE/ION PLANS*, Savannah, GA, Apr 2016.
- [46] R. J. Kelly and J. M. Davis. Required Navigation Performance (RNP) for Precision Approach and Landing with GNSS Application. *Navigation, Journal of the Institute of Navigation*, 41(1):1–30, Spring 1994.
- [47] Jong-Hun Kim, Dae Woo Lee, Kyeum-Rae Cho, Seon-Yeong Jo, Jung-Ho Kim, Chan-Oh Min, Dong-In Han, and Sung-Jin Cho. Development of an Electro-optical System for Small UAV. *Aerospace Science and Technology*, 14(7):505–511, Oct 2010.
- [48] Mykel J. Kochenderfer, Matthew W. M. Edwards, Leo P. Espindle, James K. Kuchar, and J. Daniel Griffith. Airspace Encounter Models for Estimating Collision Risk. *AIAA Journal of Guidance, Control, and Dynamics*, 33(2):487–499, Mar 2010.
- [49] Mykel J. Kochenderfer, Leo P. Espindle, James K. Kuchar, and J. D. Griffith. Correlated Encounter Model for Cooperative Aircraft in the National Airspace System. Project Report ATC-344, Massachusetts Institute of Technology, Lincoln Laboratory, 2008.
- [50] Mykel J. Kochenderfer, James K. Kuchar, Leo P. Espindle, and J. D. Griffith. Uncorrelated Encounter Model of the National Airspace System. Project Report ATC-345, Massachusetts Institute of Technology, Lincoln Laboratory, 2008.
- [51] James K. Kuchar and Lee C. Yang. A Review of Conflict Detection and Resolution Modeling Methods. *IEEE Transactions on Intelligent Transportation Systems*, 1(4):179–189, Dec 2000.
- [52] Hak-Tae Lee, Larry A. Meyn, and SoYoung Kim. Probabilistic Safety Assessment of Unmanned Aerial System Operations. *AIAA Journal of Guidance, Control, and Dynamics*, 36(2):610–616, Mar 2013.
- [53] Seung Man Lee, Chunki Park, Marcus A. Johnson, and Eric R. Mueller. Investigating Effects of Well Clear Definitions on UAS Sense-And-Avoid Operations. In *2013 Aviation Technology, Integration, and Operations Conference*, pages 1–15, Los Angeles, CA, Aug 2013. American Institute of Aeronautics and Astronautics (AIAA).
- [54] Young C. Lee. Analysis of Range and Position Comparison Methods as a Means to Provide GPS Integrity in the User Receiver. In *Proceedings of the 42nd Annual Meeting of The Institute of Navigation*, pages 1–4, Seattle, WA, Jun 1986.
- [55] P. C. Mahalanobis. On the Generalized Distance in Statistics. *Proceedings of the National Institute of Sciences (Calcutta)*, 2(1):49–55, Apr 1936.
- [56] Michael P. McLaughlin and Andrew D. Zeitlin. Safety Study of TCAS II for Logic Version 6.04. Technical report, MITRE Corporation-U.S. Department of Transportation, Federal Aviation Administration, Jul 1992.
- [57] Cesar Munoz, Anthony Narkawicz, James Chamberlain, Maria C. Consiglio, and Jason M. Upchurch. A Family of Well-Clear Boundary Models for the Integration of UAS in the NAS. In *14th AIAA Aviation Technology, Integration, and Operations Conference*, Atlanta, GA, Jun 2014. American Institute of Aeronautics and Astronautics (AIAA).

- [58] Cesar Munoz, Anthony Narkawicz, George Hagen, Jason Upchurch, Aaron Dutle, Maria Consiglio, and James Chamberlain. DAIDALUS: Detect and Avoid Alerting Logic for Unmanned Systems. In *2015 IEEE/AIAA 34th Digital Avionics Systems Conference (DASC)*, Prague, Czech Republic, Sep 2015. Institute of Electrical & Electronics Engineers (IEEE).
- [59] Songhwai Oh, S. Russell, and S. Sastry. Markov Chain Monte Carlo Data Association for General Multiple-Target Tracking Problems. In *2004 43rd IEEE Conference on Decision and Control (CDC) (IEEE Cat. No.04CH37601)*, Nassau, Bahamas, Dec 2004. Institute of Electrical & Electronics Engineers (IEEE).
- [60] Michael P. Owen, Sean M. Duffy, and Matthew W. M. Edwards. Unmanned Aircraft Sense and Avoid Radar: Surrogate Flight Testing Performance Evaluation. In *IEEE Radar Conference*, pages 548–551, Cincinnati, OH, May 2014.
- [61] Lucy Y. Pao and Richard M. Powers. A Comparison of Several Different Approaches for Target Tracking with Clutter. In *Proceedings of the 2003 American Control Conference*, Denver, CO, Jun 2003. Institute of Electrical & Electronics Engineers (IEEE).
- [62] Bradford W. Parkinson and Penina Axelrad. Autonomous GPS Integrity Monitoring Using the Pseudorange Residual. *Navigation, Journal of The Institute of Navigation*, 35(2):255–274, Summer 1988.
- [63] Boris S. Pervan, Samuel P. Pullen, and Jock R. Christie. A Multiple Hypothesis Approach to Satellite Navigation Integrity. *Navigation, Journal of The Institute of Navigation*, 45(1):62–71, Spring 1998.
- [64] Xavier Prats, Luis Delgado, Jorge Ramirez, Pablo Royo, and Enric Pastor. Requirements, Issues, and Challenges for Sense and Avoid in Unmanned Aircraft Systems. *AIAA Journal of Aircraft*, 49(3):677–687, May 2012.
- [65] Sam Pullen. What are the Differences Between Accuracy, Integrity, Continuity, and Availability, and How are they Computed? *InsideGNSS*, pages 20–24, Sep-Oct 2008.
- [66] D. Reid. An Algorithm for Tracking Multiple Targets. *IEEE Transactions on Automatic Control*, 24(6):843–854, Dec 1979.
- [67] Mohammad Reza-Abbasifard, Bijan Ghahremani, and Hassan Naderi. A Survey on Nearest Neighbor Search Methods. *International Journal of Computer Applications*, 95(25):39–52, Jun 2014.
- [68] Jason Rife, Sam Pullen, Per Enge, and Boris Pervan. Paired Overbounding for Nonideal LAAS and WAAS Error Distributions. *IEEE Transactions on Aerospace and Electronic Systems*, 42(4):1386–1395, Oct 2006.
- [69] RTCA. *RTCA SC-228 Minimum Operational Performance Standards for Unmanned Aircraft Systems*, Apr 2016 (accessed April 9, 2016). <http://www.rtca.org/content.asp?contentid=178>.
- [70] RTCA SC-147. Minimum Operational Performance Standards for Traffic Alert and Collision Avoidance System II, 2008.
- [71] RTCA SC-159. Minimum Aviation System Performance Standards for the Local Area Augmentation System, 2004.

- [72] RTCA SC-228. Draft Detect and Avoid Minimum Operational Performance Standards for Verification and Validation, Version 2, Nov 2015.
- [73] RTCA SC-228. Draft Minimum Operational Performance Standards for for Air-to-Air Radar for Detect and Avoid Systems, Sep 2015.
- [74] Omid Shakernia, Won-Zon Chen, Scott Graham, John Zvanya, Andy White, Norman Weingarten, and Vincent Raska. Sense And Avoid (SAA) Flight Test and Lessons Learned. In *AIAA Infotech@Aerospace 2007 Conference and Exhibit*, Rohnert Park, CA, May 2007. American Institute of Aeronautics and Astronautics (AIAA).
- [75] Omid Shakernia, Won-Zon Chen, and Vince Raska. Passive Ranging for UAV Sense and Avoid Applications. In *Infotech@Aerospace*, Arlington, VA, Sep 2005. American Institute of Aeronautics and Astronautics (AIAA).
- [76] Trent A. Skidmore, Frank van Graas, and Fan Liu. Ohio University LAAS Monitoring: Design and Performance. In *Proceedings of the 9th International Technical Meeting of the Satellite Division of The Institute of Navigation (ION GPS 1996)*, pages 1615–1621, Kansas City, MO, Sep 1996.
- [77] Nathan E. Smith. *Optimal Collision Avoidance Trajectories for Unmanned/Remotely Piloted Aircraft*. PhD thesis, Air Force Institute of Technology, Dec 2014.
- [78] Nathan E. Smith, Richard Cobb, Scott Pierce, and Vincent Raska. Optimal Collision Avoidance Trajectories for Unmanned/Remotely Piloted Aircraft. In *AIAA Guidance, Navigation, and Control (GNC) Conference*, Boston, MA, Aug 2013. American Institute of Aeronautics and Astronautics (AIAA).
- [79] Nathan E. Smith, Richard Cobb, Scott J. Pierce, and Vincent Raska. Optimal Collision Avoidance Trajectories via Direct Orthogonal Collocation for Unmanned/Remotely Piloted Aircraft Sense and Avoid Operations. In *AIAA Guidance, Navigation, and Control Conference*, National Harbor, MD, Jan 2014. American Institute of Aeronautics and Astronautics (AIAA).
- [80] Nathan E. Smith, Richard G. Cobb, Scott J. Pierce, and Vincent M. Raska. Uncertainty Corridors for Three-Dimensional Collision Avoidance. *Journal of Guidance, Control, and Dynamics*, 38(6):1156–1162, Jun 2015.
- [81] US House of Representatives. FAA Modernization and Reform Act of 2012, Feb 2012.
- [82] Velodyne. *VLP-16*, Apr 2016 (accessed April 11, 2016). <http://velodynelidar.com/vlp-16.html>.
- [83] Roland E. Weibel, Matthew W. M. Edwards, and Caroline S. Fernandes. Establishing a Risk-Based Separation Standard for Unmanned Aircraft Self Separation. In *Ninth USA/Europe Air Traffic Management Research and Development Seminar*, pages 1–7, Berlin, Germany, Jun 2011.
- [84] Xiang Yu and Youmin Zhang. Sense and Avoid Technologies with Applications to Unmanned Aircraft Systems: Review and Prospects. *Progress in Aerospace Sciences*, 74:152–166, Apr 2015.
- [85] Andrew D. Zeitlin. Sense & Avoid Capability Development Challenges. *IEEE Aerospace and Electronic Systems Magazine*, 25(10):27–32, Oct 2010.